Innovative Transceiver Approaches for Low-power Near-field and Far-field Applications

A Dissertation

Presented to

The Academic Faculty

By

Farzad Michael-David Inanlou

In Partial Fulfillment

of the Requirements for the Degree

Doctor of Philosophy in the

School of Electrical and Computer Engineering

Georgia Institute of Technology

August 2014

Copyright © 2014 by Farzad M.D. Inanlou

Innovative Transceiver Approaches for Low-power Near-field and Far-field Applications

Approved by:

Dr. John D. Cressler, Advisor
School of Electrical and Computer Engineering
Georgia Institute of Technology

Dr. Maysam Ghovanloo, Co-Advisor
School of Electrical and Computer Engineering
Georgia Institute of Technology

Dr. John Papapolymerou
School of Electrical and Computer Engineering
Georgia Institute of Technology

Dr. Shyh-Chiang Shen
School of Electrical and Computer Engineering
Georgia Institute of Technology

Dr. David R. Hertling
School of Electrical and Computer Engineering
Georgia Institute of Technology

Dr. Hamid Garmestani
School of Material Science and Engineering
Georgia Institute of Technology

Date Approved: May 14, 2014

ACKNOWLEDGEMENTS

I wish to thank my advisor, Dr. John Cressler, for caring so honestly and so deeply about his students' professional and personal success and well-being. His technical guidance and support were fundamental to the development of this work. I am grateful for the privilege of learning from him and for his mentorship and friendship. Also, I would like to thank my co-advisor, Dr. Ghovanloo, for his technical guidance.

I am thankful to my father for always having my back, as stable and strong as a mountain, my mother for believing in me and for being my hero, and my sister for her love. I am blessed with the unconditional love and support of a wonderful family.

I wish to thank my friends who grew to be my family in Atlanta; dear Margaret for her continuous support and invigorating smiles, and my friends Mehdi and Arashk for their friendship through all of our enlightening conversations while burning the midnight oil. I also wish to extend my gratitude to my friends and colleagues for putting up with all my questions; Duane, Rob, Chris, Cagri, Xueliang, Uei Ming and the rest of SiGe Device and Research team, and GT-bionics team, current and former members.

I want to thank, Dr. Papapolymerou, Dr. Shen, Dr. Hertling, and Dr.Garmestani for being on my committee. I am grateful to Georgia Tech President's Fellowship, NSF EAPSI Fellowship, NASA, IBM, NIH, NSF and all funding agencies for their support of this work.

TABLE OF CONTENTS

LIST OF TABLES

LIST OF FIGURES

SUMMARY

Wireless operation, near-field or far-field, is a core functionality of any mobile or autonomous system. These systems are battery operated or most often utilize energy scavenging as a means of power generation. Limited access to power, expected long and uninterrupted operation, and constrained physical parameters (e.g. weight and size), which limit overall power harvesting capabilities, are factors that outline the importance for innovative low-power approaches and designs in advanced low-power wireless applications. Low-power approaches become especially important for the wireless transceiver, the block in charge of wireless/remote functionality of the system, as this block is usually the most power hungry component in an integrated system-on-chip (SoC). Three such advanced applications with stringent power requirements are examined including space-based exploratory remote sensing probes and their associated radiation effects, millimeter-wave phased-array radar for high-altitude tactical and geological imaging, and implantable biomedical devices (IMDs) leading to the proposal and implementation of low-power wireless solutions for these applications in CMOS and SiGe BiCMOS platforms.

Space-based probes such as Mars exploration rovers (MER) must operate under serious power drain, while autonomously collecting and wirelessly transmitting data, using far-field telemetry schemes, consuming the limited power provided by energy scavenging (e.g., solar) and/or weight and size limited batteries. Since battery renewal of a deployed probe is not an option, for obvious reasons, and the power available from energy scavenging is limited and subject to a wide range of constraints, such a system can profoundly benefit from low-power designs. Furthermore, the use of low-power approaches will naturally address mission payload size, weight, and power (SWaP),

which are key driving constraints not only in mission cost, but in mission science capabilities. It is important to note that due to harsh nature of space based environments the robust operation of these wireless systems in extreme environments, mainly under intense radiation, must also be addressed. Similar arguments can also be made for the second area of interest, high-altitude phased-array imaging radars.

In the case of IMDs, a battery or a wireless power transfer link is usually in charge of providing the power needed to operate the electronics on-board. Since this system, along with the battery, is implanted in a patient, the need to perform surgery for the sake of battery replacement makes this replacement highly impractical. Therefore, designs that reduce the power consumption of the system, and thus, allow for a longer duration of uninterrupted operation with the same battery, are highly desirable. In addition, the lower power consumption of such systems relaxes requirements on power efficiency or maximum deliverable power for any wireless power transfer link.

Major accomplishments are listed below:

- Developed a novel design procedure for low-voltage low-power LNAs utilizing weakly saturated SiGe HBTs while identifying design tradeoffs in designing with weakly saturated SiGe HBTs. In addition, designed and characterized a 1.0 V, 10-22 GHz, 4 mW LNA utilizing weakly saturated SiGe HBTs for single-chip, low-power, remote sensing applications and achieved a 4 mW record lowest power reported wide-band LNA spanning X, K, Ku bands. [1]

- Designed a CMOS pulse generator and investigated total ionizing dose effects aimed at low-power space-based/high-altitude remote sensing applications. [2],[3]

- Designed a SiGe HBT Gaussian pulse generator and investigated total ionizing dose effects aimed at low-power space-based/high-altitude remote sensing

applications. In addition, conducted comparative study of CMOS and SiGe pulse generators. [4], [5]

- Designed and characterized two compact, low-Power, single-ended and differential SiGe W-band LNAs for phased array radar applications and achieved lowest power reported W-band LNA (8.8 mW from 2.2 V), and lowest NF reported W-band LNA (4.2 dB at 94 GHz) implemented in a technology with f_T/f_{max} of equal or less than 300<350 GHz. [6]

- Proposed and developed novel modulation technique named Pulse Harmonic Modulation (PHM) for wideband near-field data telemetry in high Q-factor links. In addition, developed time-domain theoretical analysis for data telemetry inductive links. [7],[8]

- Designed and characterized a low-power pulse harmonic modulation transceiver achieving a record high data rate of 10.2 Mbps. [9], [10]

CHAPTER I

SPACE-BASED EXPLORATORY REMOTE SENSING

1.1. Introduction

Robotic explorations of Mars have been in motion since the 1970s, as evidenced by the successful Viking, Pathfinder, and Mars Exploration Rover (MER) missions, laying the ground work needed for eventual human exploration [11]-[13]. Mission payload size, weight, and power (SWaP) are key driving constraints not only in mission cost, but in mission science capabilities. Advances in integrated circuit (IC) technology can naturally address SWaP goals, but with the caveat that robust performance in radiation-intense and wide-temperature range extreme environments must be adequately dealt with to ensure mission reliability. The classical paradigm for conducting such missions is to fly a "warm electronics box" (WEB) (e.g. as in the three examples cited above), but this has serious disadvantages in SWaP goals and forces a centralized electronics architecture, which is not always optimal for satisfying mission science goals [14].

Wireless communications, including both rover-to-rover and rover-to-orbit, are an essential function of any such robotic exploration mission, and must operate under serious power drain constraints while collecting and wirelessly transmitting data using the limited power provided by energy scavenging (e.g. solar or RF) or small batteries. UHF transceivers currently equipping the Spirit and Opportunity MERs weigh as much as 2 kg, with a size of 2000 cm^3 and consume approximately 45 W of power [15]. These MERs, in total, have a mass of 185 kg and measure about 5 m^3 that results in only one rover per launch, thereby limiting the surface exploration of the planet to only two sites [16]. Such systems can benefit from highly-efficient low-power design techniques.

A brief overview of SiGe HBT BiCMOS technology and radiation effects in space environments will follow.

1.1.1. Radiation Effects in Space Environment

Highly energetic particles that are extremely harmful for electronics systems dominate the skies above earth's protective atmosphere. To make matters worse, the space radiation environment is a highly dynamic one. Thus, the considerations for different space missions can differ based on variables, such as the duration of the orbit, current solar cycle, the orbital path, and altitude of a craft. As an example, the Van Allen radiation belts arise from the magnetosphere of the earth, which traps charged particles ejected from the sun (solar winds), forming a plasma torus around the earth, as seen in Fig. 4. These belts are composed of trapped electrons, protons, and low-energy heavy-ions that gyrate and traverse along magnetic field lines. Trapped electrons and protons, which can have very large energies, are the primary concern for orbital electronics.

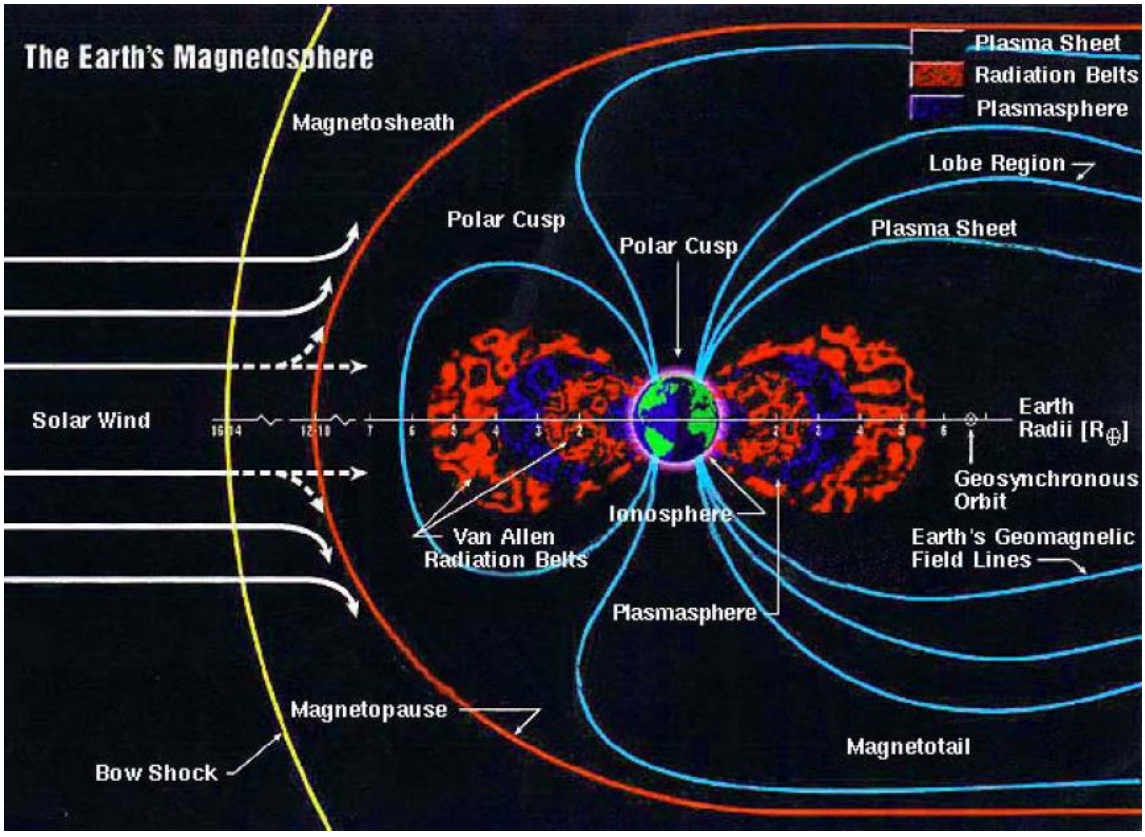

Fig. 1 . Van Allen belts surrounding the earth, fueled by solar winds and held in place by the earth's magnetic field. [17]

To guarantee that the electronics on-board satellites, robot exploration probes, and other space bound systems will have a robust operation in this extremely harsh environment, a detailed understanding of the radiation sources and their interaction with electronics on the device level, circuit level, and finally system level is essential. This allows researchers on each level to independently investigate methods of mitigating and overcoming these radiation effects leading to a radiation-hard design that can withstand the harsh environment in space and operate robustly regardless.

1.1.2. SiGe HBT BiCMOS Technology Overview

The silicon-germanium heterojunction bipolar transistor (SiGe HBT) is the first practical bandgap-engineered device to be realized in silicon, and effectively combines transistor performance competitive with III-V technologies with the economy-of-scale of conventional silicon IC manufacturing. Since the first demonstration of a functional transistor in 1987, SiGe technology has entered manufacturing across the world, and is currently making in-roads in a number of venues associated with the global electronics infrastructure.

In many ways, SiGe HBTs represent the ideal mixed-signal device. SiGe HBTs possess excellent frequency response at useful breakdown voltages, extremely large transconductance per unit area, very high gain, very low output conductance, very low broadband noise, very low 1/f noise, very low phase/jitter noise, good RF linearity, excellent power handling capability, extremely high current drive, good thermally stability, the ability to operate across very wide temperature ranges (4K to 300C), and inherent tolerance to ionizing radiation. All at very conservative lithographic nodes (typically with a two-generation advantage over CMOS at fixed performance). Importantly, SiGe HBTs can also be easily integrated into core foundry-compatible CMOS platforms to address an optimal HBT/CMOS division of labor for highly-

integrated electronic systems. At the state-of-the-art, SiGe HBTs exhibit frequency response above 300 GHz at 300K (at 130 nm), and above one-half TeraHertz (500 GHz) at cryogenic temperatures, with significant untapped performance remaining.

Integrated circuits (ICs) fabricated in SiGe HBT BiCMOS technology are utilized in a wide range of applications, including but not limited to, global positioning systems (GPS), cellular handsets, wireless local area networks (WLAN) building blocks, and radar systems in the 3 GHz to 77 GHz frequency range [18] and mmW imaging. Fig. 2 provides a visual overview of the application frequency bands for SiGe HBT BiCMOS technology.

The current and projected f_T and f_{max} values for SiGe HBT devices provided by different foundries are displayed in Fig. 3. The increase of f_{max} up to several hundred gigahertz demonstrates the capability of this technology to provide power at such high frequencies that is crucial for practical applications. The overall increasing trend in f_T and f_{max} are a result of advancements in device scaling methods and advanced fabrication techniques.

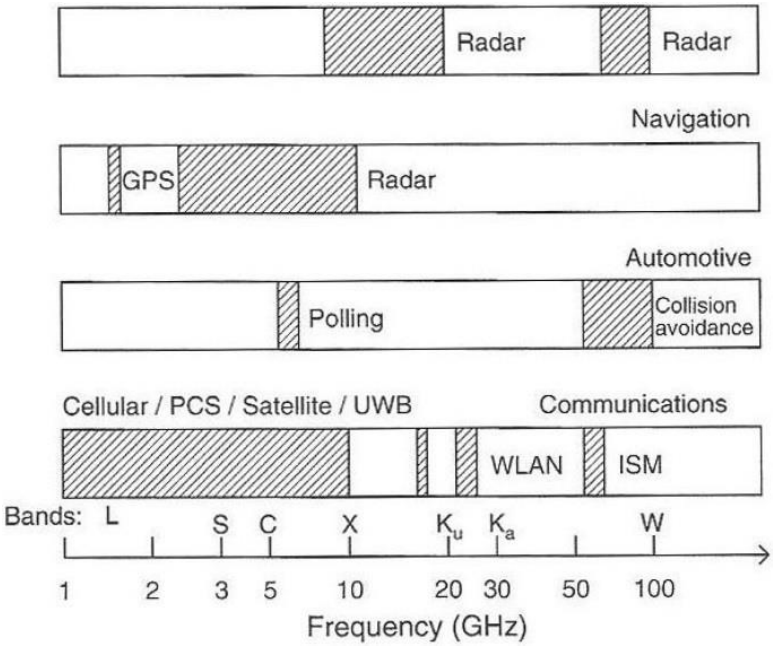

Fig. 2. Application frequency bands for SiGe HBT BiCMOS technology. [18]

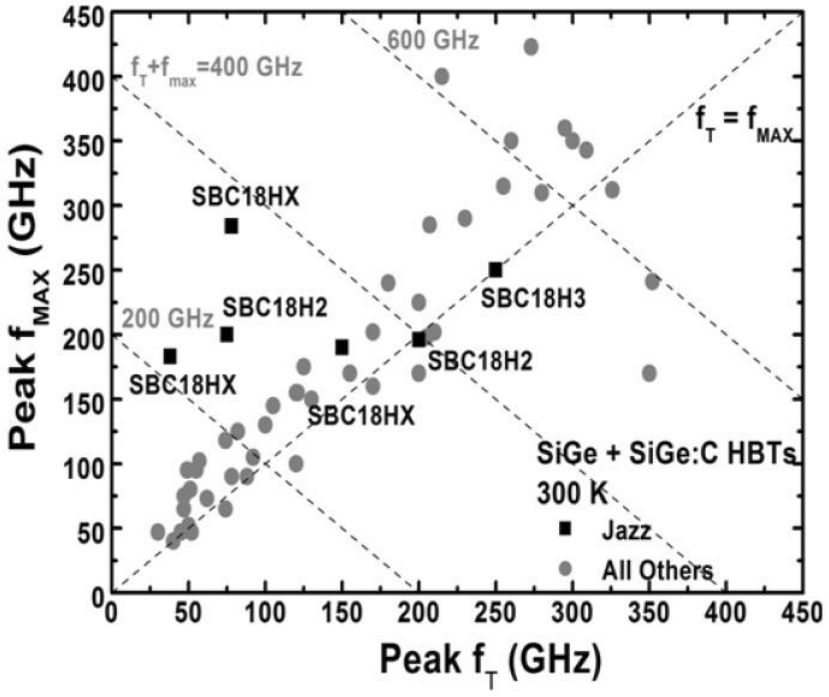

Fig. 3. The evolution of f_T and f_{max} for SiGe HBTs across many generations, along with future projections. [19]

1.2. A 1.0 V, 10-22 GHz, 4 mW LNA Utilizing Weakly Saturated SiGe HBTs for Single-Chip, Low-Power, Remote Sensing Applications

Development of advanced radar systems for emerging remote sensing applications necessitates next-generation receivers with wideband frequency capabilities. Furthermore, limited access to power in such applications, due to autonomous operation, together with constrained physical parameters (e.g., weight and size), which limit overall power harvesting capabilities, requires a receiver system with ultra-low power consumption. The first active building block in such a receiver chain is the low noise amplifier (LNA), the performance of which (e.g., input matching, NF, and gain) has a critical impact on the overall system performance. The proposed 4-mW LNA, with its wideband coverage that spans X-band (8-12 GHz), Ku-band (12-18 GHz), and K-band (18-26.5 GHz), make it an ideal match for aerial and space-based pulsed radars aimed at remote sensing applications. Fig. 4 displays an example of such a tactical aerial remote sensing application that requires ultra-low power consumption.

Conventional radar transceiver (TR) modules are designed using discrete components, making them very power inefficient. In addition, the sensitivity of these discrete components to power supply, temperature, and process variations can limit the

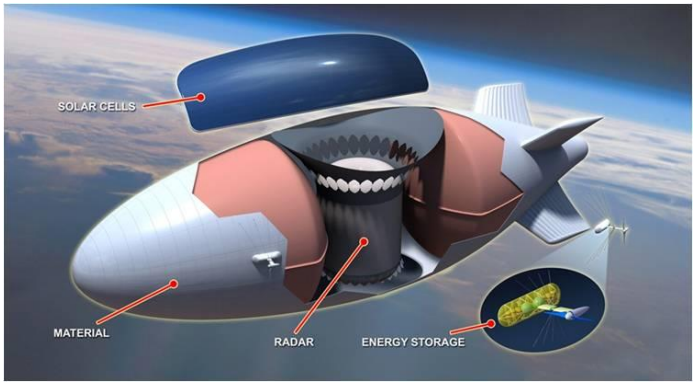

Fig. 4. DARPA ISIS Program vision: Lockheed Martin High Altitude Airship concept. [20]

performance of the TR. [21]

Integrated single-chip radar systems enable high performance within a compact form factor, as well as reduced power consumption.

Low power LNAs implemented in a variety of platforms have been reported, with III-V technologies (e.g., InP-HEMT), presently leading in performance with sub-milliwatt power consumption and NF of less than 2.0 dB [22]. Despite the attractive low-power performance of such III-V technologies, the associated high cost, driven mainly by low yield, and more importantly their incompatibility with the integration levels associated with standard CMOS processes, hinders their application in systems. Silicon-germanium (SiGe) technology is an attractive candidate to satisfy both high performance and low cost constraints. SiGe heterojunction bipolar transistors (HBTs) offer a dramatically higher performance compared to conventional Si bipolar junction transistors (BJTs) as a result of bandgap engineering, while maintaining strict compatibility with low-cost CMOS implementations [19]. However, low-power and low-voltage constraints must first be addressed in the design methodology.

The present work demonstrates the design of a 1-V, 10-22 GHz, 4-mW LNA in SiGe BiCMOS technology, by utilizing the modest low-power performance of weakly saturated HBTs. Weakly-saturated SiGe HBTs have been shown to demonstrate decreased but still acceptable levels of power gain, along with good noise performance and favorable characteristics under low-temperature operation [23]. The 1-V supply operation of the proposed LNA paves the way towards such a single-chip, inexpensive, low-power receiver for portable wideband digital radars.

1.2.1. LNA Design

The proposed LNA is depicted in Fig. 5 along with a die micrograph in Fig. 6, and consists of two stages. The first stage, consisting of Q_{1a} and Q_{1b}, adopts a current-reuse topology to take advantage of simultaneous noise and power matching under a reduced power budget. A current-reuse amplifier, in essence, is composed of two common-emitter (CE) amplifiers that are stacked in order to use the same bias current. In Fig. 5, the input signal, after passing through the first CE stage (Q_{1a}), is routed to the base of Q_{1b} through C_c (L_{1a} provides and *ac* open) and thus is amplified by the second CE stage (C_c provides an *ac* ground at the emitter of Q_{1b}). As a result, a current-reuse amplifier provides nearly twice the gain of a cascode amplifier at the same bias current and voltage supply, thus improving the overall gain and *NF* of the LNA, when used as the first stage. This makes it an especially attractive choice for low-power design; however, it is known to suffer from poor reverse isolation. To improve the overall reverse isolation as well as to improve gain, the second stage of the LNA (Q_{2a}, Q_{2b}) is implemented as a cascode topology.

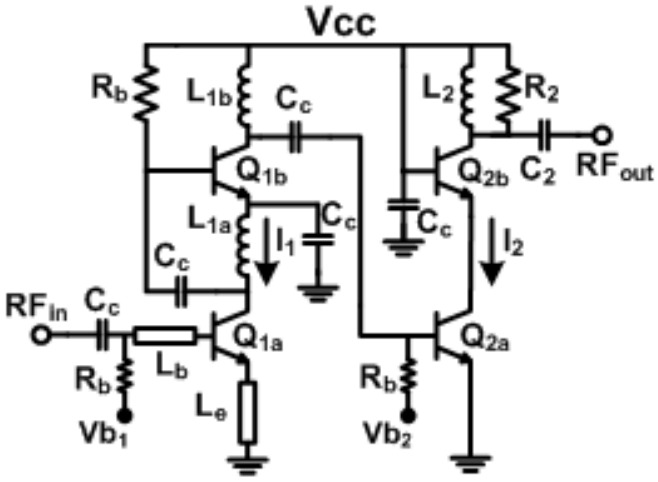

Fig. 5. 1-V LNA circuit schematic consisting of a current-reuse and a cascode topology for the 1st and 2nd stages, respectively.

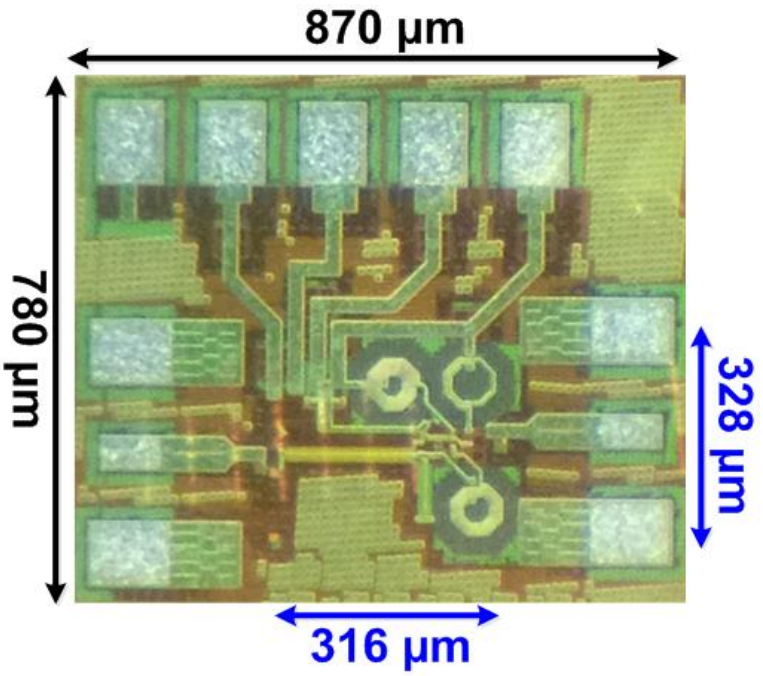

Fig. 6. Die micrograph of the SiGe 1-V wideband LNA.

Power and noise matching were accomplished using the guidelines described in [19], which includes optimizing Q_{1a}'s collector current density (J_c) for optimal *NF* and gain. Furthermore, since the two lower HBTs (Q_{1a} and Q_{2a}) are intentionally biased in weak saturation, to allow for the intended low-voltage operation, it is important to take into account additional considerations to capture the effects of changes in collector-emitter voltage (V_{CE}) on gain and noise. Due to the *dc* configuration of the vertically stacked topologies (including current-reuse and cascode), if an equal base-emitter voltage (V_{BE}) is assumed for both devices, in this case Q_{1a} and Q_{1b}, V_{CE} for Q_{1a} will be lower than the supply voltage (V_{CC}) by a V_{BE} , when the base of Q_{1b} is tied to V_{CC}.

Fig. 7 displays the 16-GHz maximum gain under ideal matching conditions (G_{max}), minimum noise figure (NF_{min}), and J_c versus V_{BE} for a stand-alone *npn* SiGe HBT, in which V_{CE} has been set to a $(1.0\text{-}V_{BE})$ voltage value to account for the 1-V target supply and the resulting changes in V_{CE} with sweeping V_{BE}. In other words, V_{CE} decreases from 300 mV to 100 mV as a result of sweeping V_{BE} from 700 mV to 900 mV. As V_{BE}

increases from 700 mV the HBT gradually moves into weak saturation, reaching a G_{max} peak value of 11.9 dB, in Fig. 7, at a V_{BE} of 830 mV (V_{CE} of 170 mV), with a J_c value of 2.5 mA/μm^2 (peak f_T). Increasing V_{BE} further results in a sharp drop-off in gain as the device becomes increasingly saturated.

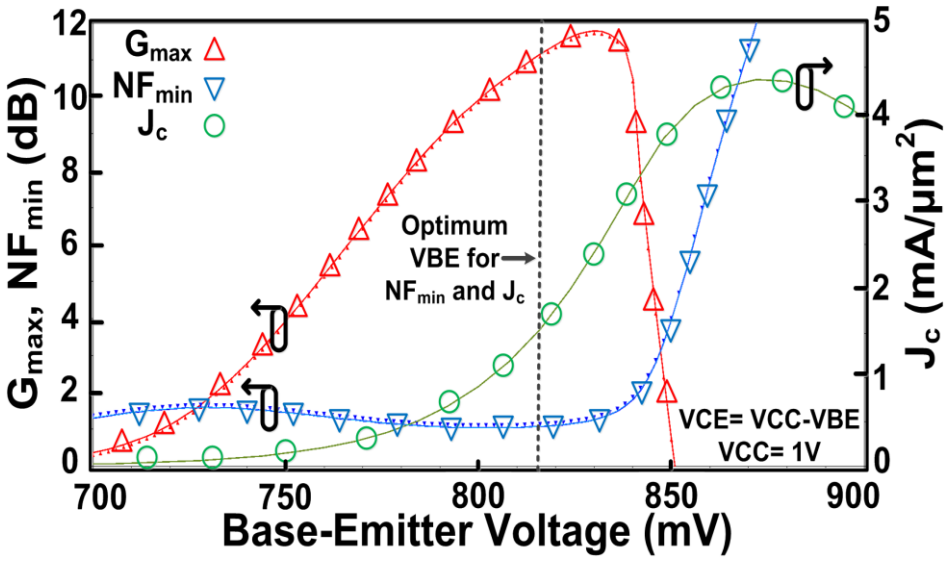

Fig. 7. Simulated 16-GHz G_{max}, NF_{min}, and J_c versus V_{BE} for the first device in the signal path in current reuse or cascode topologies (Q_{1a} and Q_{2a}) with 1-V supply.

It is important to note that in a traditional LNA design procedure, with sufficient voltage headroom and with the devices operating in forward active mode, G_{max} would continue to rise with V_{BE} beyond what is displayed in Fig. 7. In this case a peak of more than 20 dB at a V_{BE} of more than 900 mV (peak f_T) is obtained by exponentially increasing I_c by an order of magnitude. NF_{min}, on the other hand, will remain approximately constant and instead begin to increase (degrade) with increasing V_{BE} of more than 900 mV (peak f_T). This contrast essentially represents the voltage-gain-power tradeoff for designing SiGe HBT LNAs using weakly saturated devices. A lower device-level gain, at an exponentially lower current consumption and supply voltage, can be compensated by the use of a multi-stage design topology, which if optimized for power,

can result in significantly lower total power consumption at a constant total gain and noise performance. However, this lower power consumption comes at the cost of degradation in linearity due to the physical properties of the saturated SiGe HBT [23] and the multi-stage design topology. Furthermore, due to the sharp drop-off in gain with increased V_{BE}, as seen in Fig. 7, the design sensitivity to bias variations increases significantly.

Fig. 7 provides essential information for selecting the V_{BE} of Q_{1a} and Q_{2a}. Since Q_{1a} is the first active device in the signal path, V_{BE} is chosen at 816 mV in order to minimize NF_{min} and J_c (power consumption) while maintaining a safe margin from the G_{max} drop-off to assure a robust design, resulting in a chosen value of J_c = 1.5 mA/μm^2. Emitter length (L_E) for Q_{1a} was selected as 6.5 μm to match the optimum source resistance ($R_{s,opt}$) to 50 Ω [19]. This results in a collector current of 2.53 mA (I_1 in Fig. 5) for a double-emitter device with each emitter width (W_E) being 0.13 μm. Furthermore, L_e and L_b are designed to 65 pH and 100 pH, respectively, for noise and power matching. L_e and L_b are implemented as microstrip lines due to their inductor value scalability and high accuracy.

As for the second stage, J_c (for Q_{2a} and Q_{2b}) was designed based on the process utilized for the 1st stage, since the *dc* configuration of both stages is similar. However, design of the 2nd-stage (i.e., setting J_c, device sizes, and the output RLC resonant load) was aimed at achieving the target gain and bandwidth, unlike design of the 1ststage where NF_{min} and S_{11}, were the primary target specifications. This results in a 2nd stage I_c (I_2 in Fig. 5) of 1.47 mA, and L_E of 3 μm, adding up to a total current consumption of only 4 mA from a 1-V supply. Finally, the output resonant load component values of L_2 and C_2 are designed at 280 pH and 100 fF, respectively, with a reduced quality factor as a result of an added 100 Ω shunt resistor (R_2) used for the enhancement of wideband response. Importantly, careful consideration was attended during layout for minimal parasitics through the amplifier.

1.2.2. Measurement Results

The 1-V wideband LNA was implemented in a commercially-available 0.13 µm, 250-GHz peak f_T SiGe HBT BiCMOS technology, with core (without pads) and die sizes of 0.1 mm^2 and 0.68 mm^2, respectively (Fig. 6). The amplifier was characterized on-wafer with probe-level calibration in an RF shielded room. The S-parameters were measured using an Agilent E8363B PNA, and the 50 Ω noise figure was measured using a cold-source noise parameter method with Focus Microwaves automated tuners and software along with an Agilent E4446A spectrum analyzer.

Fig. 8 displays the measured and simulated gain (S_{21}) and *NF* of the designed LNA. It can be seen that a measured S_{21} of 15.5 dB is achieved at 16 GHz, while S_{21} has less than -3 dB variation across 10 GHz to 22 GHz, reasonably consistent with the simulated results. The *NF* is measured at 3.4 dB at 16 GHz, while *NF* at 20 GHz and 22 GHz could not be measured due to limitations in the noise measurement setup; however, close agreement between measured and simulated *NF* allows for a reasonable *NF* projection of 4.4 dB at 22 GHz.

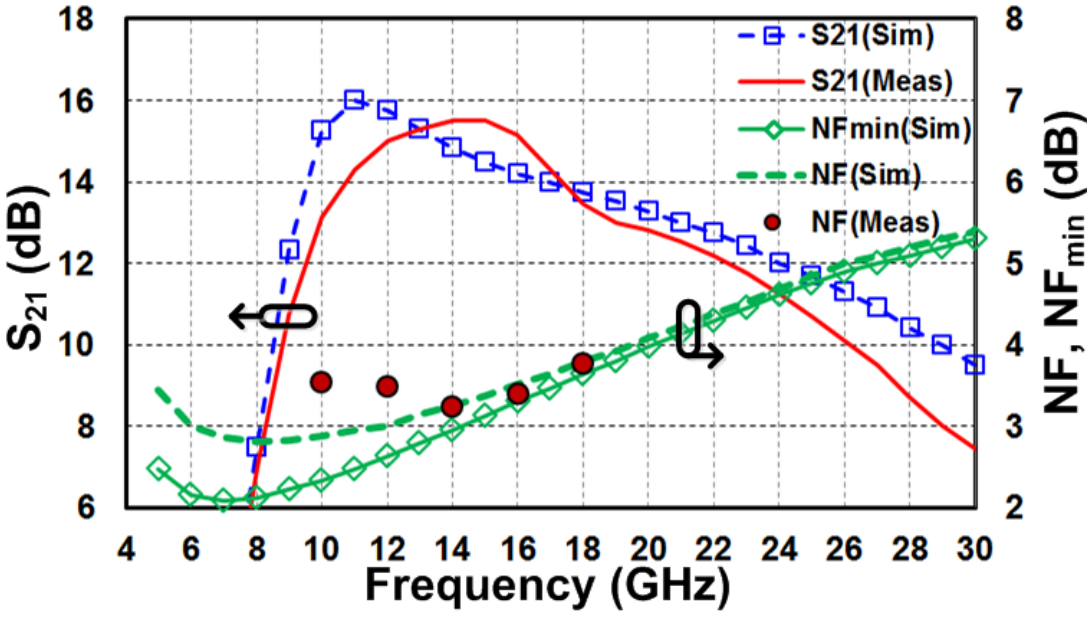

Fig. 8. Measurement and simulation results: (b) Gain (S_{21}), *NF*, and NF_{min} across frequency.

It should be noted that the difference in *NF* and NF_{min} values in the lower half of the operating range (10-16 GHz) is due to an intentional design tradeoff of noise for wideband input matching. *NF* and NF_{min} values differ by less than 0.1 dB for the upper half of the operating range (16-22 GHz).

The measured input reflection coefficient (S_{11}) of the LNA is shown in Fig. 9 and is well-matched to below -7.5 dB over the entire operation band of 10-22 GHz (-9 dB at 16 GHz). The measured S_{11} upwards spike at 10-12 GHz and the simulation-measurement mismatch in *NF* at the same frequencies are as a result poor reverse isolation at the output of the first stage, which causes the input matching to be very sensitive to the values of elements at this output, especially L_{1b}. Since the LNA is not designed for stand-alone functionality and is aimed for use in an integrated Rx module where conjugate inter-block matching will be implemented (or a simple low-power output buffer can be implemented), 50-Ω matching was not a design criteria and thus S_{22} is presented here only for the sake of completeness of the reported results (e.g., to show low-frequency stability of the design).

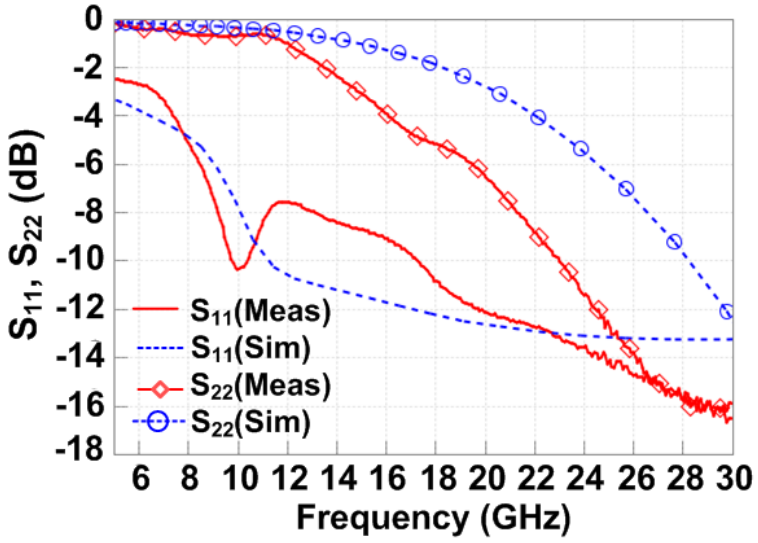

Fig. 9. Measurement and simulation results for input and output reflection coefficient (S_{11} and S_{22}) across frequency.

Fig. 10 presents the measured S_{21} for half-bandwidth functionality of the designed LNA, when the second stage current is reduced to 0.52 mA from 1.47 mA as a result of reduction in 2nd stage gain which was optimized for increased bandwidth.

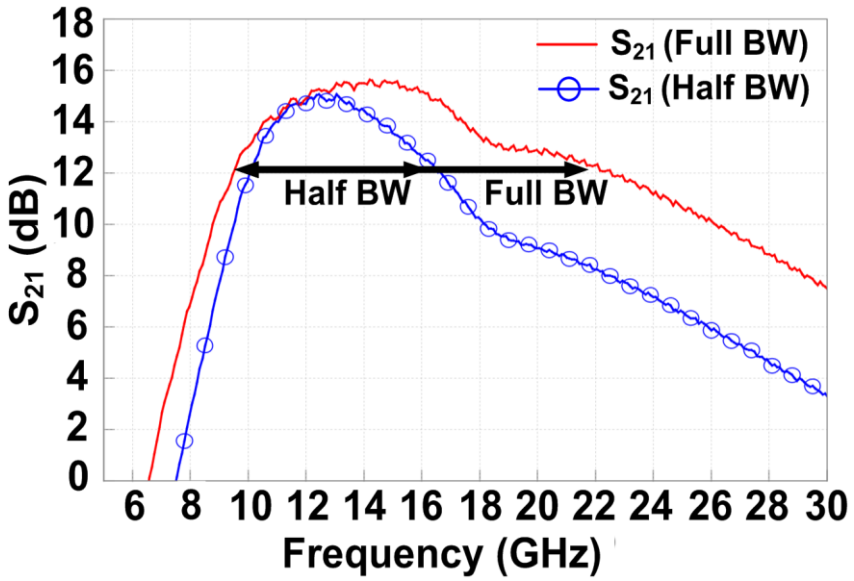

Fig. 10. Measured gain (S_{21}) across frequency for full-bandwidth mode (10-22 GHz) and half-bandwidth mode (10-16 GHz).

Finally, the OP_{1dB} and *OIP3* of the LNA were measured to be -22 dBm and -17 dBm, respectively. Stringent linearity requirement are imposed on the LNA in full-duplex radar transceivers that use the same antenna for simultaneous transmit and receive operation. Due to this simultaneous operation (leakage), these radars are susceptible to cross modulation distortion of undesired signals in the receive band [24]. Half-duplex (pulsed) transceivers, on the other hand, which only transmit or receive at any given time, don't have this stringent criterion [25]. As a result, linearity can be traded off, to a certain extent, for low-current/voltage operation by using saturated HBTs and a multi-stage design topology.

1.2.3. Summary

A wideband low-voltage/power SiGe HBT LNA is implemented aimed at integrated pulsed radar systems for remote sensing applications. The LNA design consists of a current-reuse 1st stage and a cascode 2nd stage. 1-V supply operation is achieved by intentionally biasing the SiGe HBTs in weak-saturation while accounting for additional considerations in the design procedure to capture consequential performance changes not applicable in a classic design with sufficient voltage headroom. Table 1 summarizes the LNA performance and its comparison against other state-of-the-art wideband LNAs. The performance is achieved at a power consumption of only 4 mW from a 1-V supply, which to the authors' best knowledge is the lowest power consumption for a wideband LNA operating over a similar frequency band. Finally, the LNA figure-of-merit (FoM) provides insight into the performance of Si-based LNAs for pulse-based radar applications (a larger FoM is better). It is important to note that for continuous wave radar applications linearity should be included in this FoM.

Table 1
COMPARISON of SI-BASED LOW-POWER WIDEBAND LNAs

Reference	***BW (GHz)***	***S_{21} (dB)***	***NF (dB)***	***Power (mW), V_{CC} (V)***	***IIP3 (dBm)***	***FoM***	***Tech***
[26], TMTT 2010	1.6-28	9.6	2.9-4.4	21.6, 1.2	4	0.57	90-nm CMOS
[27], MWCL 2009	0.1-20	11.2	3.3-5.5	20.4, 1.2	-2.5	0.7	90-nm CMOS
[28], RFIC 2009	0-22	9.2	4.3-6.6	8.4, 1.2	-2.7	0.79	90-nm CMOS
[29], IMS 2009	8-18	16.0	5.0-6.0	38, 2.2	-14	0.31	130-nm SiGe
This work	**10-22**	**15.5**	**3.2-4.4**	**4.0, 1**	**-33**	**4.78**	**130-nm SiGe**

$$FoM = \frac{Gain\ (Magnitude).BW(GHz)}{[NF(Magnitude) - 1]\ .f_c\ (GHz)\ .Power\ (mW)}$$

1.3. An Investigation of Total Ionizing Dose Damage on a Pulse Generator Intended for Space-Based Impulse Radio UWB Transceivers

UWB radios, with roots that originate from Marconi's spark gap radio, today are defined by the Federal Communication Commission (FCC) as having transmitting spectrum with -10 dB bandwidths greater than 500 MHz. In addition, within the 3.1-10.6 GHz UWB band, transmitter power is limited to less than -41.3 dBm/MHz [30]. UWB designs have increased significantly since the FCC's 2002 ruling that deregulated the use of UWB for low power communications. One such variation, known as IR-UWB, communicates data via the modulation of narrow pulses, thus offering significant advantages for low-power and low-complexity transmitter design (and with modest receiver specifications) [31]. This is due to the transmission of narrow pulses, as opposed to a traditional carrier-based system, in which the data is transmitted through the modulation of an RF carrier signal. In addition, in this carrier-less communications scheme, power-hungry frequency stabilization blocks such as phase-locked loops (PLLs) can be eliminated, contributing to a much lower power design [32]. These attributes have made IR-UWB an attractive choice for a wide range of battery operated or battery-less applications where energy is critical, including radio-frequency identification (RFID) tags, wireless USB, and personal area networks (PAN) [33], [34]. In 2007, an amendment to the low-data-rate 802.15.4 standard was approved to add UWB signaling as a physical layer option [35]. This amendment is designed specifically for ultra-low-power radios and supports any UWB pulse shape as long as it matches the reference pulse. The UWB physical layer can operate at a 110 kb/s, 851 kb/s, 6.81 Mb/s, and 27.24 Mb/s.

In IR-UWB, data is modulated by varying the amplitude, position, and/or polarity of the pulses, respectively known as pulse amplitude modulation (PAM) and pulse

position modulation (PPM). In a specific variation of PAM, the data is modulated by the presence or absence of the pulse known as “on-off keying” (OOK).

The IR-UWB transmitter can be categorized based on how the pulse is delivered to the antenna [31]. In designs such as those presented in [36] and [37], the pulse is delivered to the antenna by analog amplification through a power amplifier, as opposed to digital designs where digitally-generated edges and pulses are buffered to drive the 50Ω load and associated parasitics, such presented in [38] and [39]. Analog amplification allows for simpler pulse shaping at the cost of dissipating high amounts of static power. Digital buffering, on the other hand, only dissipates dynamic power and thus is more favorable for low-power designs, although robust pulse shaping is more difficult to achieve. Most digital designs consist of some variation of delay cells and edge combiners.

The UWB receiver architecture can adopt a non-coherent or coherent scheme, the former being a lower power and less complicated choice, with the caveat of lower achievable data rate (but still with enough for the present application) compared to the former. Such UWB receivers apply an energy-detection scheme in which the signal’s energy is captured by down-converting it to base-band and then detecting it using a comparator [40].

It is well-established that SiGe HBTs possess a favorable tolerance to total dose radiation exposure [41]-[44] and the ability to operate well across an extreme range of temperature. This, along with their excellent RF performance [45], provides a clear motivation to select a SiGe BiCMOS technology as the platform for a space-based UWB transceiver, since it can, in principle, be used outside of the WEB and thus dramatically improve mission SWaP. In this scenario, the power generating portion of the IR-UWB transmitter is implemented in SiGe HBTs, and the pulse generator and other support circuitry in CMOS, representing an ideal division of labor. In the present work, we investigate, for the first time, total dose effects on the pulse generator, which is the main

component of such an envisioned BiCMOS IR-UWB transmitter (Fig. 11). Due to the low-power nature of the application space, the digital approach has been selected for the pulse generator architecture, similar to that utilized in [38] and [39]. The pulse generator was fabricated in Jazz Semiconductor's SBC18-H3 SiGe BiCMOS process technology, which combines 250 GHz SiGe HBTs and 180 nm CMOS, and has a 6-layer metal stack-up. Total dose effects were examined using 10-keV X-rays.

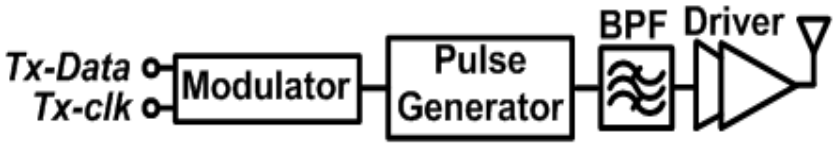

Fig. 11. UWB transmitter block diagram.

1.3.1. Device Technology and UWB-pulse-generator Design

The UWB pulse generator was designed to generate pulses with widths ranging from 50 ps to 60 ps while terminated by a 50 Ω load. Fig. 12 displays the schematic for the pulse generator, which consists of delay cells, edge-combiner, and a pull-up inductor. The pull-up inductor and the active area of the circuitry have been indicated in the chip micrograph in Fig. 13 (the design is pad limited). The delay cell includes a current-starved inverter, the current for which is provided by M_p and M_n for rising and falling output edges, respectively. M_p and M_n act as current mirrors, replicating I_{bias}. Thus, through I_{bias}, the current provided for the inverter, and as a result its delay, can be controlled within a certain range. The edge-combiner is composed of three nFETs, and an inductor for pull-up. As it is shown in the timing diagram in Fig. 12, as the input travels through the delay cells, the edge combiner preforms a NAND operation on the buffered *A* and *B* signals (*B* is the inverted-delayed version of *A*), generating a single pulse. In other words, when the two bottom nFETs in the edge combiner are off, the inductor and the nFET connected to it, which acts as a resistor, keep V_{pulse} at a voltage level of $Vdd - V_{TN}$. On the other hand, when the two bottom nFETs turn on for the short duration in

which *A* and *B* signals are both high and thus equal to t_d (depicted in Fig. 12), they will conduct current that results in a voltage drop in V_{pulse}, generating a pulse. The amplitude of this pulse, V_p, is highly dependent on the width of the nFETs that *A* and *B* are fed into, and the width of this pulse, t_{pw}, is equal to the propagation delay of the delay cell, t_d. Since, t_d is proportional, within a certain range, to the current passing through the delay cell, and this current is a replicated version of I_{bias}, t_{pw} can be controlled through I_{bias}. The *Vdd* for this design is 1.8 V.

1.3.2. Experimental Details

The UWB pulse generator die were first measured and then irradiated up to 3 Mrad (SiO_2) using a 10-keV X-ray source (at a dose rate of 31.5 krad/min) at room temperature with all terminals grounded. The irradiated die were re-measured at intermediate dose points soon after exposure to minimize any potential annealing effects. The time-domain waveforms were obtained using a 50 GS/s oscilloscope. All measurements were performed on-wafer and at room temperature.

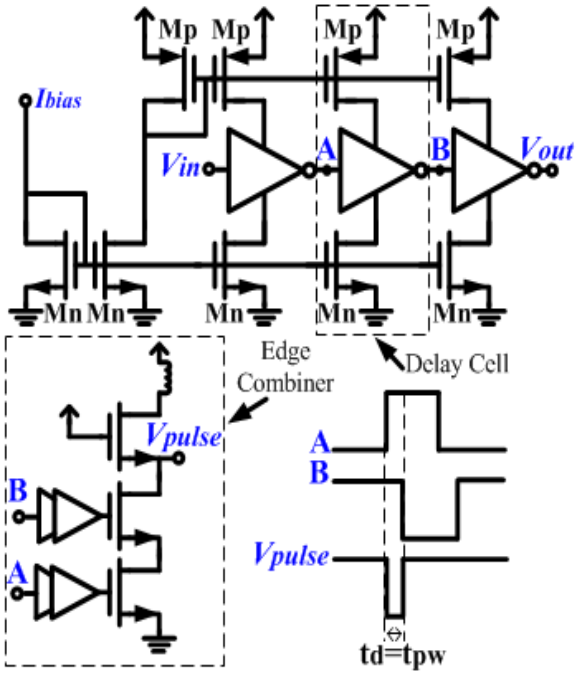

Fig. 12. Schematic diagram of UWB CMOS pulse generator along with its timing diagram.

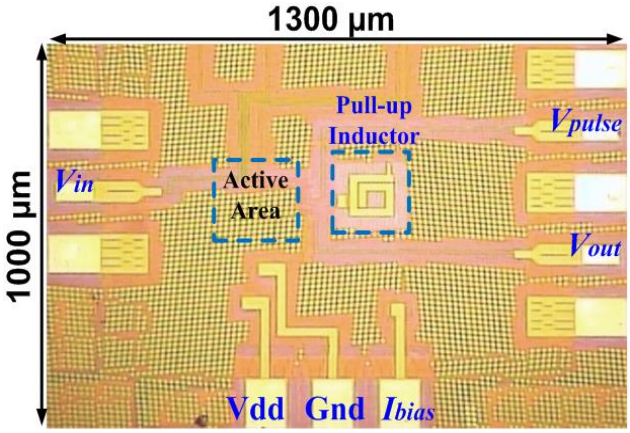

Fig. 13. Pulse generator chip micrograph.

1.3.3. UWB Pulse-generator-radiation Effects

Fig. 14(a) displays an inverted pre-rad measured pulse with t_{pw}=56 ps at I_{bias}=10 µA. This pulse is generated by performing a NAND operation on a 500 MHz clock fed into V_{in} and an internally generated delayed copy of the clock signal. Fig. 14(b) presents the inverted measured pulse after the pulse generator has been exposed to 1.0 Mrad of total dose radiation. By comparing Fig. 14(a) and (b), the effects of irradiation on the performance of the pulse generator can clearly be observed. The 1.0 Mrad radiation has caused t_{pw} to nearly double from its pre-irradiation value of 56 ps (Fig. 14(a)), to its post-radiation value of 136 ps (Fig. 14(b)). It should be noted that t_{pw}, by convention, is measured at half of the peak amplitude value (V_p/2). Another specification that has also been affected by the radiation exposure is the slight increase of V_p from 17 mV to 20 mV.

Fig. 15(a) depicts t_{pw} as a function of I_{bias} at several different TID values. In the pre-irradiation sample, t_{pw} is ~56 ps at I_{bias}=10 µA and can be decreased to ~ 49 ps by increasing I_{bias}. These values vary, however, as a function of dose. For example, at 1 Mrad, t_{pw} at I_{bias}=10 µA is 136 ps, which is more than twice the pre-irradiation value. In addition, from Fig. 15(a) it can be seen that although the radiation affects t_{pw}, this effect can be mitigated by the control that the design provides over t_{pw} through I_{bias}. Fig. 15(b) displays the less significant, but also important, effect of radiation on V_p. It can be seen

that the different doses follow the same trend, exhibiting a ~25% increase in V_p after radiation exposure. Another interesting TID effect, better depicted in Fig. 15(c), is the rebound and decrease of t_{pw} as the total dose is increased from 1.0 Mrad upward, after t_{pw} increases with total dose up to 1.0 Mrad.

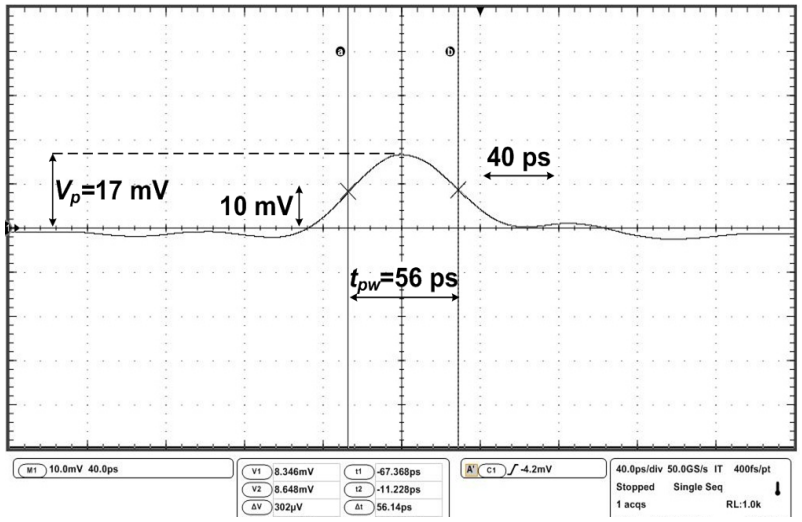

(a)

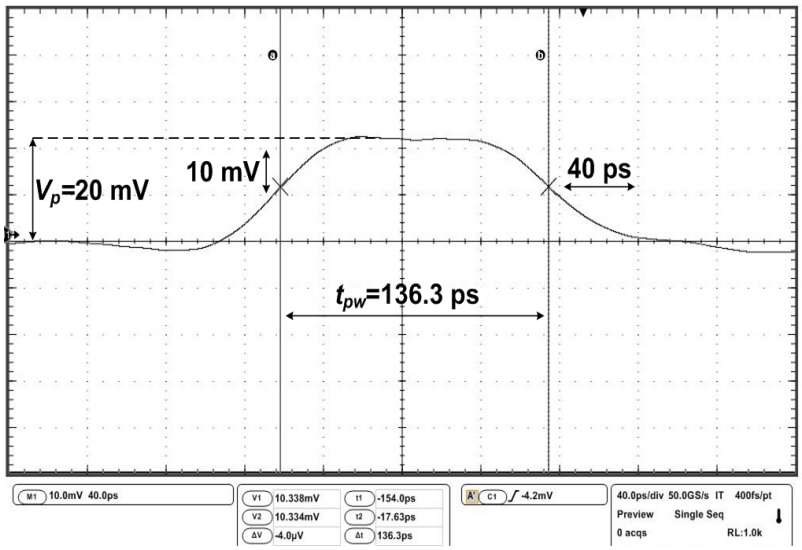

(b)

Fig. 14. (a) Inverted-measured pre-radiation waveform of a pulse with t_{pw}=56 ps at I_{bias}=10 μA. (b) Inverted-measured 1.0 Mrad post-radiation waveform of a pulse with t_{pw}=136.3 ps at I_{bias}=10 μA.

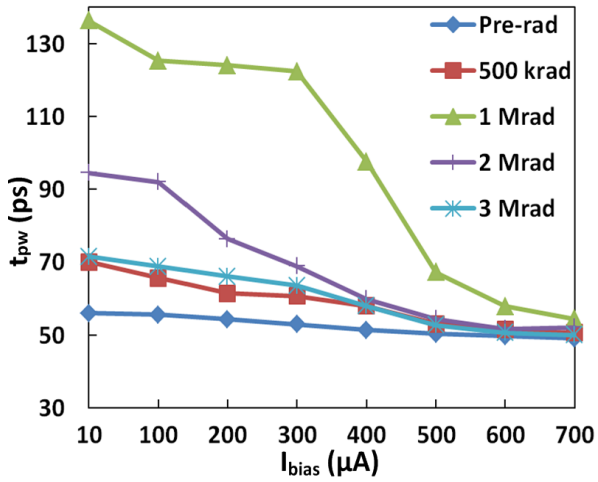

(a)

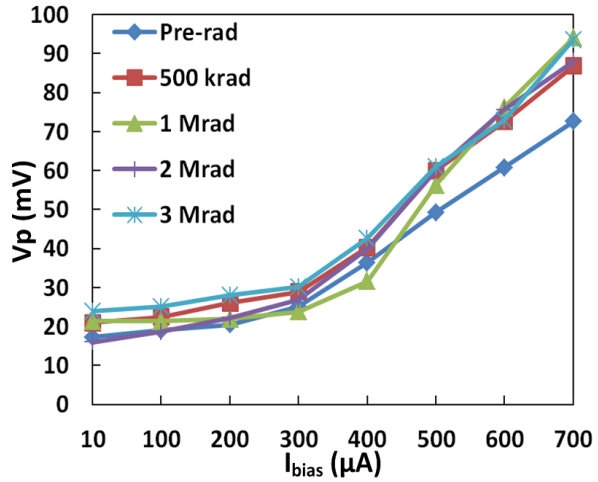

(b)

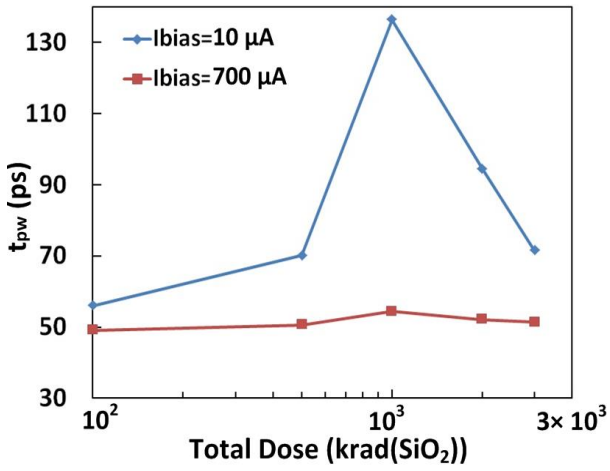

(c)

Fig. 15. (a) t_{pw} as a function of I_{bias} for different total-doses. (b) V_p as a function of I_{bias} for different total-doses. (c) t_{pw} as a function of total dose. The rebound effect can be seen beyond one Mrad.

To shed more light on these observations for the pulse generator total dose response, we also irradiated stand-alone nFETs (V_G=*Vdd*, V_S=V_D=V_B=*Gnd*). Fig. 16 (a), and (b) display the nFET drain current versus the gate-source voltage at different Xray, and proton radiation dosages, respectively. The dominant effects of TID in nFETs include an increase in off-state leakage current (Fig. 17(a)), and consequent reduction in subthreshold slope (Evident in Fig. 16), and shifts in the threshold voltage (Fig. 17(b)), both of which can contribute to changes in the t_d of the delay cells in the pulse generator, which in turn affects t_{pw} [46], [47].

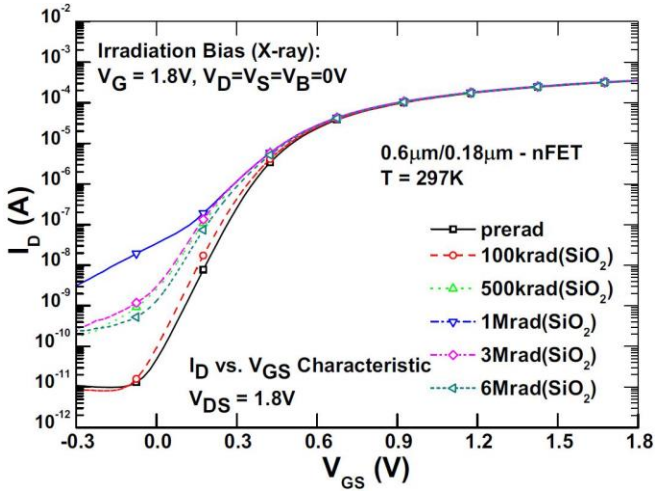

(a)

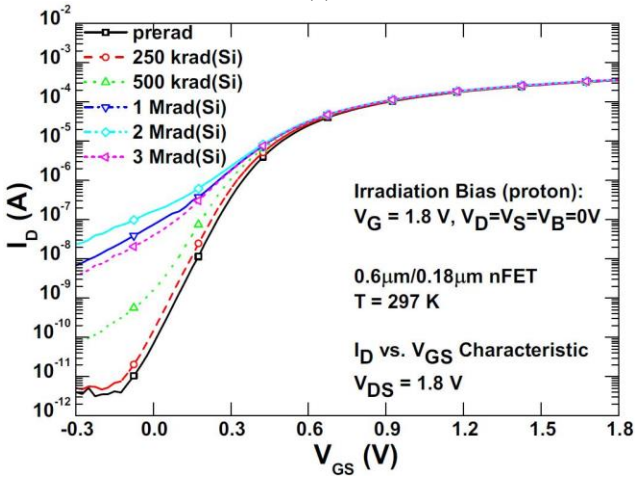

(b)

Fig. 16. (a) X-ray-induced degradation in narrow nFET at high V_{DS}=1.8 V, (b) Proton-induced degradation in a narrow nFET at high V_{DS}=1.8 V.

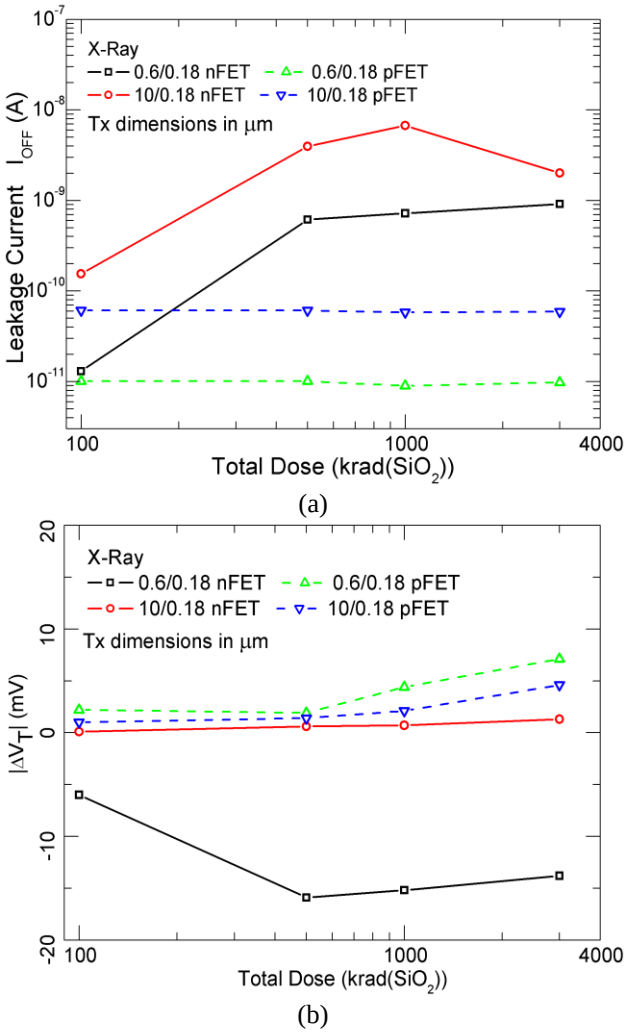

Fig. 17. (a) CMOS leakage current, (b) Threshold voltage as a function of total dose.

These effects are primarily caused by a buildup of positive charge in the various oxide layers of the device. For sufficiently-scaled CMOS-technologies with gate thickness on the order of a few nanometers, the charge trapped in the gate oxide itself is negligible, and thus, charge trapping in the shallow trench isolation (STI) oxide is the primary degradation mechanism. This has been demonstrated for another CMOS technology at an identical lithography node [48]. In the nFETs of the present SiGe BiCMOS technology, the absence of charge trapped in the gate oxide is confirmed by the lack of threshold voltage shift in the large transistors, which also indicates that the

apparent threshold shift in the small devices is caused by STI oxide effects. A well-known re-bound effect is also observed in the stand-alone devices as the negative charges associated with interface trap generation eventually compete with the positive charge in the bulk oxide, resulting in an apparent saturation or even annealing of the radiation effects. The radiation response of the present SiGe BiCMOS process technology has been fully characterized and described in greater detail in [49] . In addition, it is important to note that the main device within the delay cell that is responsible for radiation-induced changes in the circuit performance is the inverter n-FET, which determines the high-to-low transition at the output of each inverter. Since the current mirrors are all affected equally by the radiation, it is reasonable to expect their mirroring function to remain approximately unaltered.

At the circuit level, the increasing leakage current and the shift in threshold voltage results in an increase in propagation delay, which leads to an increase in t_{pw}. Fig. 17(a), (b) display the measured CMOS leakage current and V_{th} shift for both wide and narrow nFETs and pFETs at doses up to 3 Mrad (SiO_2). The trend of the V_{th} shift for a narrow nFET and nFET leakage current clearly resembles the t_{pw} trend in Fig. 15(c), with V_{th} shift, leakage current and t_{pw} increasing with increasing TID up to 1 Mrad. The rebound effect previously shown for t_{pw} at doses above 1 Mrad can also be seen here as the leakage current and V_{th} shift begin to decrease at sufficiently high total dose. This further confirms the presented findings in regards to the effect of TID on t_{pw} and the proposed explanation.

In addition, we re-simulated the pulse generator circuit while implementing the observed TID device-level changes within the nFET compact model. Since TID data for a stand-alone nFET with a width equal to the one that is used in the inverter (1 µm) was not available, and due to the fact that the devices were not irradiated at the bias points in which they operate at, a point-by-point comparison of measurement and simulations results was not possible. However, the simulation results confirmed the proposed

explanation for the cause of circuit performance TID effects trend based on device performance TID effects; namely, that threshold voltage shift increase is responsible for the observed lengthening of the delay with increasing dose. Furthermore, these simulations indicated a more significant impact of V_{th} shifts on t_{pw} variations compared to the radiation-induced changes in off-state leakage current.

1.3.4. TID Mitigation Strategies

The increase in $t_{pw,}$ if not appropriately compensated for, can cause degradation in the robust recovery of the data due to inter-symbol interference (ISI), which increases the total system-level bit-error-rate (BER). In addition, since t_{pw} determines the maximum data-rate that can be achieved, any variation in its value can negatively affect communication speed. The access the present design provides to I_{bias} allows for direct control of t_{pw}. For example, as is demonstrated in Fig. 15(a), a 1 Mrad exposure results in t_{pw} more than doubling in value at I_{bias}=10 µA. However, by increasing I_{bias} the value of t_{pw} can be decreased to its original pre-irradiation value, thus mitigating the negative effects on the communication link robustness and/or data rate (albeit, at somewhat higher power dissipation).

Mitigation strategies for TID-induced damage can be categorized as either static or dynamic (self-healing) methods. In static methods such as classical RHBD methods, the design is hardened against radiation through layout techniques that minimize the field oxide (FOX) transistors edge leakage effects. This is done, for instance, by designing the transistor to eliminate the edges altogether. Annular transistors [50] and enclosed transistors [51] are commonly used examples of such techniques. The drawback of such methods include imposing limitations on device connectivity in the layout, lack of compact models for such devices, increase of the minimum width for annular transistors (by a factor of four or five), and an increase in gate capacitance for enclosed transistors compared to standard devices with the same *W/L* [52]. The increase in minimum width

and gate capacitance, in particular, will significantly slow down these transistors and the associated circuits, and are thus highly undesirable in RF applications such as the one presented here.

In a dynamic or self-healing TID mitigating method [53], which have attracted significant attention recently, support circuit blocks are assigned the task of monitoring the main circuit's performance and adjusting for any changes in a closed loop fashion, through control knobs (usually for biasing) on the main circuit. In such methods, the control knobs are adjusted based on the observed circuit performance changes, which are a function of dose level. Such self-healing methods not only can be used to mitigate radiation damage, but in principle can also be used to compensate for any process variations or temperature changes [54]. The potential drawbacks of such methods are the over-head of the design and space associated with the support circuit blocks and their radiation hardening. However, since for real orbits, total dose damage accrues slowly, the support circuit blocks do not require high speed and thus classical RHBD methods can be applied to them. In essence, such an approach results in a hybrid TID mitigation strategy using both static and dynamic mitigation methods, allowing for high-speed RF applications. In addition, due to the slow nature of TID damage on the circuit, the support feed-back loop can be highly duty cycled, thereby not adding much power overhead to the overall system. Furthermore, the low-speed function of the feedback loop alleviates any stability issues, which can easily be addressed through a proper design methodology.

Fig. 18 depicts a potential "self-healing" scheme in which the circuit directly monitors t_{pw} and compensates for any radiation-induced changes to t_{pw} by varying the value of I_{bias} in a closed-loop manner. This compensation scheme is based on measuring the energy of a pulse, which is directly proportional to V_p and t_{pw}. Since the energy of one pulse is difficult to detect, an integrator is used to accumulate the energy of the several pulses and then provide it to the comparator for detection. The comparator reference voltage is set based on the expected value for the accumulated energy of N pulses with a

desired V_{p1} and t_{pw1}. Once the comparator detects the accumulated energy of several pulses and the output toggles, its value M is fed into a digital-to-analog converter which sets the value for I_{bias}. If the changes are due to radiation-induced t_{pw} increases ($t_{pw}>t_{pw1}$), the comparator will toggle at $M<N$, due to increased accumulated energy, triggering the circuit to adjust I_{bias} accordingly and returning t_{pw} to t_{pw1}. In this scheme, the variations in V_p are neglected due to being much less significant in value compared to the variations in t_{pw}, as demonstrated earlier.

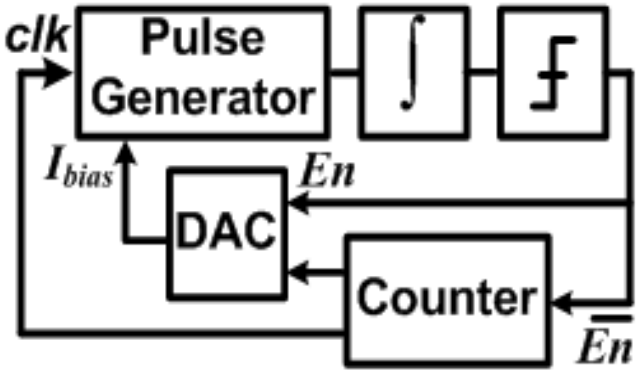

Fig. 18. Proposed adaptive TID compensation scheme.

1.3.5. Summary

We have investigated total dose effects on a CMOS UWB pulse generator aimed at space-based communications applications. The effects of TID on the pulse generator performance, mainly a variation in t_{pw} with increasing dose, have been demonstrated. We have provided an explanation for the circuit-level performance degradation by linking the observed response to well-known device-level TID effects in the component transistors. In addition, the degrading effects of these changes on the overall communication link performance have been described. Furthermore, possible mitigation strategies and their tradeoffs have been described. Finally a potential self-healing scheme for mitigating the radiation-induced changes is outlined, setting the stage for a future complete self-healing system.

1.4. Impact of Total Ionizing Dose on a 4th Generation, 90 nm SiGe HBT Gaussian Pulse Generator Technology

Development of advanced radars for high-altitude and space-based remote sensing is an emerging area of interest for applications such as tactical aerial surveillance, weather imaging, and space-based exploratory probes. Fig. 19 displays an example of such a tactical aerial remote sensing platform that has stringent constraints on size, weight and power (SWaP). SWaP specifications are key driving constraints not only in mission cost, but in mission science capabilities. Advances in integrated circuit (IC) technology can help meet SWaP goals, with the caveat being that one must still ensure robust operation in intense radiation environments and under wide-temperature swings. Traditionally, these issues were addressed by placing the electronics in a shielded and temperature controlled box (warm box) but this results in an increased SWaP overhead.

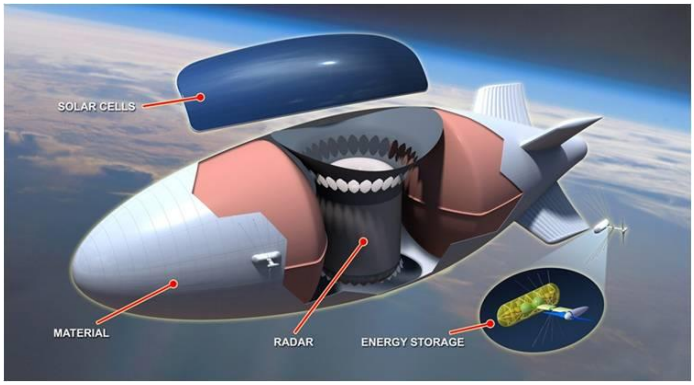

Fig. 19. DARPA ISIS Program vision: Lockheed Martin High Altitude Airship concept. [20]

Radars are categorized into continuous wave (CW) or pulse-based topologies, with the pulse-based radar offering low power consumption benefits due to its duty-cycled nature, at the cost of a "blind" period, which makes it unsuitable for the tracking of fast moving objects. In addition, pulsed radars are much more immune to interception and jamming due to their spread-spectrum nature. Pulsed radar, in effect, utilizes the time it takes for a transmitted short pulse to reflect off an object and travel back to the

transceiver as a measure of range. Fig. 20 displays a block diagram for such a pulsed radar. Due to its low-power benefits and due to the high spectrum efficiency of the Gaussian pulse shape, a Gaussian pulsed radar has been selected as the subject of this study.

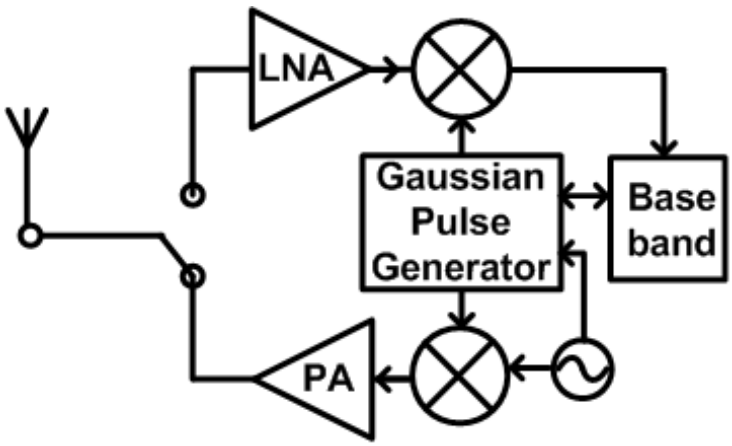

Fig. 20. Block diagram for a pulsed radar transceiver.

It is well-established that SiGe HBTs possess a favorable tolerance to total dose radiation exposure [41]-[44] and the ability to operate well across an extreme range of temperatures. These facts, along with their excellent RF performance [19], provide a clear motivation to select a SiGe BiCMOS technology as the platform for a space-based pulsed imaging radar transceiver. In this scenario, the microwave front-end portion of the radar transmitter is implemented in SiGe HBTs, and the digital baseband processing in CMOS, representing an ideal division of labor. In the present work, we investigate, for the first time, total dose effects on a SiGe HBT Gaussian pulse generator, which is the main component for a pulsed radar transmitter. Furthermore, as it will be explained in greater detail in the following section, the Gaussian pulse generator consists of two emitter-coupled logic (ECL) inverters, with the width of the pulse depending on the switching speed of these inverters. Therefore, the total dose effects on the Gaussian pulse

generator can also be considered as a measure of the ECL inverter's performance in radiation intense environments, which has implications for high-speed digital circuits.

Finally, it is important to note that this study is the first published TID investigation on a circuit implemented in IBM's new 9HP SiGe BiCMOS process. The Gaussian pulse generator was fabricated in this IBM 9HP SiGe BiCMOS process technology, which combines 300 GHz f_T SiGe HBTs and 90-nm CMOS devices. Total dose effects were examined using a 10-keV ARACOR X-ray source.

1.4.1. Gaussian Pulse Generator Design

The Gaussian pulse generator, as seen in Fig. 21, consists of two cross-coupled differential pairs (Q_1-Q_2, and Q_3-Q_4) and is driven by a ramp generator (V_r), while the two diff pairs are biased by two separate bias voltages (V_{b1} and V_{b2}) and current sources (I_{EE}). Pulses are generated at the rising and falling edges of V_r as the differential pairs switch following the well-established hyperbolic tangent law. Due to symmetric bias unbalancing, one of the differential pairs switches before the other resulting in a current that rises and falls to produce a current pulse. Given that large signal behavior of emitter-coupled pairs is modeled as a *tanh* function, the application of basic circuit theory to this problem yields *Vout* as,

$$Vout = 2RI_{EE}\left[\tanh\left(\frac{V_r}{2V_T}+a\right)-\tanh\left(\frac{V_r}{2V_T}-a\right)\right], \quad (1)$$

$$a=\frac{V_B-V_{B1}}{2V_T}, -a=\frac{V_B-V_{B2}}{2V_T}\ . \quad (2)$$

Equation (1) can be approximated as a Gaussian function, as given in (3), with less than 5% error if $a \in [0.5, 1.2]$ [55].

$$f\left(\frac{V_r}{2V_T}\right)=4RI_{EE}\tanh(a)\,exp\left(-\frac{\left(\frac{V_r}{2V_T}\right)^2}{\sqrt{2}\,\left(a+\frac{1}{2}\right)}\right) \quad (3)$$

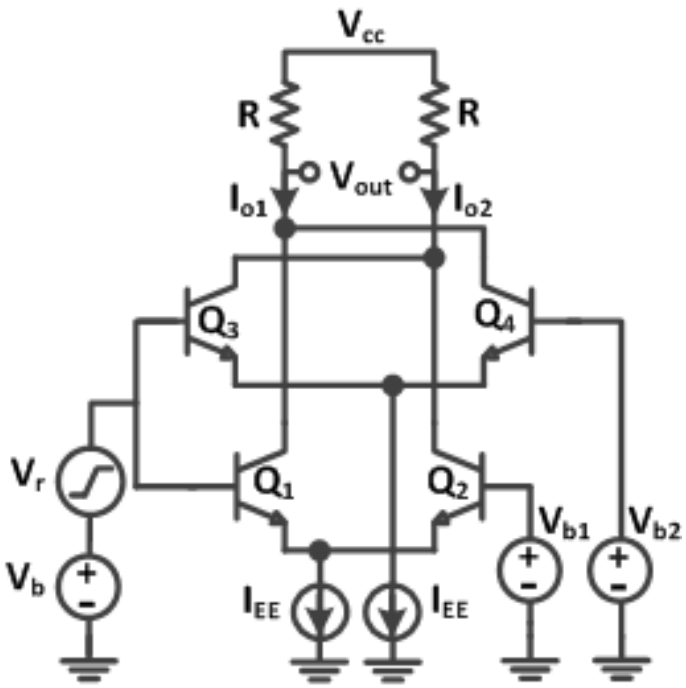

Fig. 21. Schematic diagram of a SiGe HBT Gaussian pulse generator.

Fig. 22 (a)-(d) display the measured waveforms for V_{out} as the value for a is increased from 0.5 to 2, in 0.5 increments. It can be seen that for a = 0.5 (Fig. 22(a)) the generated output pulse closely resembles a Gaussian waveform while it spreads out into an even distribution and away from a Gaussian for a = 2 (Fig. 22(d)). In the present design, the value for a is selected as 0.5 with a *Vcc* of 2.6 V. The input ramp function is generated by utilizing the linear area around the zero-crossing point of a sinusoidal through the application of a clipping circuit. Therefore, at constant amplitude, the increase in sinusoidal frequency results in an increase in ramp slope, thereby decreasing the pulse width according to (3).

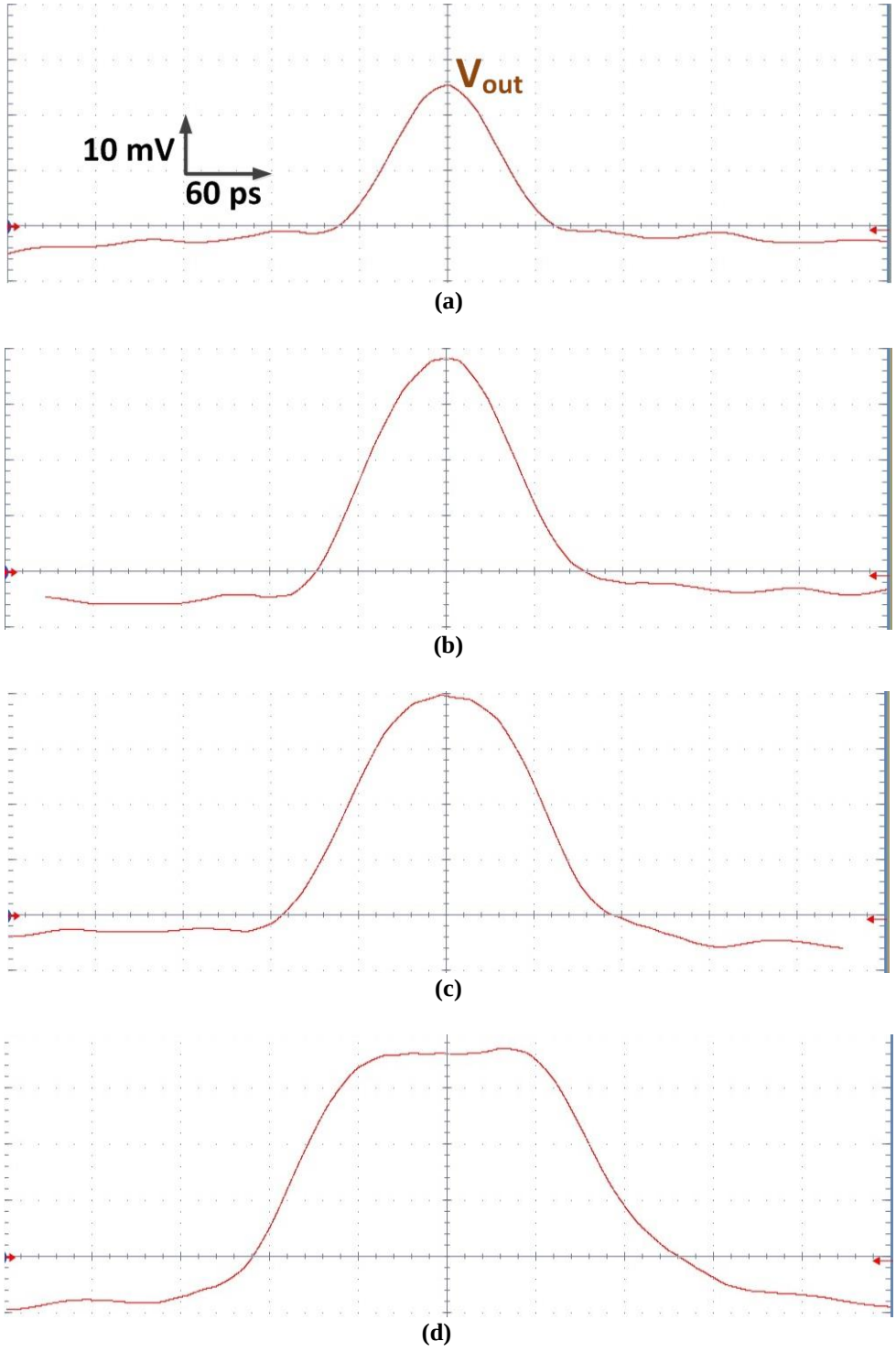

Fig. 22. (a)-(d) Measured pulse waveform for *a* values of 0.5, 1, 1.5, 2.

1.4.2. Experimental Details

Gaussian pulse generator die, a micrograph of which is displayed in Fig. 23, were first measured and then irradiated up to 3 Mrad (SiO_2) using a 10-keV X-ray source (at a dose rate of 31.5 krad/min) at room temperature, with all terminals biased at use conditions. The irradiated die were re-measured at intermediate dose points soon after exposure to minimize any potential annealing effects. The time-domain waveforms were obtained using a 50 GS/s oscilloscope and pulse width measurements were averaged across 5 samples. The input sinusoid was provided using an HP signal generator. All measurements were performed on-wafer, with 50 Ω termination.

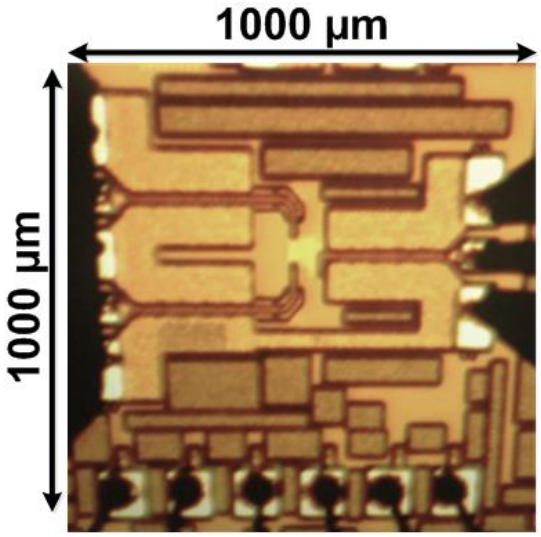

Fig. 23. Die Micrograph for the SiGe Gaussian pulse generator.

1.4.3. Radiation Effects

Fig. 24(a) displays the measured pulse width (t_{pw}) for the generated Gaussian pulse as a function of the input ramp frequency, which controls the slope for V_r in Fig. 21. It can be seen that pre-radiation measured t_{pw} decreases from 125 ps to 57 ps by increasing the ramp frequency from 250 MHz to 700 MHz, while 3-Mrad post-radiation values closely follow. The average values for t_{pw} at 250, 400, 550, and 700 MHz across the four die were measured to be 128, 74, 65, and 57 ps, respectively. Fig. 24(b) depicts

the normalized variation in t_{pw} across total accumulated doses at different t_{pw} values. It can be seen that the design is to a strong degree TID-tolerant, with a t_{pw} variation of less than 7% for total dose of up to 3.0 Mrad, and across different t_{pw} values ranging from 57 ps to 128 ps.

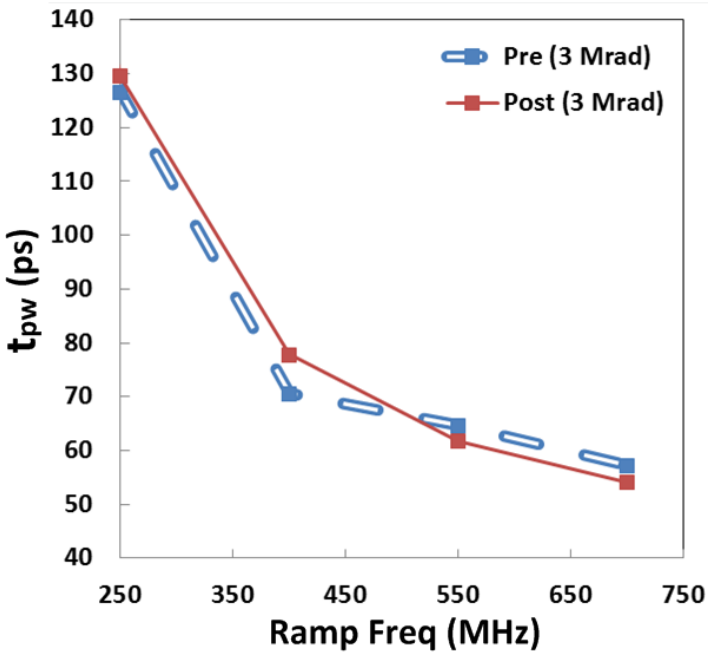

(a)

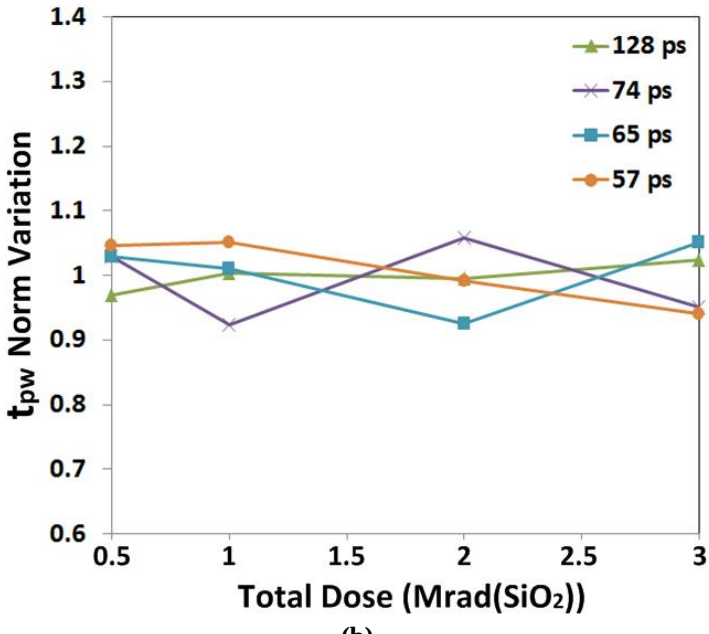

(b)

Fig. 24. (a) t_{pw} as a function of input ramp frequency, which controls the slope for V_r. (b) Normalized variation in t_{pw} across total accumulated dose at different t_{pw} values.

To shed light on the circuit-level TID response, the TID response (X-ray) of standalone SiGe HBT test structures was also characterized. The transfer characteristics (forward Gummel) for a 0.1 µm x 1.0 µm SiGe HBT are shown in Fig. 25(a). The HBT exhibits classical bipolar TID damage as seen through the increase in off-state input (base) current, which is attributed to the generation of G/R traps along the emitter-base spacer oxide interface. Fig. 25(b) shows that a steady increase in off-state base leakage up to a total dose of 3 Mrad (SiO_2). While this increase in base current results in a minor increase in power consumption, Fig. 25(c) shows that transconductance is not affected at functional biases (i.e. near peak f_T).These device-level measurements further confirm that IBM 9HP maintains the TID robustness of earlier SiGe HBT generations, while providing superior current gain and cutoff frequency, making it an attractive candidate for high-performance RF circuits.

Fig. 26 compares the TID performance of the SiGe HBT Gaussian pulse generator (consisting of ECL inverters), presented above, and that of a 0.13 µm technology CMOS pulse generator (consisting of standard CMOS inverter gates) presented in [56], at a similar t_{pw} value. It is interesting to note that in both cases t_{pw} is the function of the inverter switching speeds and thus has implications for digital design (beyond the stated RF application). It can be seen that the SiGe HBT pulse generator far outperformers the CMOS pulse generator under TID conditions, with t_{pw} more than doubling at 1.0 Mrad for the CMOS version while the SiGe HBT version varies by less than 5%.

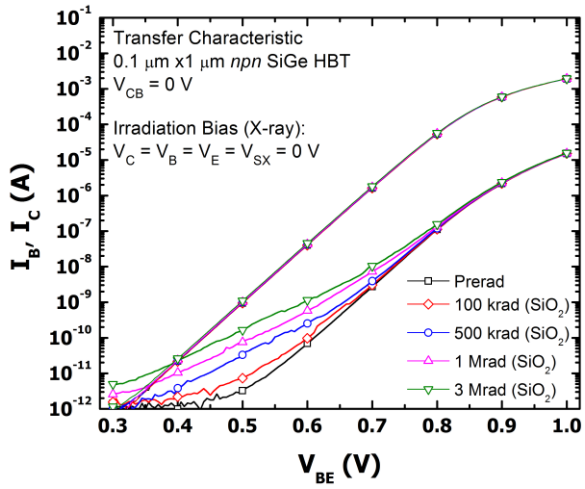

(a)

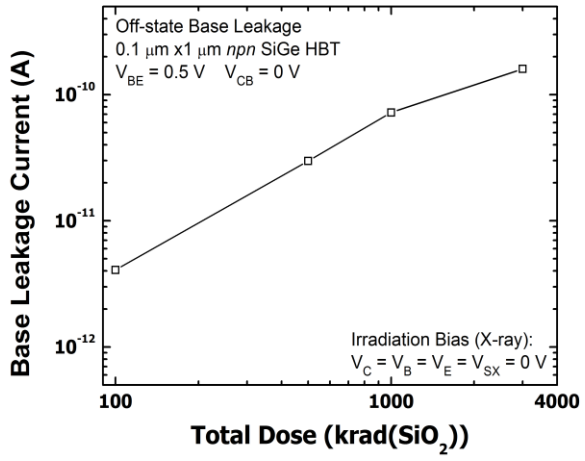

(b)

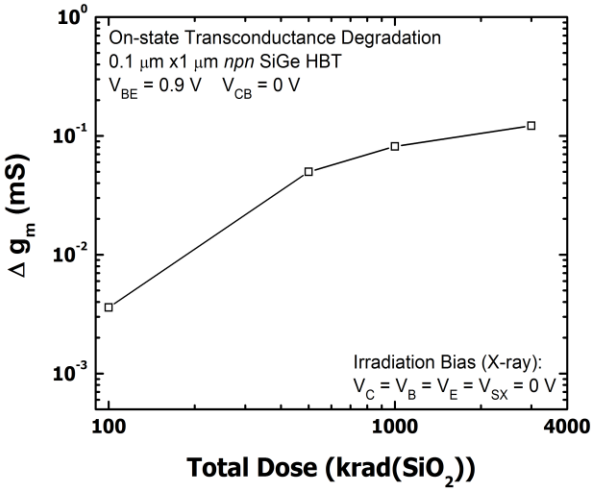

(c)

Fig. 25. (a) Forward-mode Gummel characteristics of 0.1x1.0 μm^2 IBM 9HP SiGe HBT. (b) Base leakage current, (c) Transconductance variation, as a function of total dose.

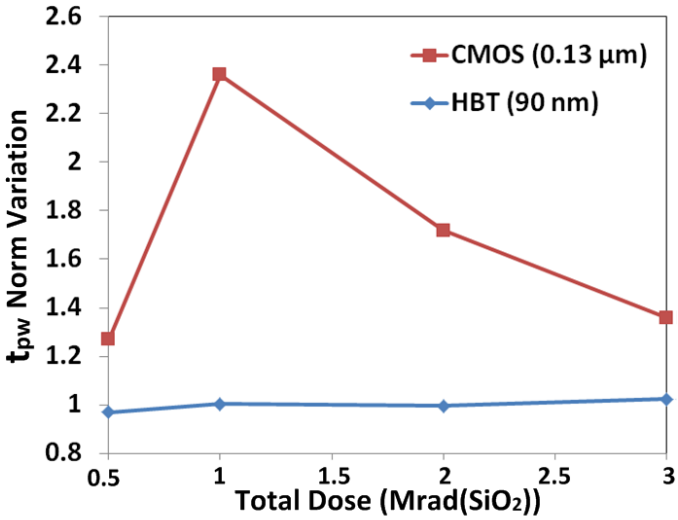

Fig. 26. Comparison of TID performance for HBT Gaussian pulse generator and CMOS pulse generator.

1.4.4. Summary

Total dose effects on a SiGe HBT Gaussian pulse generator implemented in IBM 9HP 90-nm SiGe BiCMOS process were investigated up to 3 Mrad, which covers virtually all orbital environments. The Gaussian pulse generator maintains robust TID performance, which is in-line with the presented device level TID-hardness. Finally, the present investigation paves the way for an HBT Gaussian pulse generator as an ideal candidate for use in high-altitude or space-based pulsed radar transceivers.

CHAPTER II

MILLIMETER-WAVE PHASED ARRAY RADAR

2.1. Compact, Low-Power, Single-Ended and Differential SiGe W-Band LNAs with 4.2 dB SE NF at 94 GHz

2.1.1. Introduction

Development of millimeter wave front-ends on silicon has attracted an increased amount of attention, with emerging advanced applications including high data rate communications at 60 GHz, automotive collision avoidance radar at 77-79 GHz, and imaging for medical, security, and remote sensing applications at 94 GHz [57]-[60] (Fig. 27). High resolution active and passive imaging radars, which are used for the detection of moving targets, automatic landing systems, aerial surveillance, and astronomical/geological science operate under various adverse weather and low-visibility conditions, and must meet stringent specifications on linearity and dynamic range, while dissipating low amounts of power. A front-end block diagram for such a potential CW radar transceiver is depicted in Fig. 28. In such a front-end, the LNA could have either a Diff or SE configuration, with the Diff option offering packaging benefits for the transceiver at the cost of increased size and power consumption.

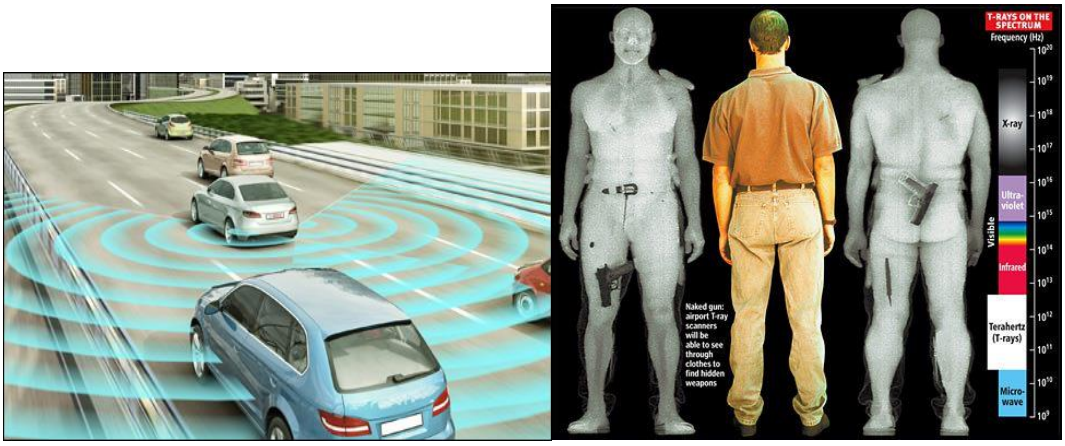

Fig. 27. Millimeter wave radar applications in automotive radar and security imaging.

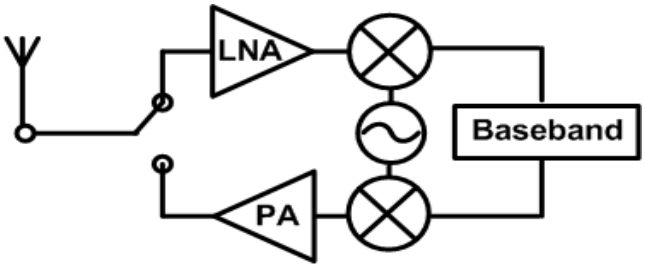

Fig. 28. CW radar transceiver front-end.

Silicon-germanium (SiGe) technology is an attractive candidate to satisfy both high-performance and low cost constraints. SiGe heterojunction bipolar transistors (HBTs) offer a dramatically higher performance compared to conventional Si bipolar junction transistors (BJTs) as a result of bandgap engineering, while maintaining compatibility with low-cost CMOS baseband implementations [19]. In addition, the built-in total dose radiation tolerance of SiGe HBTs makes this technology an ideal candidate for high-altitude and space-based radar systems [52]. The proposed LNAs are implemented in the new IBM 9HP 90-nm SiGe BiCMOS process with SiGe HBTs having f_T/f_{max} of 300/350 GHz, and a 10-layer metal backend suitable for the construction of W-band low-loss transmission lines.

2.1.2. W-Band LNA Design

The schematic of the proposed SE LNA is depicted in Fig. 29, and consists of a single-stage cascode amplifier. For brevity, the Diff version is not depicted here, but it consists of two of the SE branches with the only modification being a change in the value of TL_e to 25 µm. In addition, the Diff version integrates a transformer balun at its input to provide an overall SE-input-to-Diff-output LNA. For biasing purposes, large resistors are used to connect the bias nodes to current mirrors. The reactances for the matching networks are implemented as microstrip lines using the 2nd from the top metal layer as signal and 6th metal layer as ground. In order to minimize the length of the microstrip

lines, a characteristic impedance (Z_0) of 70 Ω was selected, resulting in a line width of 3.5 µm. Furthermore, in order to achieve a compact layout the microstrip lines are meandered. All passive components and interconnects have been extensively EM-simulated in Sonnet. Power and noise matching were accomplished using the guidelines described in [19], resulting in a device emitter length (L_E) of 5.8 µm, and a collector current (I_C) of 4 mA. The matching network components are as listed in Fig. 29.

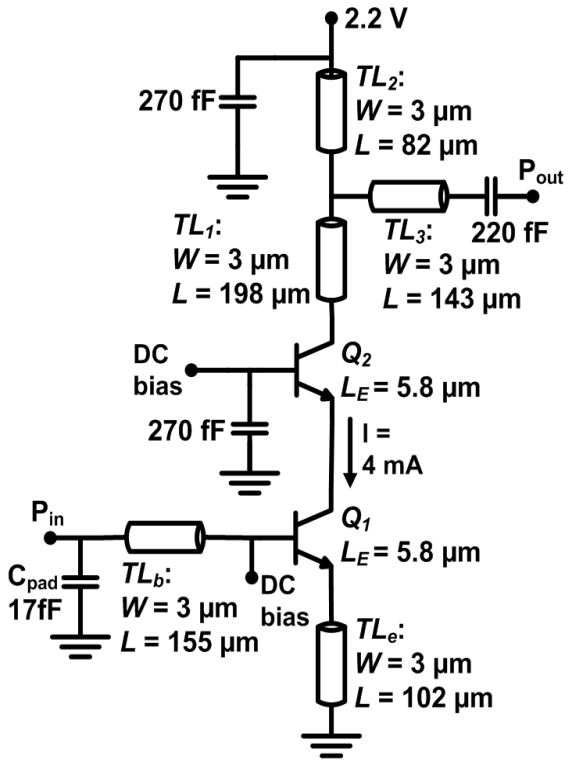

Fig. 29. **SE LNA schematic.**

For the Diff LNA, a passive one-turn, transformer-based 94 GHz balun (Fig. 30(a)) was designed with staggering of the primary and secondary turns (primary and secondary coils are offset parallel to the substrate) to reduce capacitive coupling and maximize magnetic coupling. It should be noted that although a multiple-turn transformer balun can increase the mutual coupling, it degrades the self-resonance frequency. Based on 3-D EM simulations preformed in HFSS and displayed in Fig. 30(b), a staggering

value of 2 µm provides the minimum insertion loss of 4.5 dB (which accounts for the 3 dB loss as a result of power division, as well as 1.5 dB resulting from the balun loss) around 94 GHz, which in turn helps with optimizing the phase-imbalance. The balun was integrated into the input of the Diff LNA using optimized transmission lines for matching and gain, and the differential input feed lines were spaced apart 12 µm on the balun side and 200 µm on the LNA side. An asymmetric balun integration technique is utilized in the interest of better input matching, at the cost of 1 dB loss in Diff gain.

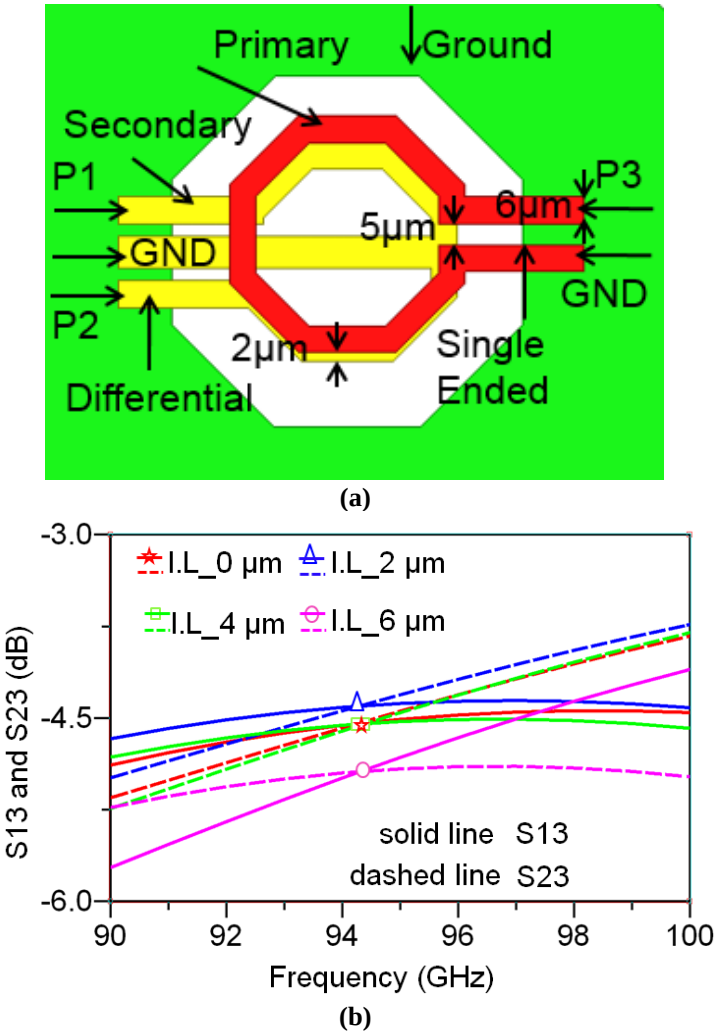

Fig. 30. (a) 3D HFSS model of the transformer-based balun. (b) Simulated insertion loss of transformer-based balun with different staggering/offset values between the primary and secondary coils.

2.1.3. Measurement Results

The W-band low-power SE and Diff LNAs were implemented in an advanced 90-nm SiGe BiCMOS technology having SiGe HBTs with f_T/f_{max} of 300/350 GHz. Die micrograph of the LNAs can be seen in Fig. 31 and Fig. 32 and have a compact core size of only 158 µm × 350 µm (0.055 mm^2) and 288 µm × 430 µm (0.126 mm^2) for the SE and Diff LNA, respectively. The LNAs were measured on-wafer and consume 8.8 mW SE from a 2.2 V supply.

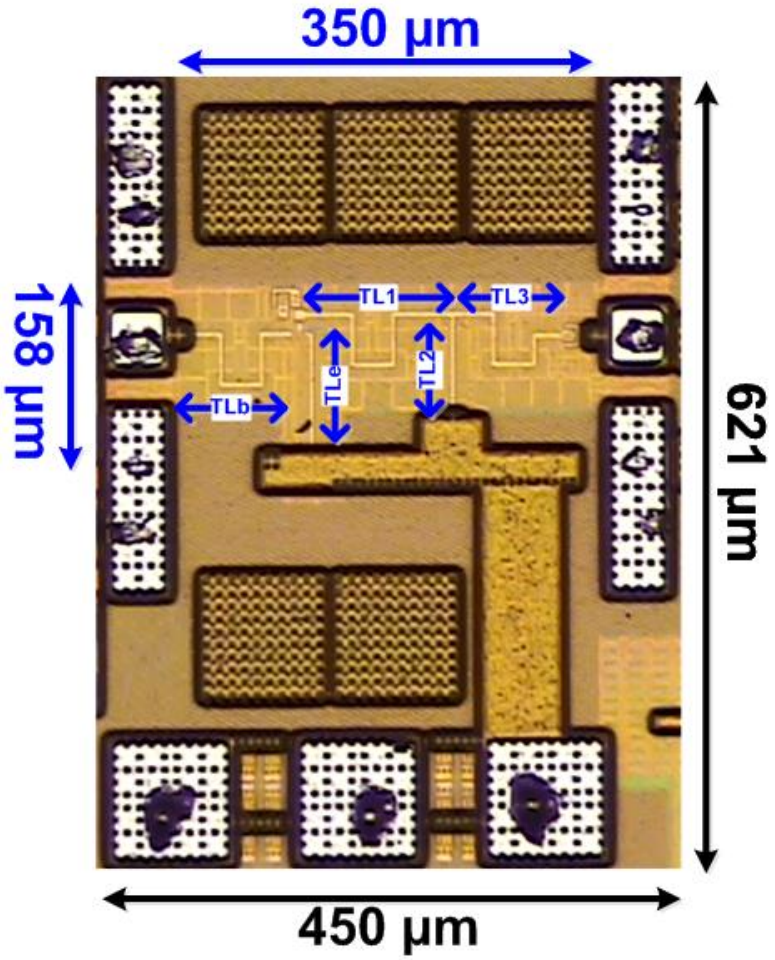

Fig. 31. Die micrograph of SE LNA.

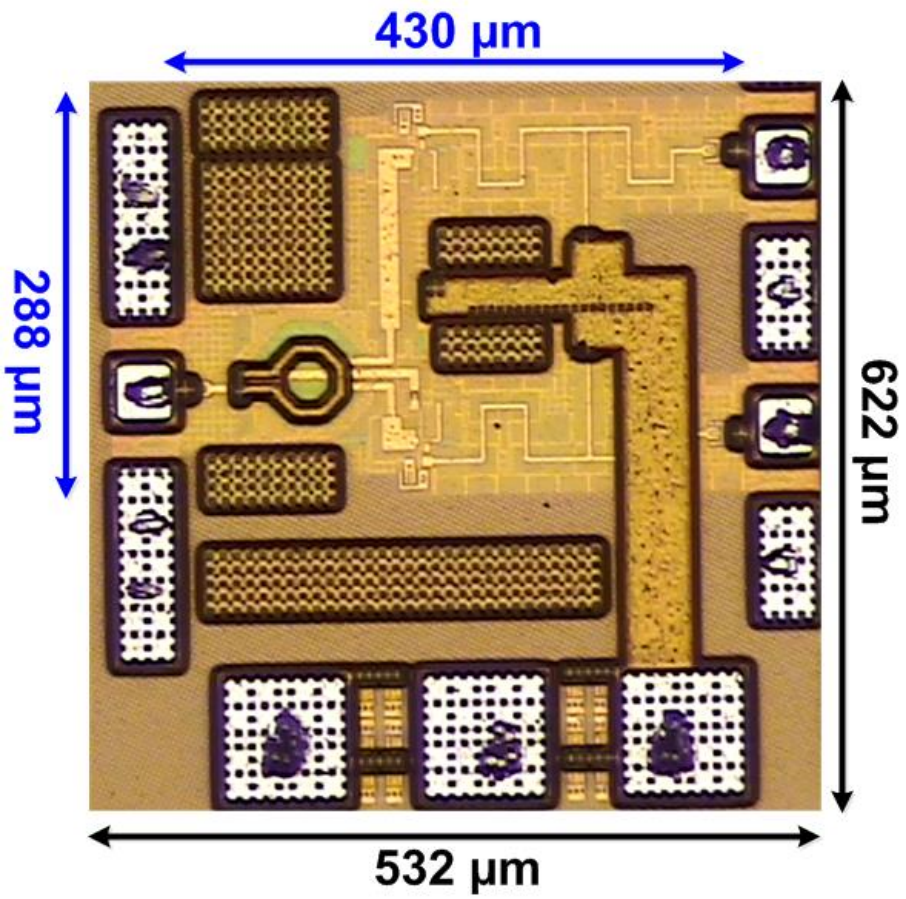

Fig. 32. Die micrograph of Diff LNA with integrated transformer balun.

Fig. 33(a) displays the measured and simulated gain (S_{21}) and *NF* of the SE LNA. It can be seen that a measured S_{21} of 10 dB is achieved at 94 GHz, with the gain shifting slightly to a peak of 10.5 dB at 91 GHz. In addition, S_{21} has less than 3 dB variation across 81 GHz to 101 GHz, resulting in a 20 GHz bandwidth, consistent with the simulated results. The *NF* is measured to be 4.2 dB at 94 GHz, while *NF* remains below 5.0 dB across the operating bandwidth. It should be noted that close agreement between *NF* and NF_{min} are as a result of accurate noise matching and detailed EM-modeling of the input matching network components. The measured and simulated input and output reflection coefficients (S_{11} and S_{22}) of the SE LNA are shown in Fig. 33(b), with an S_{11} of -12.5 dB and S_{22} of -6.5 dB at 94 GHz.

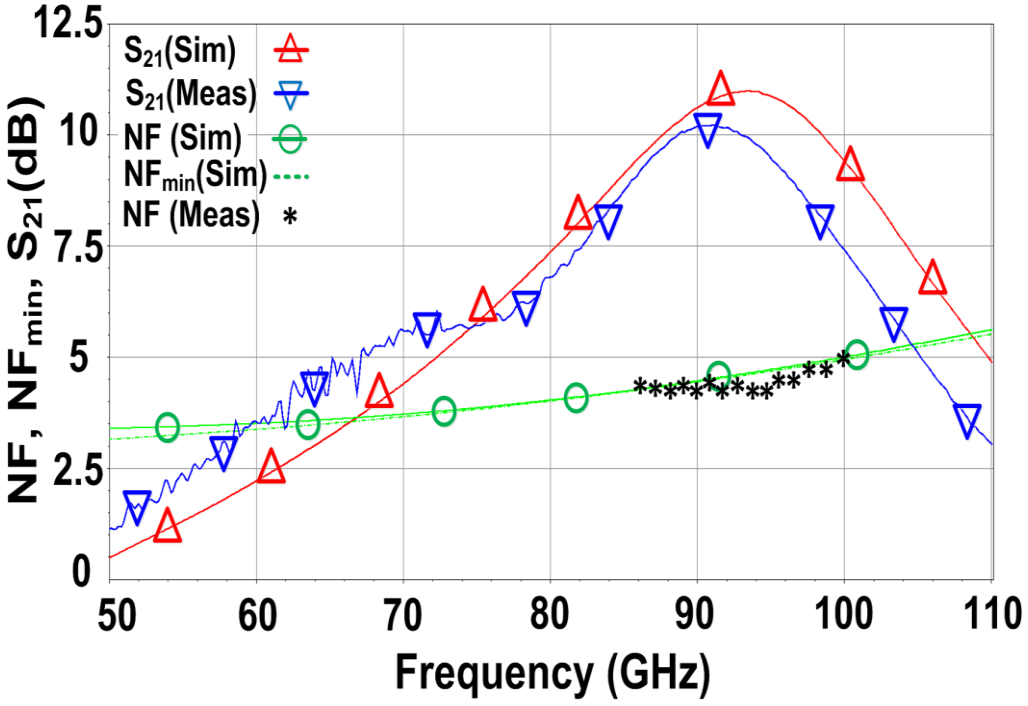

(a)

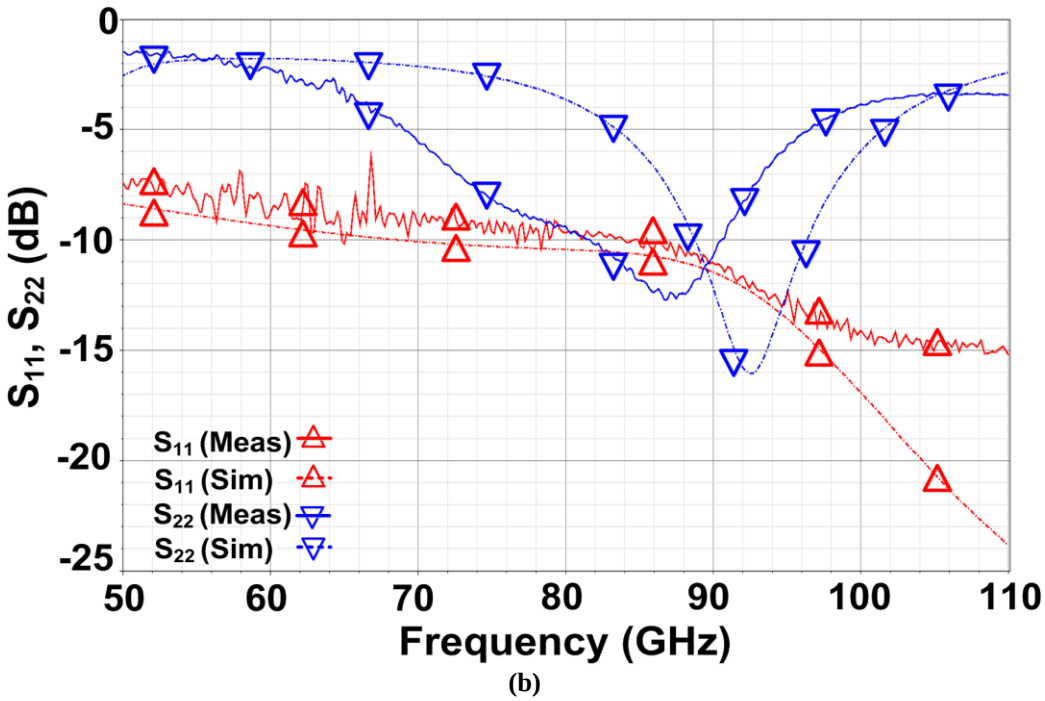

(b)

Fig. 33. Measurement and simulation results for the low-power 94 GHz SE LNA.

Fig. 34(a) displays the measured and simulated gain (S_{21}) and *NF* of the Diff LNA. Since a differential measurement setup was not available, each differential output was measured in a single-ended fashion while the other output remained at an open termination. It can be seen that a differential gain, which is assumed to be the algebraic sum of the two SE gains, of ~ 12 dB is achieved at 94 GHz, with the gain peaking at 90 GHz. In addition, S_{21} has a -3 dB bandwidth of 28 GHz across 76 GHz – 104 GHz. The difference in the simulated and measured S_{21} is a result of non-ideal conditions for the differential gain measurement. Ideally, an output balun should be used just for measurement purposes, followed by de-embedding of that balun, or in a SE measurement the output that is not being measured should be terminated at 50 Ω while the other is being measured in a SE fashion. The *NF* is measured to 6.3 dB at 94 GHz, while it remains below 7.5 dB up to 100 GHz. It should be noted that the difference in *NF* and NF_{min} is a result of an intentional trade-off for input power matching in the process of integrating the balun into the LNA input. The measured and simulated input and output reflection coefficient (S_{11} and S_{22}) of the Diff LNA are shown in Fig. 34(b), with an S_{11} of -18 dB and S_{22} of -5 dB at 94 GHz.

Fig. 35(a) and 35(b) show power measurement results carried out in a one-tone method at 94 GHz for the SE and Diff LNAs, respectively. It can be seen that the SE LNA achieves an input/output P_{1dB} of -11.5/-2.5 and the Differential LNA achieves an input/output P_{1dB} of -8.75/+0.25, while consuming 4 mA from a 2.2 V supply.

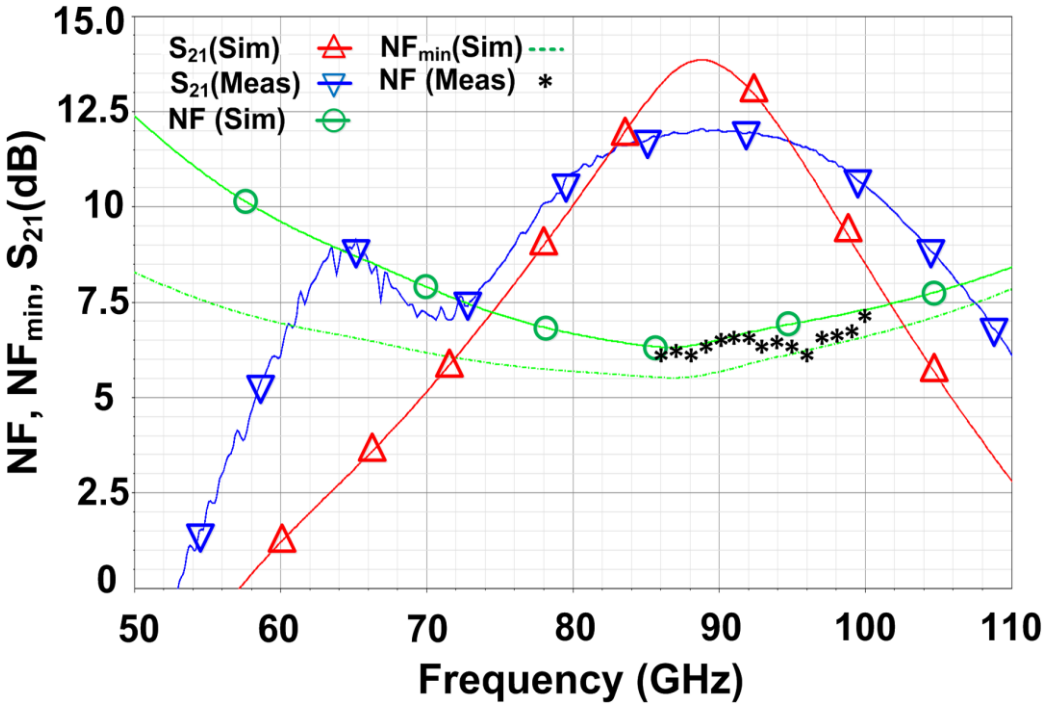

(a)

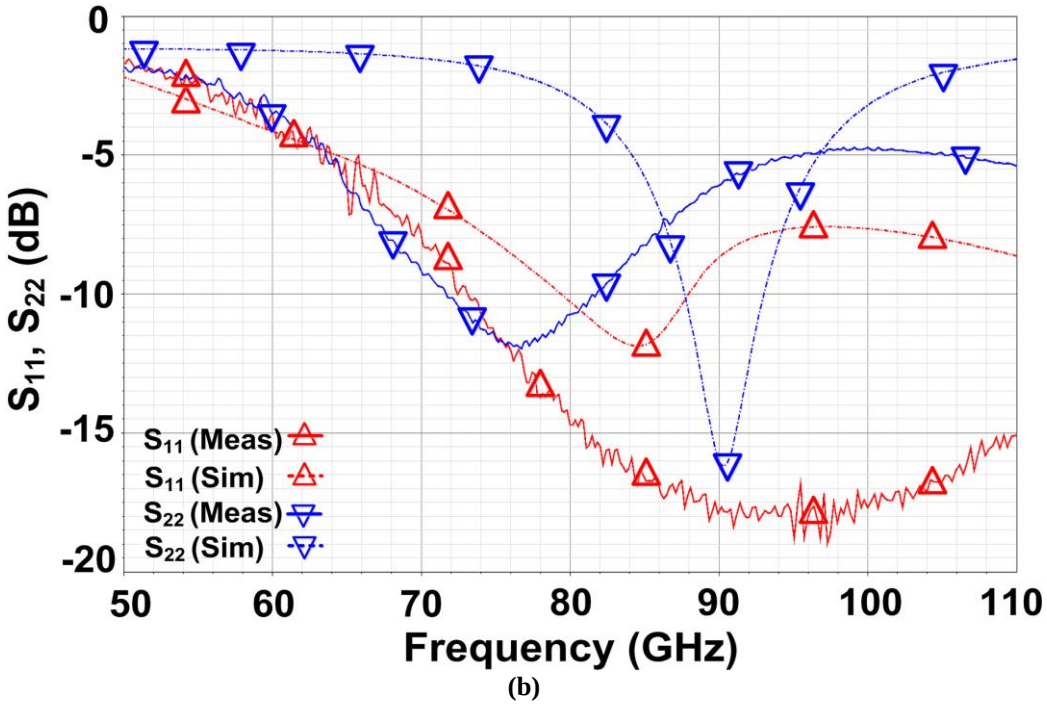

(b)

Fig. 34. Measurement and simulation results for the low-power 94 GHz Diff LNA.

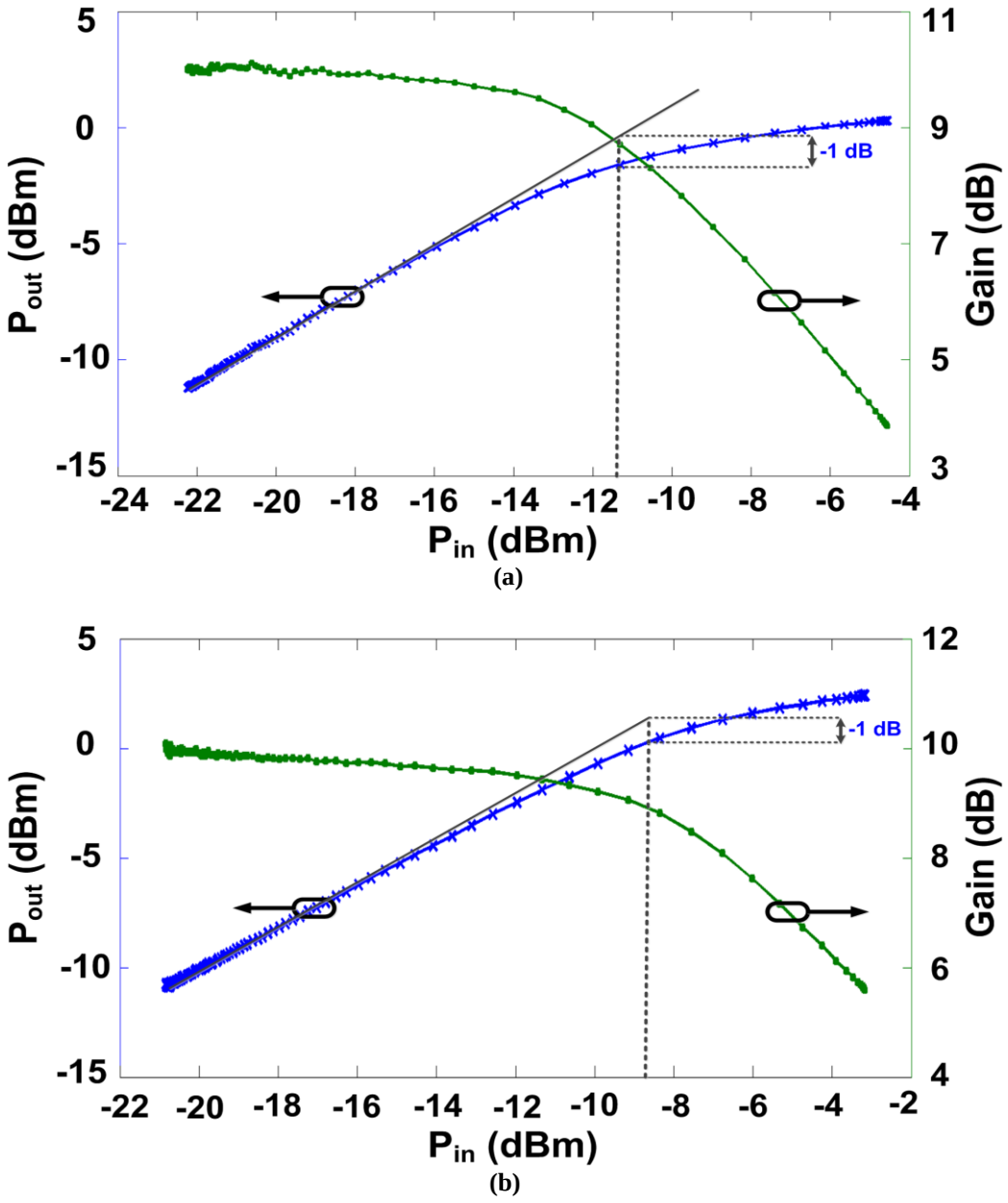

Fig. 35. Power measurement results at 94GHz for (a) SE LNA, and (b) Diff LNA.

Table 2 summarizes the low-power SE W-band LNA's performance and its comparison against eight other state-of-the-art Si-based W-band LNAs. It can be seen that the measured *NF* of 4.2 dB at 94 GHz is the lowest reported NF for W-band LNAs implemented in a technology with f_T/f_{max} of less than or equal to 300/350 GHz. In addition, this performance is achieved while consuming only 8.8 mW, which to the authors' best knowledge is the lowest power consumption for a Si-based W-band LNA.

Table 2
PERFORMANCE SUMMARY AND COMPARISON of PUBLISHED SI-BASED W-BAND LNAs

Ref	***Topology***	f_c ***(GHz)***	S_{21} ***(dB)***	***NF (dB)***	***Power (mW)***	***Tech***
[61]	2-stage Cascode	90	22	7.0	56	130-nm SiGe
[62]	1-stage Cascode	95	9	8.6	13	130-nm SiGe
[63]	1-stage Cascode	95	11	6.0	52	45-nm CMOS
[64]	3-stage CS	90	27	6.8	36	65-nm CMOS
[65]	5-stage CE	95	23	8.0	28	120-nm SiGe
[66]	4-stage Cascode	105	39	6.5	34	180-nm SiGe
[67]	4-stage CE	90	19	5.1	43	90-nm SiGe
[68]*	2-stage Cascode	110	21	4.0	17	130-nm SiGe
This work	**1-stage Cascode**	**94**	**10**	**4.2**	**8.8**	**90-nm SiGe**

*f_T/f_{max} = 300/500 GHz. (All other table references are ≤ 300/350 GHz)

2.1.4. Summary

Two Diff and SE compact linear low-power W-band LNAs are implemented in a 90-nm SiGe BiCMOS technology for 94 GHz active imaging radar applications. The single-stage cascode LNAs demonstrate a measured gain of 10 and 12 dB, with a NF of 4.2 dB and 6.3 dB, for SE and Diff LNAs, respectively, while consuming only 8.8 mW SE power from a 2.2 V supply. The two LNAs have a compact core size of 0.055 mm^2 and 0.126 mm^2 for the SE and Diff LNA, respectively, with a transformer balun integrated at the input of the Diff LNA.

CHAPTER III

IMPLANTABLE MEDICAL DEVICES

3.1. Introduction

Transcutaneous data telemetry is one of the more important functions in a group of implantable medical devices (IMDs) known as neuroprostheses. Such neuroprostheses act as substitute for sensory or motor modalities that are lost due to an injury or a disease [69]. Well-known examples of the prostheses are cochlear implants and visual prostheses that need a large volume of data from external artificial sensors to the IMD. Another example is invasive brain-computer interfaces (iBCI) that collect a massive amount of data from the central neural system (CNS) and transfer the data across the skin to the outside of the body to control the patient's environment or prosthetic limbs after signal processing [70]-[78].

The challenges involved in designing transcutaneous data links relate to the extremely limited space and power available to the IMD for establishing a wideband and robust connection. Because of the significant electromagnetic-field-absorption in the tissue, which exponentially increases with the carrier frequency, high bandwidth must be achieved at the lowest possible carrier frequencies [79], [80]. This requirement rules out the majority of commercially available wideband wireless protocols, such as Bluetooth or WiFi, which operate well in the air at 2.4 GHz. On the other hand, there are specific standards, such as Medical Implant Communication Service (MICS), operating in the 402~405 MHz band, which can only offer a limited bandwidth (300 kHz) [81]. Therefore, there is a need for low-power, robust, and wideband wireless links with novel modulation techniques that are specifically tailored for high-performance IMD applications.

Near-field inductive coupling (Fig. 36) is the most common method that has been utilized for establishing wideband data telemetry links with IMDs. In these links, robustness can be measured by bit error rate (BER) in presence of various sources of external interference, supply ripple, load changes, digital switching noise, and coupling

variations as a result of mechanical vibrations and coils misalignments [80]. It should be noted that similar applications of the near-field data transmission can be found in radio-frequency identification (RFID), contactless smartcards, and high throughput wireless sensors, where batteries are avoided because of their extreme size, cost, and lifetime

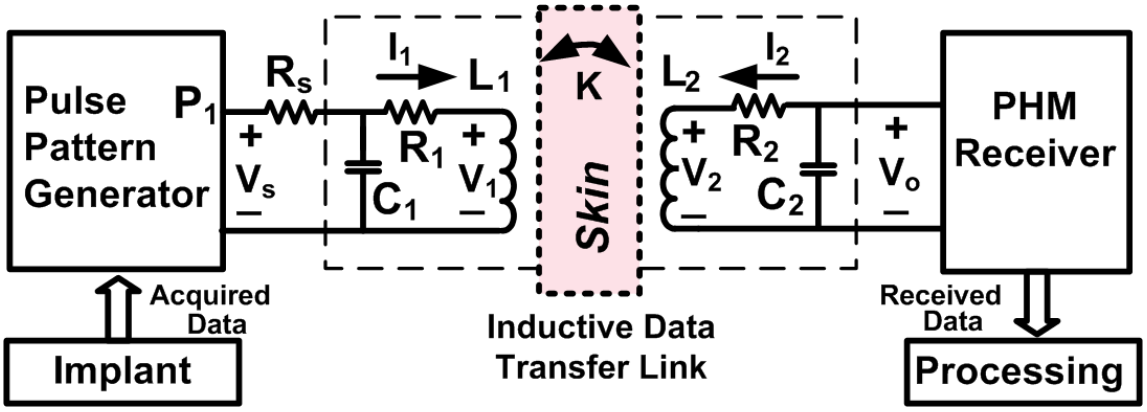

Fig. 36. Near-field data transmission using pulse harmonic modulation (PHM).

constraints [82], [83].

The majority of data transmission techniques for such near-field applications have been carrier based. Amplitude shift keying (ASK) has been popular in the past because of its simple modulation and demodulation circuitry [84]. This method, however, is not robust against coupling variations and faces major limitations in high bandwidth data transmission, which needs high order filters with sharp cut-off that cannot be easily integrated in this low-frequency end of the RF applications. Ghovanloo and Najafi developed a demodulator based on phase-coherent frequency shift keying (pcFSK) and shaped the inductive link passband spectrum to reach 2.5 Mbps [84]. However, that method occupies a wide bandwidth (>5 MHz). A few groups have developed circuits based on binary and quadrature phase shift keying (BPSK, QPSK) [85]-[90], which have fewer limitations compared to ASK and FSK. However, the dependence of all these methods on carrier signals result in high power consumption particularly on the transmitter side. Thus, it is concluded that carrier based techniques are more appropriate

for data transfer from outside of the body, where size and power are less constrained, to the IMD (often referred to as the downlink). In addition it is important to note that use of carrier signals was attractive in the early IMDs because the same low frequency data carrier could be used for transferring power to the IMD. However, the power carrier has to be separated from data carrier in the high performance IMDs, in which much wider bandwidth is required for data while the power carrier frequency cannot be increased because of excessive loss in the tissue at higher frequencies [91]. On the other hand, the use of high frequency data carriers for robust wideband communication with IMDs requires complex and high power consuming frequency stabilization RF circuits, such as phase-locked loops (PLL), which is not desired.

For wideband data transmission from the IMD to the outside of the body (the uplink), most researchers so far have used active back telemetry circuits, such as voltage controlled oscillators (VCO) that utilize similar carrier based modulation techniques in the far-field domain [92], [93]. This is despite the fact that the external receiver antenna can be placed in a patch right across the skin. As a result, the RF transmitter is one of the key power consuming blocks in such IMDs. An alternative method is passive back telemetry using load shift keying (LSK), which is commonly used in the RFID tags for data rates up to 0.5 Mbps [82], [83]. Recently, Mandal et al. improved the LSK bandwidth for iBCI applications [94]. However, LSK, which consists of a switch across the IMD power coil and an ASK receiver outside of the body, requires strong coupling between the coils. Even though a single switch appears to be simple and low power, it entirely shuts off the power transfer to the IMD when it is closed. Hence, a fundamental problem with LSK is reducing the IMD received power by the switching duty cycle, which is not desired in high performance IMDs.

In 2002, the FCC issued a ruling deregulating the use of Ultra-Wide Band (UWB) for low power communications. A variation known as Impulse Radio (IR) UWB, in which data is transmitted via sub-nanosecond pulses through wideband antennas, soon

became quite popular for short range ultra-low power applications such as body area networks (BAN) [95]. Low power consumption in the IR-UWB transmitters is mainly because of being carrier-less, which leads to the elimination of continuously power consuming high frequency oscillators or frequency stabilization circuitry. These features make the IR-UWB an attractive choice for the uplink in IMDs [96]-[98]. However, the caveat is that the ordinary IR-UWB, which is intended for far-field interactions in the 3.1-10.6 GHz band, is highly absorbable in water and cannot penetrate or pass through tissue volume conductor [99].

Several researchers have adopted the idea of a carrier-less wireless link from the IR-UWB and applied it to inductive links in the near field domain by using narrow pulses for transferring data in applications such as chip stacking, multimedia, and BAN [100]-[104]. In all of these efforts, to achieve high data rates, the self resonance frequencies (SRF) of both transmitter (Tx) and receiver (Rx) coils are kept quite large to allow the high frequency components of the narrow data carrying pulses effectively pass through the inductive link, and reconstruct the pulse on the Rx side. It can be shown that when a simple Gaussian pulse with the width of tpw passes through the link, it is differentiated by the inductive coupling between the coils, and its fundamental frequency shifts from DC to $f_P = \sqrt{2}/\pi t_{pw}$ [100]. As a rule of thumb, the inductive link bandwidth should be kept above $2f_P$ to limit the undesired inter-symbol interference (ISI). Otherwise, if the inductive link bandwidth is not sufficiently large, it significantly attenuates the higher harmonic components of the transmitted pulses, which in turn results in ringing on the Rx side that extends well beyond the designated bit period. This will either increase the ISI and BER or lead to data rate reduction.

Maintaining high SFR in the 100's of MHz range for implanted coils that are used in the IMDs is quite challenging because the coils' dimensions, inductance, and separation are often much larger than the on-chip coils used in chip-to-chip communication, while their parasitic resistance is much lower. Due to high conductivity

of the tissue volume conductor, there is also significantly larger parasitic capacitance around the coils that are implanted or attached to the body compared to those operating in the air (BAN) [105]. Therefore, methods proposed in [100]-[104] are not applicable to the IMDs. One possible solution to bandwidth limitation is lowering the coils' quality factor, Q, by adding series or parallel resistors [103], [104]. Of course on-chip coils inevitably have low Qs as a result of their high parasitic resistance [100], [101]. Lower Q, however, decreases the range of the inductive link, i.e. the maximum coil separation, by reducing the amplitude of the received signal, increasing the noise and interference as a result of lowering the receiver selectivity, and consequently degrading the Rx signal to noise ratio (SNR) [102].

This has motivated us to devise a new data transmission technique for near-field wideband applications, called Pulse Harmonic Modulation (PHM), which has similarities to the impulse radio ultra-wideband (IR-UWB) in the far-field domain [106], [107]. The PHM transmitter generates a string of narrow pulses with specific amplitudes and timing to transmit each bit across a pair of high-Q LC-tank circuits. Each pulse generates a decaying oscillatory response at the harmonic frequency that the receiver LC-tank is tuned at, which adds to the oscillations at the same frequency that are resulted from subsequent pulses within that bit period to minimize the inter-symbol interference (ISI) at the receiver input. This allows reaching high data rates without reducing the inductive link quality factor by adding dissipative elements to extend its bandwidth. This method also improves the signal to noise ratio (SNR) at the receiver, leading to improvements in the BER, transmission range, selectivity, and robustness against misalignments of the link.

In the present work a new carrier-less modulation technique, called *Pulse Harmonic Modulation* (PHM), for wideband, low-power, and low-complexity data transmission across inductive-telemetry links that operate in the near-field domain at low frequencies, all of which are necessary to operate in the tissue environment, is introduced.

More importantly, in this method it is neither needed to keep the coils' SRF above $2f_P$ nor is it needed to reduce their Q by adding resistors. On the contrary, both Tx and Rx coils are deliberately tuned at f_P, which is a function of the pulse width (t_{pw}) and maintain their high Q to filter out the undesired sources of interference, such as the strong power carrier [91], increase the inductive link voltage gain, and maximize the SNR at the PHM receiver input.

3.2. Pulse Harmonic Modulation Concept

The goal is to eliminate the carrier signal by using sharp and narrow pulses, similar to the IR-UWB, to significantly reduce the Tx power consumption, while transferring data across an inductive link with low SRF (as a result of parasitic capacitance). The goal was to achieve this without lowering the coils' quality factor, Q, while maintaining a low BER. Therefore, it was needed to deal with the ISI across the

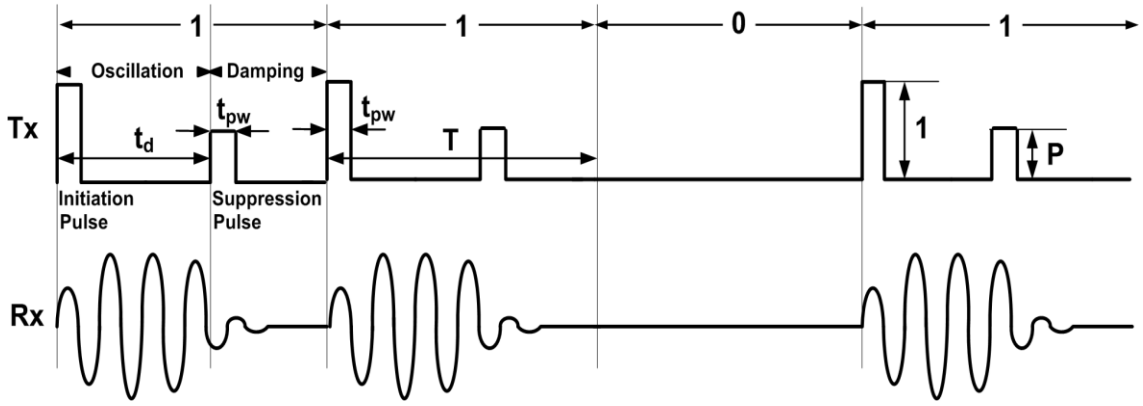

Fig. 37. PHM conceptual waveforms including their key parameters.

secondary Rx coil because of the ringing that follows every pulse. The proposed novel solution is to utilize a pattern of two or more pulses with specific time delays and amplitudes for transferring each bit unlike IR-UWB or other pulse based solutions [95]-[104], in which all pulses are the same. The main idea behind the PHM, which is shown in Fig. 37, is to modulate the key harmonic components of the main pulse, which is called

the *initiation pulse* right at the beginning of each bit, on the Rx side by adjusting the delay time (t_d) and amplitude ratio (P) of one or more additional pulse(s), called *suppression pulse(s)*, that are transmitted within every bit period (T), following the initiation pulse. The resulting signal consists of an oscillation pattern that is amplitude modulated by the successively transmitted pulses to minimize the inter-symbol

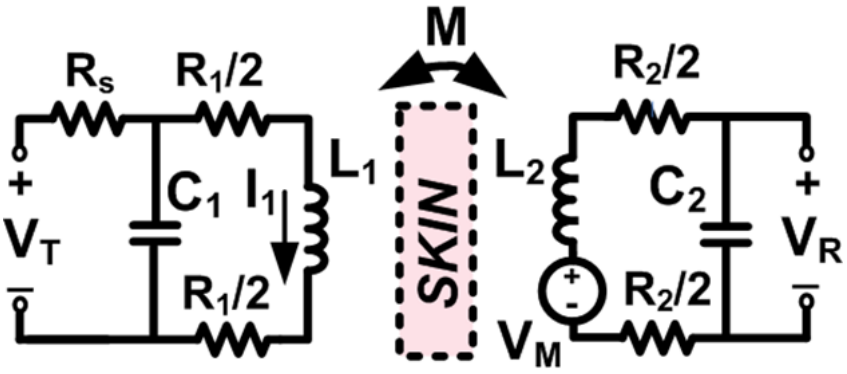

Fig. 38. Lumped model for near-field data telemetry through coupled coils.

interference (ISI) across the Rx coil and facilitate robust data demodulation with low bit-error rate (BER). This is similar to plucking a guitar string once to initiate a tone and then plucking it again at the right time, and with the right amplitude to stop the resonance.

If a narrow pulse is applied across the primary L_1C_1 tank, V_T in Fig. 38, a lowpass filtered version of that pulse passes as current I_1 through R_1 and L_1. The loose mutual coupling, M, between L_1 and L_2, representing a small coupling coefficient, $k = M / \sqrt{L_1 L_2}$, induces a similar but much smaller current, I_2, in L_2, which creates V_R across the Rx input. V_R has an oscillatory nature at a frequency close to the secondary resonance, $f_r = 1/2\pi\sqrt{L_2 C_2}$, and decays exponentially. It can be shown that the amplitude of V_R oscillations (received signal envelope) drops below 4% of its initial value after Q_2 cycles, where Q_2 is the quality factor of the secondary series L_2C_2 tank,

$$Q_2 = \frac{1}{R_2}\sqrt{\frac{L_2}{C_2}}. \qquad (1)$$

In a simple encoding scheme, it can be assumed that the presence or absence of a pulse at the beginning of every bit period (t = 0) represents a data bit "1" or "0", respectively. To minimize ISI, the envelope of V_R oscillations needs to be negligible at t = T. Therefore, to achieve a high data rate, V_R oscillation should cease rapidly, and any residual oscillations beyond T are highly undesired. This is why in all previous carrier-less solutions, a wideband low-Q approach has been adopted [100]-[104]. These methods succeed in achieving high data rates at the expense of degrading the SNR and selectivity of the Rx, which are not acceptable in safe transcutaneous IMD communications.

In the PHM, on the other hand, instead of reducing Q_2, the oscillation pattern of V_R is altered (modulated), which consists of the harmonic components of the initiation pulse by sending one or more narrow pulses within the same bit period to rapidly suppress the oscillation at V_R before T. In Fig. 37 only one suppression pulse with the same width (t_{pw}) is used in every "1" bit. P and t_d for the suppression pulse have been selected such that it creates a decaying oscillatory pattern across V_R that is equal and out of phase compared to that of the initiation pulse from $t = t_d$ to the end of the bit period. P and t_d are dependent on f_r, Q_2, t_{pw}, T, and N, which is the desired number of cycles at the input of the PHM receiver for a reliable, low BER data detection before the oscillation is suppressed. Even though k may change as a result of misalignments or mechanical vibrations between the two coils at a rate much slower than 1/T, since it affects all pulses within a bit period in the same way, the PHM mechanism will not be affected.

3.2.1. Pulse Harmonic Modulation Theory

3.2.1.1. Inductive-link Impulse Response

Fig. 38 shows a lumped equivalent circuit model of an inductive link. The primary (L_1C_1 transmitter) and secondary (L_2C_2 receiver) sides are composed of LC-tank circuits and their associated parasitic components (R_1 and R_2). L_2C_2 tank is tuned at f_r, while the L_1C_1 tank, depending on the data rate and transmission range requirements, can

be either tuned to f_r or left at its self-resonance frequency (SRF), in which case C_1 in Fig. 38 simply represents the parasitic capacitance of L_1. Since L_1 and L_2 are loosely coupled (small k) and the current in L_2C_2 tank is very small, unlike inductive power transmission links, the effect of L_2C_2 loading on the Tx circuitry can safely be neglected to simplify the equations. Hence, the inductive link transfer function in the S-domain can be described as,

$$H(s)=\frac{V_R}{V_T}=\frac{V_R}{V_M}\times\frac{V_M}{I_1}\times\frac{I_1}{V_T}=\frac{MS}{(R_sL_1C_1s^2+(R_sR_1C_1+L_1)s+R_s+R_1)(C_2L_2s^2+C_2R_2s+1)}, \quad (2)$$

where V_T, V_R, I_1, and V_M are the Tx output voltage, Rx input voltage, current passing through L_1, and induced voltage across L_2, respectively. Other parameters are lumped circuit elements in Fig. 38. $H(s)$ is composed of two second-order systems, one originating from the primary and the other from the secondary LC-tanks, each of which can be expressed as,

$$\frac{1}{s^2+2\zeta\omega_n s+\omega_n{}^2}=\frac{1}{(s-s_1)(s-s_2)},\ s_1=-(\zeta\omega_n+j\omega_d),\ s_2=s_1^*,\ 0\le\zeta<1, \quad (3)$$

where ζ is the damping ratio, ω_n is the natural frequency, and $\omega_d=\omega_n\sqrt{1-\zeta^2}$ is the natural damping frequency of the system. From (2) and (3), these 2nd-order system parameters can be expressed in terms of the lumped circuit elements in Fig. 38,

$$\zeta_1\omega_{n_1}=\frac{(R_sR_1C_1+L_1)}{2R_sL_1C_1}\cong\frac{1}{2R_sC_1},\quad \omega_{n_1}{}^2=\frac{R_s+R_1}{R_sL_1C_1}\cong\frac{1}{L_1C_1}, \quad (4)$$

$$\zeta_2\omega_{n_2}=\frac{R_2}{2L_2},\quad \omega_{n_2}{}^2=\frac{1}{L_2C_2} \quad (5)$$

$$\zeta_1=\frac{(R_sR_1C_1+L_1)}{2R_s\sqrt{L_1C_1}}\sqrt{\frac{R_s}{R_s+R_1}}\cong\frac{1}{2R_s}\sqrt{\frac{L_1}{C_1}} \quad (6)$$

$$\zeta_2 = \frac{R_2}{2}\sqrt{\frac{C_2}{L_2}}\,. \tag{7}$$

Assuming both 2nd order systems are under damped, i.e. ζ_1 and $\zeta_2 < 1$, which is often the case for the LC-tanks used in data telemetry links, (2) can be rearranged as,

$$H(s) = \frac{Ms}{R_s L_1 C_1 (s - s_{11})(s - s_{21}) \times L_2 C_2 (s - s_{12})(s - s_{22})}, s_{1j} = -(\zeta_j \omega_{n_j} + j\omega_{d_j}),\ s_{2j} = s_{1j}{}^*, j = 1,2\,. \tag{8}$$

Now $H(s)$ can be broken up into the sum of its first order components,

$$H(s) = \left[\frac{A_1}{(s - s_{11})} + \frac{A_1{}^*}{(s - s_{21})} + \frac{A_2}{(s - s_{12})} + \frac{A_2{}^*}{(s - s_{22})}\right]\ , \tag{9}$$

Where,

$$A_1 = \frac{Ms_{11}}{R_s L_1 C_1 (s_{11} - s_{21}) \times L_2 C_2 (s_{11} - s_{12})(s_{11} - s_{22})} = a_1 + jb_1, \tag{10}$$

$$A_2 = \frac{Ms_{12}}{R_s L_1 C_1 (s_{12} - s_{11})(s_{12} - s_{21}) \times L_2 C_2 (s_{12} - s_{22})} = a_2 + jb_2\,, \tag{11}$$

and apply the inverse Laplace transform to find the impulse response for the inductive link,

$$L^{-1}\left[\frac{1}{s - a}\right] = e^{at} \tag{12}$$

$$h(t) = 2e^{-\zeta_1 \omega_{n_1} t}(a_1 \cos(\omega_{d_1} t) + b_1 \sin(\omega_{d_1} t)) + 2e^{-\zeta_2 \omega_{n_2} t}(a_2 \cos(\omega_{d_2} t) + b_2 \sin(\omega_{d_2} t))\,. \tag{13}$$

High-Q is desired for the inductive data transmission links used in IMD applications to improve transmission range and robustness of the link against interference without increasing the transmitted power. Q_1 and Q_2 can be calculated from (6) and (7)

by substituting them in $Q = 1/2\zeta$, which indicates that ζ should be small and thus, $\omega_d \approx \omega_n$. As a result, $h(t)$ in (13) can be simplified into two exponentially decaying oscillations, one with a long time-constant of $\tau_2 = 1/\zeta_2\omega_{n2} = 2L_2/R_2$ on the secondary and the other with a short time-constant of $\tau_1 = 1/\zeta_1\omega_{n1} \approx 2R_sC_1$ on the primary. The sum of these two terms will result in an oscillation across V_R in Fig. 38, which builds up rapidly but decays slowly [106]. The envelope of *h(t)* can be expressed as,

$$h_{env}(t) = 2|A_1|e^{-\zeta_1\omega_{n_1}t} + 2|A_2|e^{-\zeta_2\omega_{n_2}t}. \quad (14)$$

3.2.1.2. Pulse-harmonic Modulation

Using the inductive link impulse response from the previous section, one can calculate V_R for any arbitrary input waveform by convolving it with $h(t)$. However, if only narrow pulses are applied across V_T, with pulse width $t_{pw} \le \sqrt{2}/\pi f_r$ and amplitude α to reduce Tx power consumption, then $\alpha h(t)$ can be expected to appear across V_R [106]. On the other hand, in high speed pulse-based data transmission, it is important for the received signal (i.e. the impulse response), resulted from transmitting a single bit, to rise sharply (small τ_1) to enhance detection and decline rapidly (small τ_2) to minimize ISI with the following bit, and reduce BER. Both of these requirements suggest that Q_1 and Q_2 should be lowered to improve bandwidth, which is the method that has been adopted in previous carrier-less near-field data links [100], [104]. However, this is not a suitable choice for robust transcutaneous communications.

Considering that $h(t)$ has a sharp rise time and a slow decay, in PHM a rapid oscillatory response is generated across V_R by applying a first pulse, called the *initiation pulse*, across V_T at the onset of every digital bit "1" ($\alpha = 1$). Then a second pulse (or pattern of pulses) is (are) transmitted, called the *suppression pulse(s)*, before the end of the bit period, T, to create a second oscillation. The amplitude, P, and delay, t_d, of the

suppression pulse are chosen such that the second oscillation has the same amplitude as the first one by the time that it appears across V_R, but 180° out of phase. The result is the cancellation of both oscillatory responses after the arrival of the suppression pulse, leading to a rapid decline in the ISI, which is the amplitude of the oscillation across V_R by the time that a new bit is due to begin. In this implementation, for a digital bit "0", simply no pulses are transmitted [106].

To minimize BER, we should first allow the oscillation resulted from the initiation pulse to build up. According to (14), this can take ~$4\tau_1$. Hence, to reduce the buildup time, according to (6), C_1 and R_s should be as small as possible. In fact the parasitic capacitance of L_1 is often sufficient to form C_1. Then the suppression pulse should be applied at an odd multiple of a half cycle ($1/2f_r$) to ensure that the two responses are going to be out of phase,

$$t_d = (N + \frac{1}{2}) \times \frac{1}{f_r} \qquad 4\tau_1 f_r \le N < T f_r \tag{15}$$

where N is the number of cycles that $h(t)$ is allowed to have before it is suppressed.

For a perfect cancelation, when choosing the suppression pulse amplitude, P, the decay of $h(t)$ from the initiation pulse at $t = t_d$ should be considered. The amplitude of $h(t_d)$ can be found from its envelope in (14). Since $t_d >> \tau_1$, the first term, which represents the buildup period, can be neglected and the ratio between the suppression and initiation pulses can be found from,

$$P = e^{-t_d / \tau_2}. \tag{16}$$

Using (3)-(16), t_d and P can be easily calculated from the inductive link lumped circuit values and other parameters, such as the desired data rate ($DR = 1/T$) and pulse width (t_{pw}), to design a PHM-based near-field data telemetry link.

In practice, perfect cancellation between initiation and suppression pulses is not possible due to timing jitter, parasitic components, and process variations [106]. Nonetheless, as shown, PHM is an effective method for reducing the ISI and achieving wide bandwidth at low BER without lowering the link quality factor or consuming too much power.

3.2.1.3. Pulse-harmonic Modulation Simulations

Fig. 39 shows the results of simulating the PHM concept from the previous section in MATLAB, using measured parameters from the coils utilized in the measurements (Table 3) in the equations derived in previous theory section [105]. Fig. 39(a) shows square shaped initiation and suppression pulses at the output of the PPG block (V_T), each of which is t_{pw} = 12 ns wide. Therefore, the pulse spectral power after differentiation will be centered on f_P = 37.5 MHz, which is close to the resonance frequency that we have chosen for the inductive link (f_r = 33 MHz).

The solid waveform in Fig. 39(b) shows the received signal at the output (V_o), across V_R, if an individual pulse was used for sending each bit, similar to the previous pulse based methods. It can be seen that the large Q_2 = 44.8 has resulted in a slow exponential decay ($\tau_2 = 1/\zeta_2\omega_{n2} = 2L_2/R_2 \approx$ 432 ns) in oscillation at the Rx input, which could either lead to a slow data rate or significant ISI.

To find t_d, the buildup time for oscillation ($\tau_1 = t_b = 1/\zeta_1\omega_{n1} \approx 2R_sC_1$ = 89.6 ns when R_{s1} = 50 Ω), 1/T = 200 ns for a data rate of 5 Mbps, and $1/f_r$ = 30.3 ns were considered. N = 3 was chosen to have 3.5 cycles of oscillation across V_R before the suppression pulse is applied. Therefore, according to (15), t_d = 106 ns. The time response of the suppression pulse at Rx, if it was applied individually, is shown with dashed lines in Fig. 39(b). It can be seen that the oscillations resulted from the two pulses are out of phase and reach the same magnitude around t_0, which depends on the suppression pulse amplitude, P.

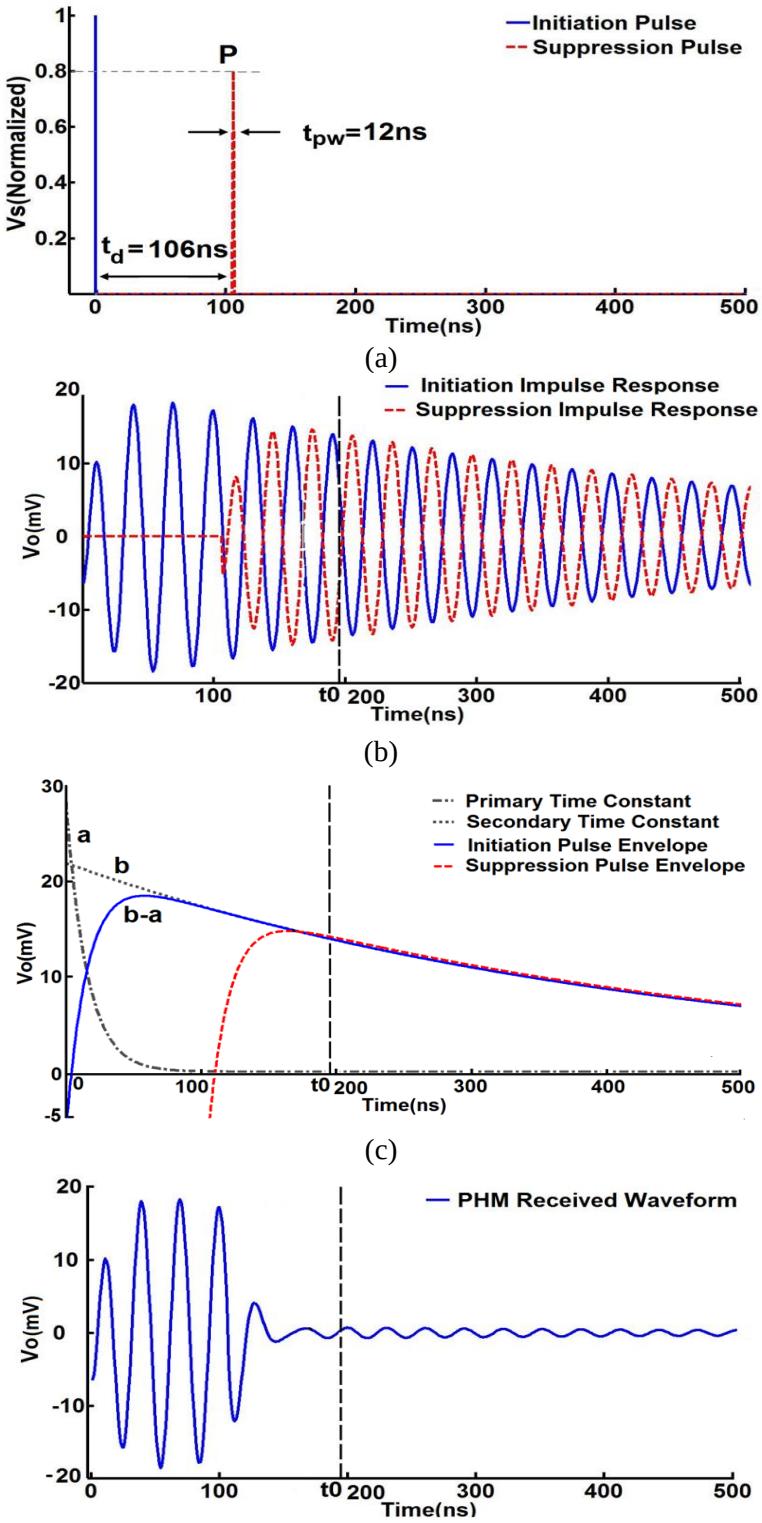

Fig. 39. (a) Initiation and suppression pulses at the output of the Tx (PPG) in Fig. 36. (b) Individual responses to initiation and suppression pulses at the input of the Rx. (c) Envelopes of the initiation and suppression pulses, showing the build up and decay phases, which begin cancellation at $t = t_0$. (d) Received PHM signal across the Rx input, which is amplitude modulated by the suppression pulse to reduce the ISI.

TABLE 3
FIGURE-8 COILS SPECIFICATIONS

Coil	Size (cm)	L (nH)	R (mΩ)
L_1	1 × 1	105	412
L_2	1.9 × 1.9	281	1300
Coil	C_p (pF)	C_t (pF)**	SRF (MHz)
L_1	2.1	225	338
L_2	3	82.7	173.2

* Number of turns for each coil, n = 2.
** Total capacitance required across the coils to resonate at f_r = 33 MHz.

To find P, (14) was used to specify the envelopes of the received waveforms, as shown in Fig. 39(c). By plugging t_d and other parameters from (4)-(7) in (16), and considering that the primary time constant, is short and the second term in (14) is practically zero for $t > t_b$, $P = 0.8$ was found. Finally, Fig. 39(d) shows the received PHM waveform at V_R when a suppression pulse is transmitted with the designated delay (t_d) and amplitude (P), following the initiation pulse, for every bit "1". It can be seen that the long tail of oscillation, which was extending well beyond 500 ns in Fig. 39(b), has been effectively truncated, and the PHM Rx is ready to detect the following bit at 1/T = 200 ns for a data rate of 5 Mbps with negligible ISI.

Fig. 40 compares the frequency response of the inductive wireless link used in this work with that of [100] and [103] using (2). The higher quality factor of the tuned coils, particularly Q_2, results in higher gain, more SNR, and better selectivity, which can translate to longer range, lower BER, and more robustness against external interference, artifacts, and coil misalignments, which are crucial in safe IMD applications.

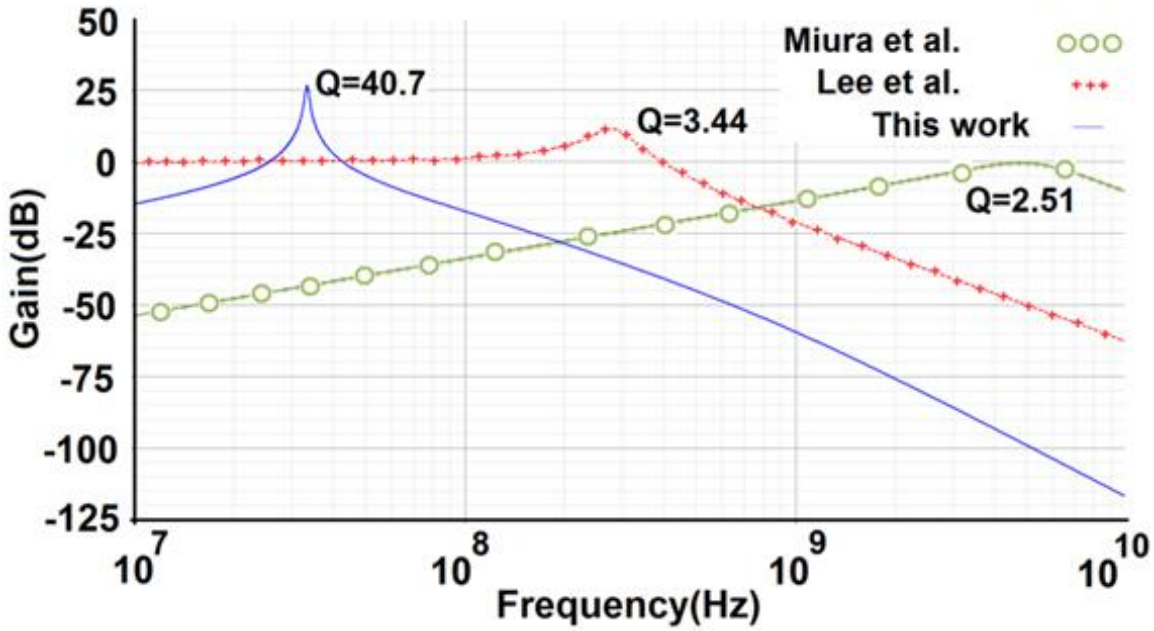

Fig. 40. A comparison between the frequency response of the inductive links used in this work, [100], and [103]. The higher quality factor of the tuned coil on the receiver (Q_2) result in higher gain, more SNR, and better selectivity, which can lead to longer range and more robustness against interference and coil misalignments, which are crucial in IMD applications.

3.3. PHM Proof-of-concept Discrete-circuit Implementation and Link Performance Demonstration

To demonstrate the PHM concept in an actual inductive wireless link, a proof-of-concept prototype has been developed using discrete circuits on both Tx and Rx sides. This setup clearly demonstrates the functionality of the PHM concept and validates the theoretical foundation, which was laid out in the previous sections. However, more accurate measurements and ratings will require implementation of the transceiver in an application specific integrated circuit (ASIC).

3.3.1. PHM Transmitter

Fig. 41 shows the schematic for the PPG block, which was implemented using an Altera Cyclone II field programmable gate array (FPGA) [108]. Since pulses are only generated for "1" data bits, $\overline{Data}+Clk$ was used as the input. Two programmable delay

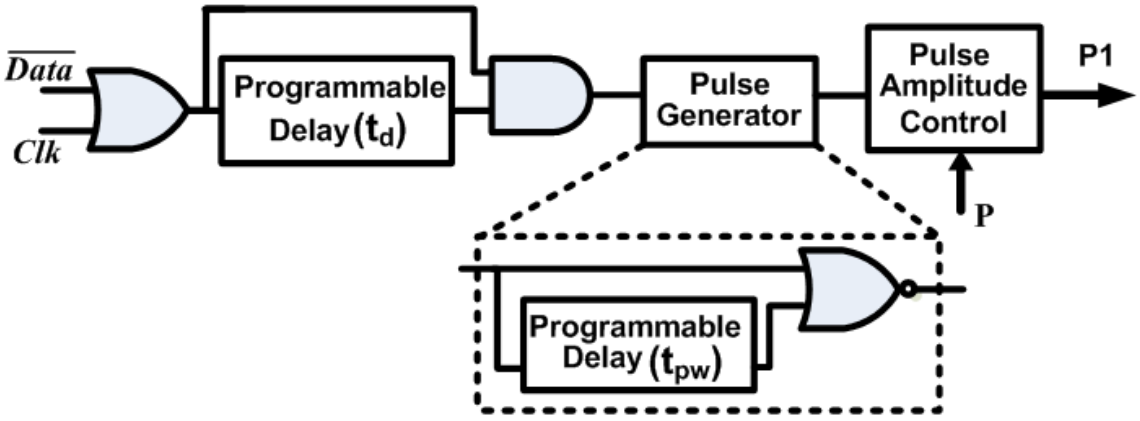

Fig. 41. Block diagram of the pulse pattern generator (PPG) on the Tx side.

elements were used to allow us control the width (t_{pw}) and time delay (t_d) of the PHM pulses. These delay elements were programmable via the Quartus-II software [109]. The pulse generator block simply combines the input with its delayed version to produce a sharp pulse. The pulse amplitude control block was implemented using a simple ladder network circuit to adjust *P*. Alternatively, a high speed digital to analog converter (DAC) could be used for this purpose. The initial t_d and *P* values were selected as a starting point, derived from theoretical calculations and simulations in the previous sections and made minor manual adjustments to compensate for the parasitic components that were not accounted for in the models.

3.3.2. Coils and Tuning Capacitors

To construct the wireless inductive data transmission link (L_1 and L_2 in Figs. 36 and 38) Figure-8 coils on FR4 PCB substrate were used. Fig. 42 shows the 3-D model of one of these coils in the HFSS field solver (Ansoft, Pittsburgh, PA). A detailed description of these coils, their optimal geometrical design methodology, and variations in *k* as a result of coil misalignments have been described in [105], and will not be repeated here. However, the main reason for choosing this coil geometry in the present IMD application is its resilience against external magnetic field interference, which is key

in a multiband transcutaneous inductive wireless link [80]. When a Figure-8 coil is exposed to uniform or symmetrical external magnetic field, the currents induced in the two loops of each coil are canceled out due to their opposing direction of winding, while the two data coils maintain a decent coupling. Table 3 summarizes the measured specifications of the coils used in the present experiments. Coil geometries were designed for an uplink with nominal coil separation of d = 10 mm. L_1 is smaller to be embedded within the IMD, while L_2 will be located across the skin outside of the body. When the two coils are perfectly aligned, they have a simulated k = 0.012 [105]. C_p is the parasitic capacitance of each coil in the air, leading to its SRF, and C_t is the total capacitance

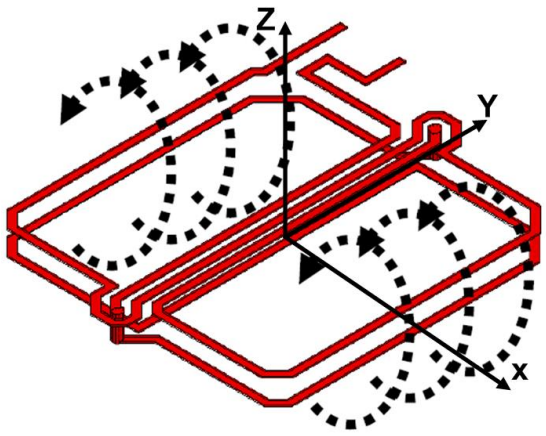

Fig. 42. 3-D model of Figure-8 coil in HFSS field solver. [105]

needed in parallel with each coil (including C_p) to tune it at f_r = 33 MHz.

3.3.3. PHM Receiver

A simplified block diagram of the PHM receiver is shown in Fig. 43. In essence, this is a simple custom designed envelope detector, consisting of a low noise amplifier (LNA) with a gain of 26 dB, followed by a rectifier and low pass filter (LPF) with 9 MHz cutoff. A high speed comparator compares the LPF output, which is the envelope of the PHM signal, shown in Fig. 39(d), with a reference voltage to sharpen the received pulses and converts them to logic levels. A second Cyclone II® FPGA board oversamples the

received pulses at 48 MHz and converts them to a serial data stream. A more detailed description of this receiver can be found in [110].

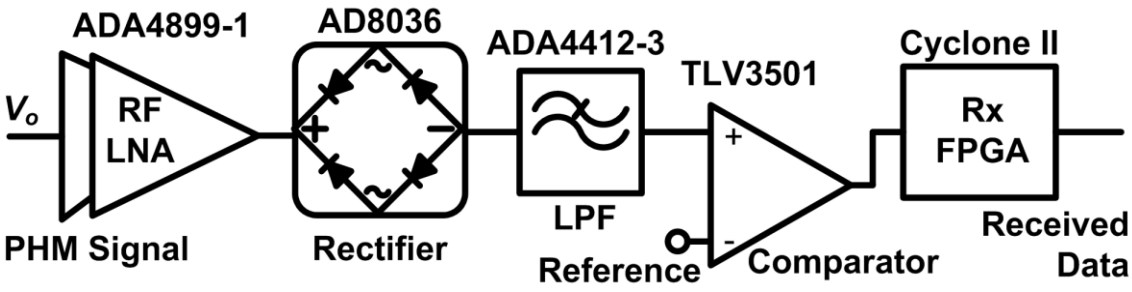

Fig. 43. Block diagram of the PHM receiver (Rx). [110]

3.3.4. Measurement Results

In addition to the blocks described above, the PHM measurement setup included a pair of Tektronix GB1400 (GigaBERT) on the Tx and Rx ends, before and after the two FPGA boards, for high speed data bit steam generation and BER analysis, respectively (see Fig. 44). Fig. 45 shows the measured waveforms across V_T at the PPG output and V_R at the PHM receiver input, which are in close agreement with the presented theoretical analysis and simulated waveforms in Fig. 39. A 2 V pulse with t_{pw} = 15 ns (1.2 nJ/pulse in simulation) resulted in a 75 $mV_{p\text{-}p}$ oscillation across input of the Rx (V_o or V_R). Figs. 45(a) and 45(b) show the initiation and suppression pulses, respectively, when they are transmitted individually.

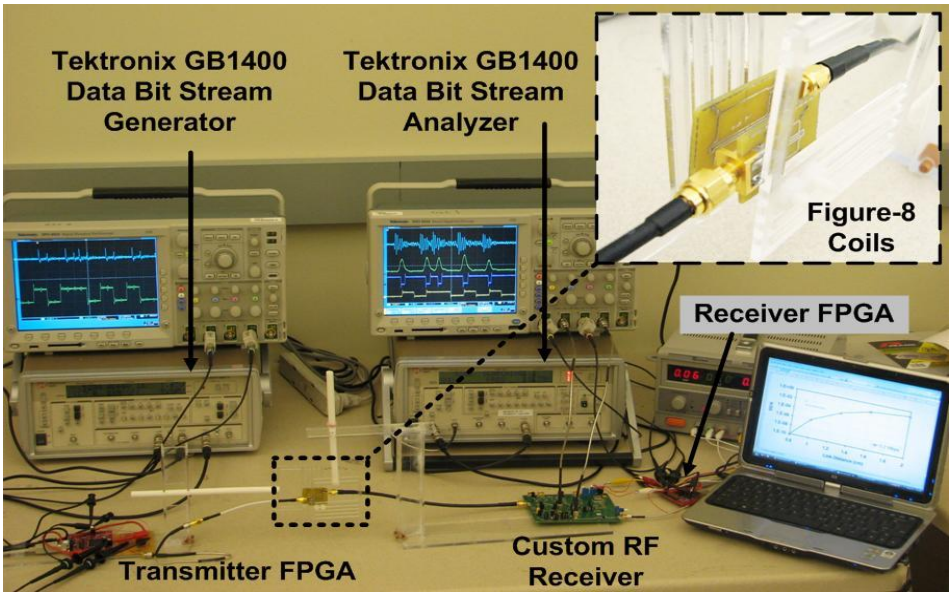

Fig. 44. PHM measurement setup. Inset: Figure-8 coils implemented on FR-4 PCB as described in [105].

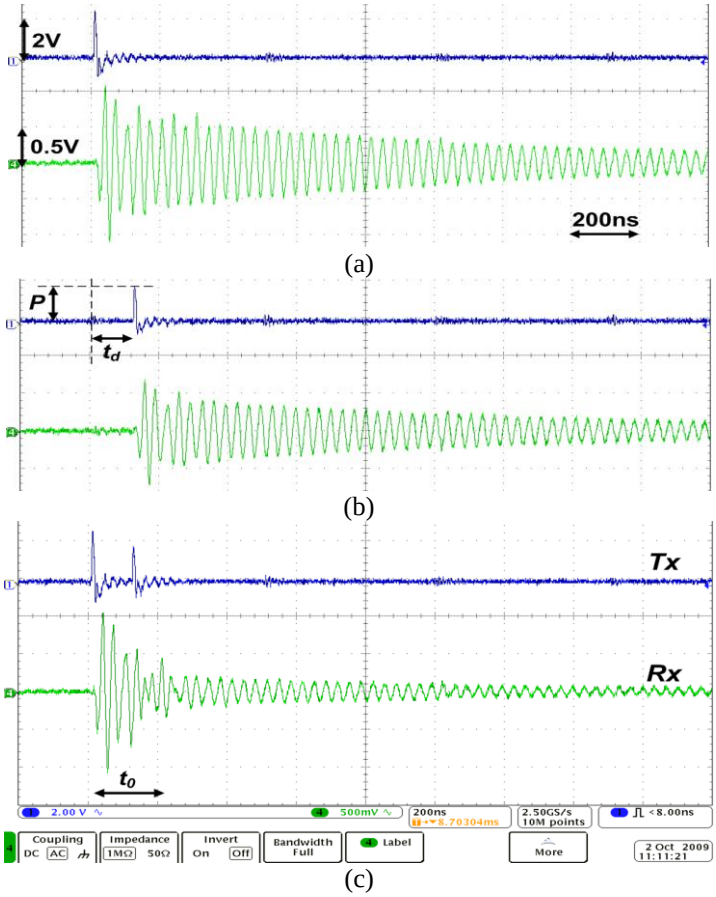

Fig. 45. Measured waveforms across V_T (Tx) and V_R (after amplification by the RF LNA) in Fig. 43, showing the (a) initiation and (b) suppression pulses when transmitted individually. (c) PHM waveforms for a single bit "1" at Tx and Rx, showing significantly reduced ISI.

It can be seen that high Q_2 has resulted in a slow decay of V_R oscillations at 33 MHz, which can lead to significant ISI or low data rates. In Fig. 45(c), however, PHM is applied by transmitting two pulses for each bit "1" with *td* = 118 ns and *P* = 0.77, which are close to the values calculated in through (15) and (16). The result is significant reduction in the ISI, allowing data rates in excess of 5 Mbps in this particular implementation, which is more than one order of magnitude higher than the data rate that could be achieved without the PHM.

To better quantify the bandwidth of the PHM based inductive data transmission link, the GB1400 was used on the Tx to generate a random serial data bit stream, and the received serial data was fed to the GB1400 on the Rx. Once the two GigaBERTs are synchronized, they can measure the BER in real time. Fig. 46 shows a snapshot of the key measured waveforms in the PHM setup in Fig. 46 when data rate was set at 5.2 Mbps and the Figure-8 coils were aligned at *d* = 1 cm. These waveforms clearly show the effect of the PHM suppression pulses in facilitating the detection of the bits following "1s" by effectively reducing the ISI.

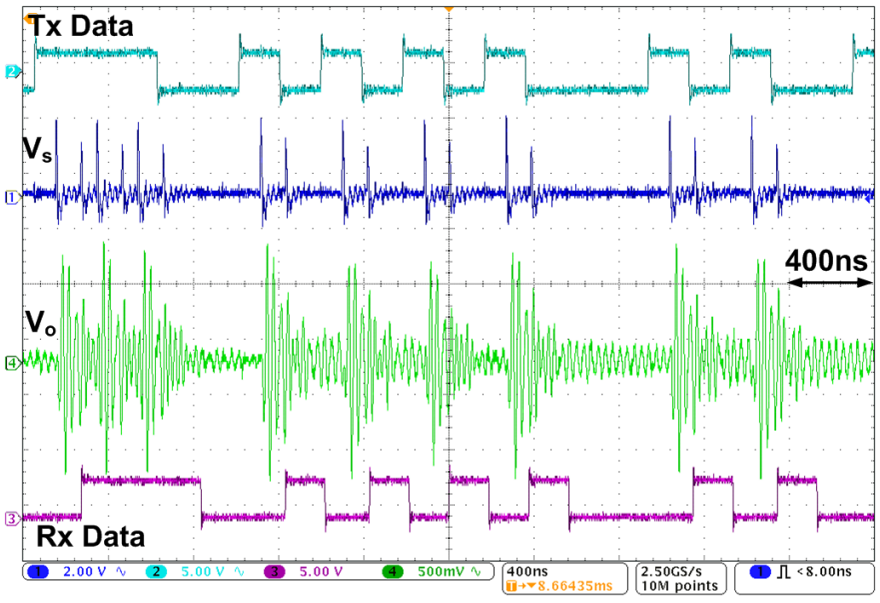

Fig. 46. Measured waveforms from the PHM based transmission setup at 5.2 Mbps with 1 cm separation between coils. From top: Tx serial data bit stream, PHM data pulses at the PPG output V_T (or V_s), received PHM signal across V_R (or V_o), received serial data bit stream.

Fig. 47(a) shows the measured BER at different data rates when *d* was changed from 8 to 20 mm. According to these curves, if the acceptable BER limit is defined at 10^{-6}, then the data rate of this proof-of-concept PHM prototype can be considered to be 5.2 Mbps when *d* = 1 cm. Fig. 47(b) shows the changes in BER as a result of coil misalignments along X and Y axes as shown in Fig. 42. The data rate and coils' distance in this case are kept constant at 5.2 Mbps and 1 cm, respectively. These curves show that the Figure-8 coils are more robust against misalignments along the Y-axis compared to X-axis, which is in agreement with earlier conclusions in [105], which were based on k variations.

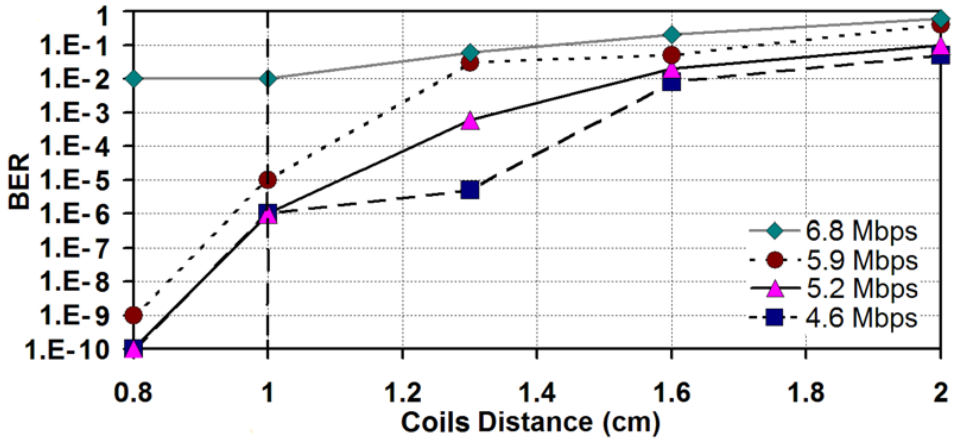

(a)

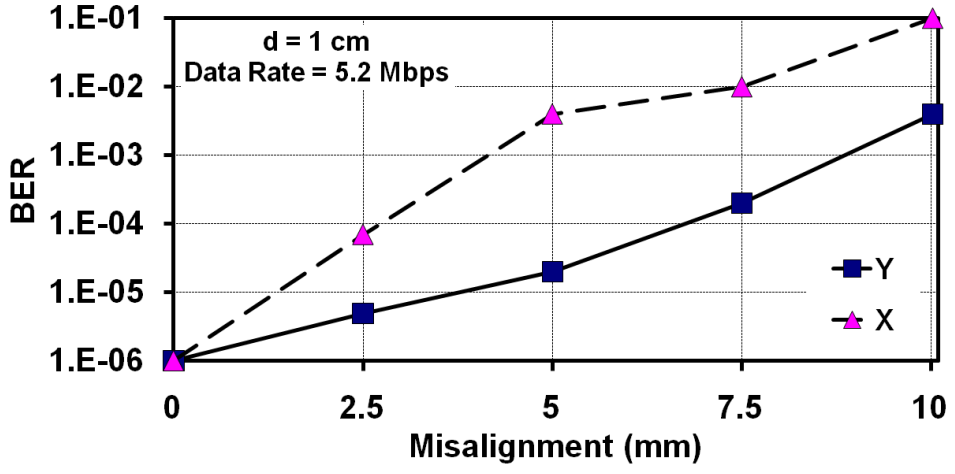

(b)

Fig. 47. (a) BER vs. coils distance, *d*, at different data rates. (b) BER vs. misalignments in the Y and X axis at a data rate of 5.2 Mbps, and *d* = 1 cm.

3.4. PHM ASIC Implementation: A 10.2 Mbps Pulse-harmonic-modulation-based Transceiver for Implantable Medical Devices

In the previous sections the PHM concept and its theoretical analysis was described along with measurements from a discrete proof-of-concept prototype. In this section a fully integrated CMOS transceiver based on the PHM technique is presented, which block diagram is shown in Fig. 48. On the transmitter side (Tx), C_b is charged up to a voltage set by a digital-to-analog converter (DAC) and C_a is charged up to V_{dd}. C_a is then discharged into the primary coil followed by C_b via an LC-Driver circuit according to a specific timing that is dictated by an FPGA that accepts the serial data bit stream to be transmitted (Tx-Data). The sharp current impulses passing through L_1 as a result of C_a/C_b discharges, couple onto the secondary L_2C_2 tank, and initiate/terminate an oscillation at the L_2C_2 resonance frequency, f_r, across the receiver (Rx) input.

Inside Rx, which operates based on a non-coherent energy detection (ncED)

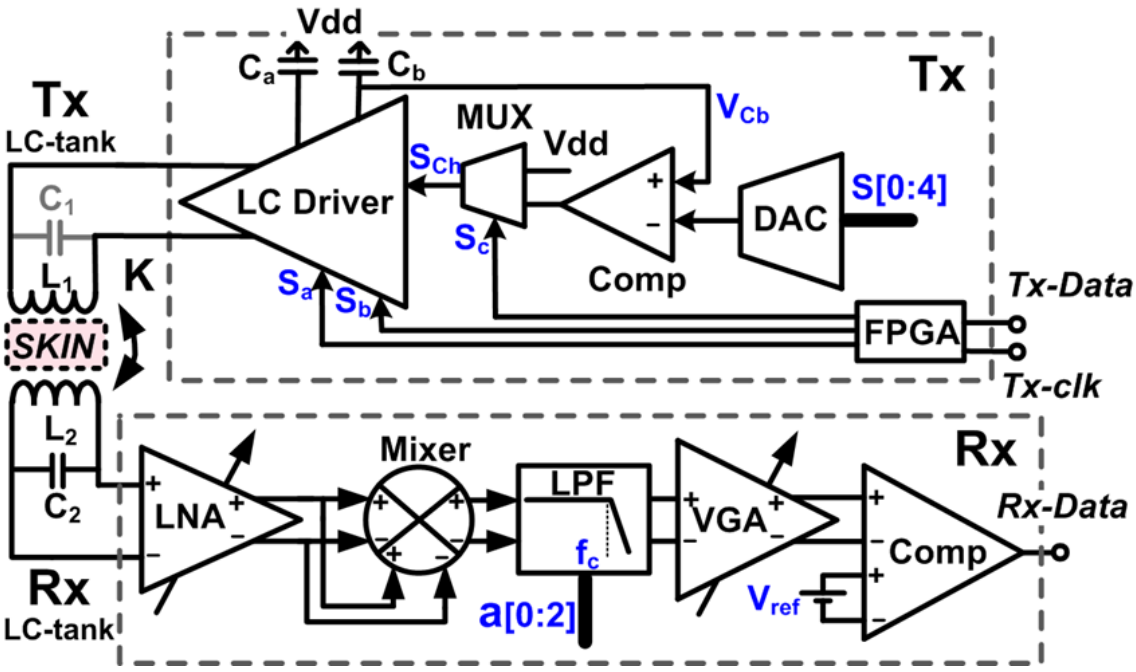

Fig. 48. Block diagram of the Pulse Harmonic Modulation based transceiver. C1 represents the parasitic capacitance of L1 and switches at the output of the LC Driver.

scheme, the received signal is amplified, squared, and low-pass filtered, and finally, a comparator recovers the serial data bit stream.

3.4.1. Transmitter Design

The PHM transmitter, which is enclosed in the upper dashed box in Fig. 48, operates by charging a pair of capacitors, C_a and C_b, up to V_{dd} and V_{dd}-V_{DAC}, respectively, and discharging them into L_1 to generate sharp initiation and suppression pulses. V_{DAC} is provided by a 5-bit DAC, which controls the voltage at the lower terminal of C_b. The DAC was designed based on folded resistor string architecture using 50 kΩ resistors [111]. Fig. 49(a) shows a more detailed schematic of the LC-Driver block in Fig. 48. This

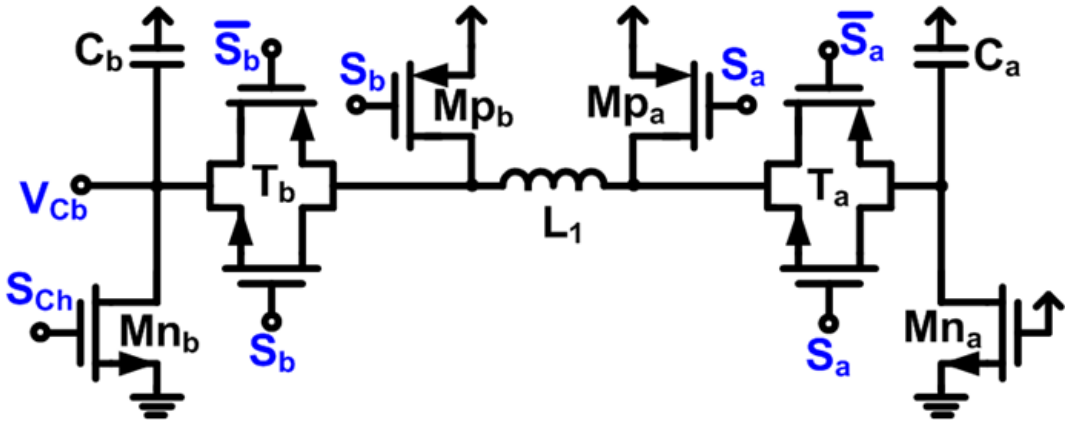

(a)

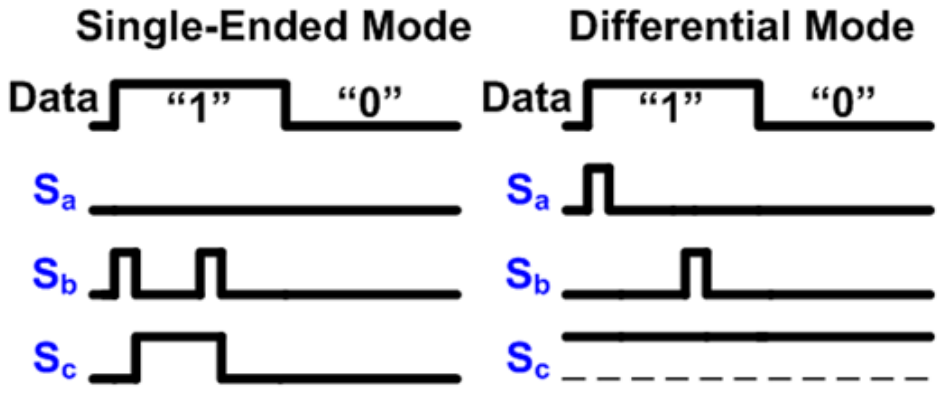

(b)

Fig. 49. (a) Schematic diagram of the LC-Driver block in Fig. 16. (b) LC-Driver timing diagram (S_c is the signal controlling the MUX in the PHM Tx in Fig. 16, which connects S_{ch} to either V_{dd} or the comparator output).

circuit, which is controlled by an off-chip FPGA through S_a and S_b signals, can operate either in single-ended or differential modes, which switching diagram can be seen in Fig 49(b).

In the single-ended mode, S_a = "0" and the right node of L_1 is always connected to V_{dd} by M_{Pa}. To generate the initiation pulse, S_c in Fig. 48 is set to "0", causing the multiplexer in Fig. 48 (MUX) to connect S_{ch} to V_{dd}, to turn M_{nb} on and charge C_b to full scale, i.e. V_{dd}. During this charging period S_b = "0" and T_b gate is open. Therefore, no current passes through L_1. At the onset of a bit "1" period, S_b toggles to "1" for a very short time period, t_{pw} (only a few ns in this design), during which the inductor current, i_1, starts increasing at a rate proportional to $di_1/dt = V_{dd}/L_1$. This current variation in L_1 is responsible for inducing a voltage across L_2, which is depicted as $V_M = Mdi_1/dt \propto V_{dd}$ in Fig. 38. Of course there will also be voltage drops across M_{nb} and T_b, depending on their sizes, which need to be considered in a more detailed analysis. To end the initiation pulse, S_b is toggled back to "0", at which time M_{pb} shorts the left node of L_1 to V_{dd} and provides a path for i_1 to return back to zero without causing undesired oscillations.

After terminating the initiation pulse, the FPGA applies the PHM time delay in (15), t_d, and at the same time prepares the transmitter for generating the suppression pulse by setting S_b = "0", similar to the initiation pulse. The difference, however, is that this time, S_c = "1", causing the MUX to connect S_{ch} to the output of a comparator, which compares V_{Cb} and V_{DAC}. The comparator output is initially high because $V_{Cb} = V_{dd} > V_{DAC}$. Therefore, M_{nb} is turned on and charges C_b up to the point where $V_{Cb} = V_{DAC}$. At this time, the comparator output goes low and turns M_{nb} off to maintain the voltage across C_b at $V_{dd} - V_{DAC}$. The rest of the steps for generating the suppression pulse is similar to the initiation pulse, and includes toggling S_b = "1" for t_{pw} to connect C_b in parallel with L_1 and induce $V_M = Mdi_1/dt \propto V_{dd} - V_{DAC}$ across L_2. Obviously the 5-bit DAC input, S[1:4], can be adjusted such that $(V_{dd} - V_{DAC}) / V_{dd} = P$, which was calculated in (16).

In the differential mode, the initiation pulse is generated by the right side of the LC-Driver in Fig. 49(a) by connecting the left node of L_1 to V_{dd} (S_b = "0") and charging C_a to full scale, i.e. V_{dd}, through M_{na}. At the onset of a bit "1" period, S_a toggles to "1" for t_{pw}, during which i_1 increases towards right. Then both S_a and S_b are lowered, during t_d, to connect both ends of L_1 to V_{dd} and reduce its current. At the same time, C_b is charged to V_{dd} - V_{DAC} and the suppression pulse is generated by the left side of the LC-Driver in the exact same way as in the single-ended mode. It should be noted that in this mode, since the suppression pulse is already out-of-phase with respect to the initiation pulse (i_1 flowing in opposite directions), unlike (15), t_d should be an even multiple of a half cycle, or simply

$$t_d = \frac{N}{f_r} \qquad 4\tau_1 f_r \le N < T f_r. \tag{17}$$

R_{on} of Mn_b and Mn_a should be small to charge C_a and C_b rapidly and meet the timing requirements of the desired data rate. In other words, $R_{on}C_{a,b} << 1/DR$ and W/L for Mn_b and Mn_a should be large. On the other hand, driving larger devices results in higher power consumption per bit. In this design $(W/L)_{Mna,Mnb}$= 20 was chosen as a compromise between DR and power consumption requirements. Similar constraints should be considered in the design of Ta, Tb, Mp_a, and Mp_b, which are much larger devices responsible for driving L_1, and as such should be designed considering the chip area constraints also. In this design, $(W/L)_{Ta,Tb}$ = 1000 and $(W/L)_{Mpa,Mpb}$ = 1167 were selected based on L_1 specifications and post-layout simulation results. It should also be noted that the parasitic capacitances added by these switches to V_{Cb} and L_1 terminals are dwarfed by the parasitic capacitance of L_1 and values of C_a and C_b, which are off-chip components.

3.4.2. Receiver Design

The PHM signal at the Rx input, V_R, is similar to the low-frequency equivalents of the IR-UWB on/off keying (OOK) signals, in which the presence or absence of a number of oscillations within a certain band represent bits "1" or "0", respectively [112], [113]. Among different architectures for such receivers, non-coherent energy detection scheme (ncED) is popular due to its low complexity [114]-[116]. This architecture does not require high power consuming blocks such as local oscillator (LO) or PLL for down-conversion either, which makes it suitable for low power applications. A recent comparison in terms of energy per bit and data rate between coherent and non-coherent UWB and narrowband receivers in [117] showed an order of magnitude lower power consumption in non-coherent receivers for data rates up to 10 Mbps. Moreover, applying this method to high-Q inductive links, which have high selectivity, can diminish some of the drawbacks of the ncED architecture, such as susceptibility to noise and interference. Therefore a standard ncED-based receiver architecture was used for the PHM Rx, the block diagram of which is shown in the lower dashed box in Fig. 48. The PHM signal across V_R is amplified and squared before passing through a Chebyshev LPF for its energy to be compared with a reference value, which is determined by the noise floor and level of interference in the system.

3.4.3. Measurement Results

The PHM transceiver prototype, shown in Fig. 50, was fabricated in a 0.5-µm 3M2P standard CMOS process, occupying 0.61 mm^2 of chip area. Two chips were used in the present experimental setup, shown in Fig. 51. Each chip was glued and wire-bonded directly on a 2-layer custom designed PCB (1 oz copper on 1.5 mm-thick FR4) and covered with epoxy. Each PCB included a 2-turn planar Figure-8 coil (see Fig. 51 inset), which specifications are summarized in Table 4 [105]. The coils were held in parallel and perfectly aligned using only non-conducting materials, such as PVC and

Plexiglas. At d = 1 cm between the two coils and perfect alignment, they had a simulated value of $k = M/\sqrt{(L_1 L_2)} = 0.012$ [105]. In addition, based on $Q_2 = 48$ at $f_r = 67.5$ MHz, the bandwidth of the inductive link can be calculated as $BW = 1.4$ MHz. To minimize the effect of interconnects and SMA connectors on the coils' magnetic field 3.4 cm and 4.25 cm clearance were added on the PCB between the Tx and Rx coils and their associated PHM transceivers, respectively.

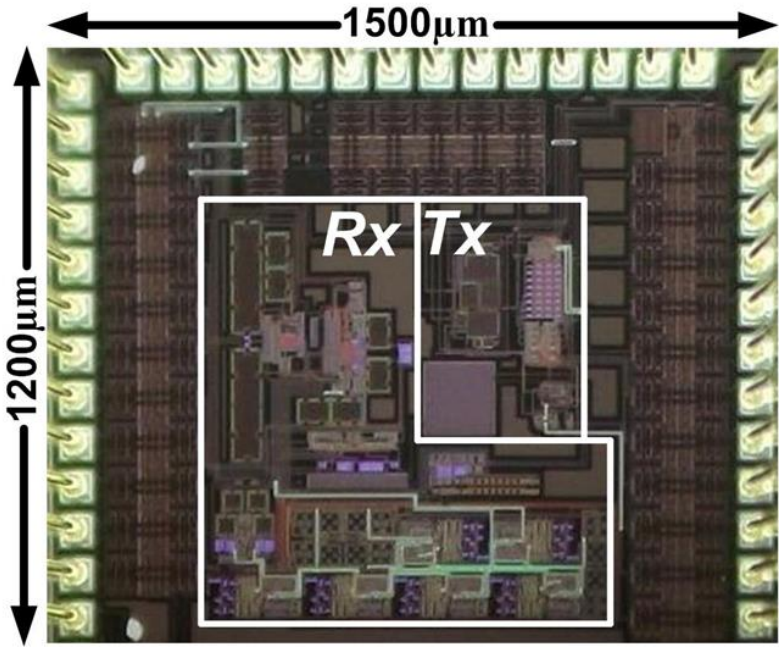

Fig. 50. PHM transceiver chip microphotograph.

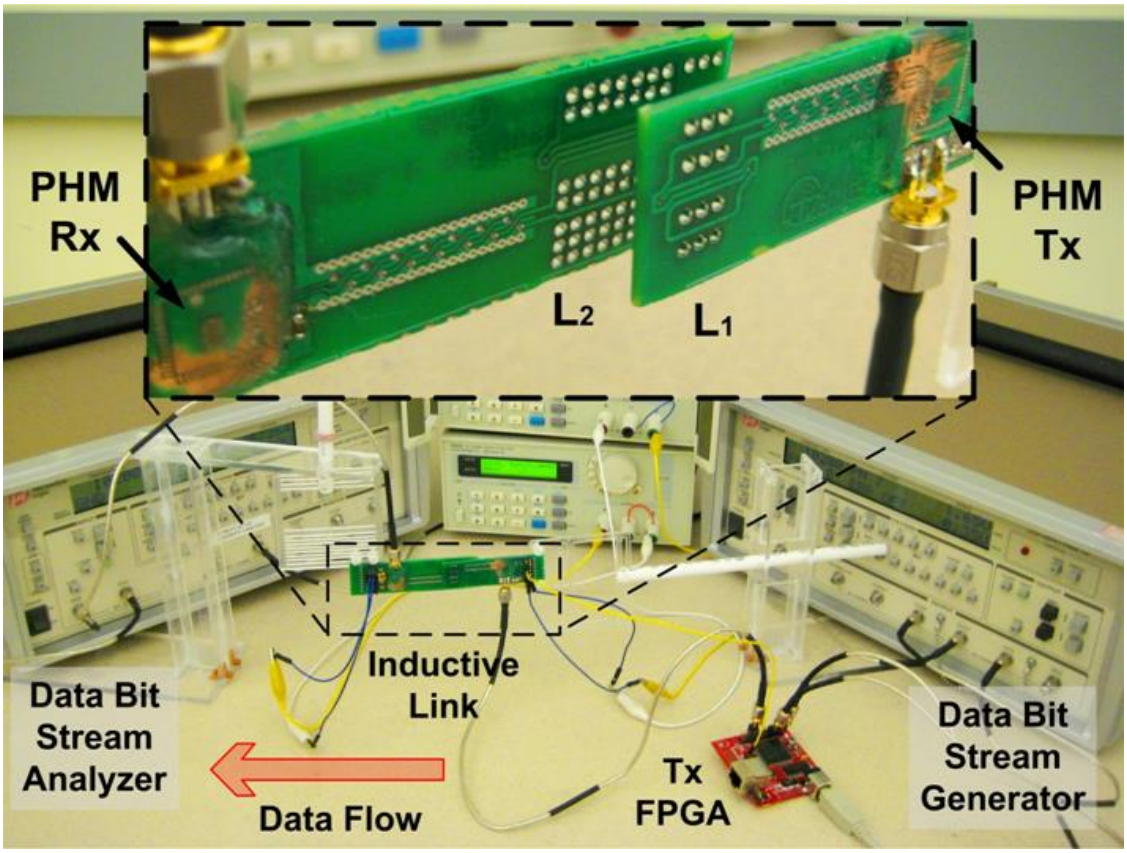

Fig. 51. PHM transceiver measurement setup. Inset: Inductive telemetry link made of a pair of planar Figure-8 coils [105] (L_1 and L_2 in Fig. 48) on FR4 PCB, on which the transceiver chips have been directly wire-bonded.

Table 4
FIGURE-8 COILS SPECIFICATIONS

Coil	Size (cm)	#Turns (n)	Clearance (cm)	L (nH)	R (mΩ)	C_p (pF)	C_t (pF)	SRF (MHz)
L_1 (Tx)	1×1	2	3.4	105	85	2.1	-	338*
L_2 (Rx)	1.5×1.5	2	4.25	230	180	3.2	24.1	184.5*

*From HFSS finite element analysis simulations

In practice, the data coil and transceiver microassembly will be packed inside an IMD with shorter interconnects and smaller parasitic effects, while the tissue volume conductor can add to the coils' parasitic components and reduce their SRF [118].

Generation of the random-serial-data-bit stream to be transmitted, *Tx-Data*, and BER analysis of the recovered data, *Rx-Data*, in Fig. 48 were conducted by a pair of Tektronix GB1400 (GigaBERT), shown in Fig. 51. Once the two GigaBERTs are synchronized via a separate hardwired clock signal, *Tx-clk* in Fig. 48, they can measure the wireless link BER in real time. Instead of the receiver block in the PHM transceiver chip, initially a custom-designed discrete RF receiver was used, in which easier access to the internal nodes was available, to observe and evaluate the effects of PHM on the received signal. Probing the inductive link directly was avoided because this could change its characteristics.

To achieve DR > 10 Mbps, which was the target for this PHM transceiver prototype, the oscillation across L_2C_2 must be initiated and suppressed within T = 100 ns. If N = 3 complete cycles for the oscillation is dedicated to build up after the initiation pulse, and three more cycles for the oscillation to die out after the suppression pulse, before the next bit arrives, then f_r needs to be > 60 MHz. It should also be pointed out that in a second order system with $\zeta_2 = 0.02 << 1$, such as $R_2L_2C_2$ in Fig. 38,

$$M_{Peak2} = \frac{1}{2\zeta_2\sqrt{1-\zeta_2^{\,2}}} \approx Q_2 = \frac{1}{R_2}\sqrt{\frac{L_2}{C_2}} = 48 \ , \tag{18}$$

where M_{Peak2} is the peak magnitude of the transfer function, i.e. the 2nd term in the denominator of (1). Therefore, increasing f_r by reducing C_2 while maintaining L_2 constant can lead to higher Q_2 and higher gain for the inductive link, both of which can lead to better SNR at the receiver input. This is a major advantage of the PHM over previous wideband carrier-less data transmission methods, which can only operate when the link Q-factor is low. High gain and Q-factor are key in inductive data links used in IMDs because the coils distance, *d*, is in the cm range, orders of magnitude larger than applications such as chip-to-chip communication [100], and there might be a strong interference from a nearby inductive power carrier [91].

For the above reasons, f_r = 67.5 MHz was chosen. Using the coils specified in Table 4 and N = 3, the main PHM parameters were found to be $t_d \approx 52$ ns and P = 0.92 based on (15) and (16), respectively. In Table 4, it can be seen that no tuning capacitor (C_t) has been used for the primary coil to reduce Tx power consumption. It was also noticed that at this f_r, since $t_d << \tau_2 = 2.5$ µs, the performance of the PHM transceiver is not very sensitive to P, and the wireless link also works fine with $P \approx 1$. Therefore, the PHM Tx was set to operate in the single-ended mode to further reduce power consumption. Figs. 52(a) and 52(b) from top to bottom show one of the LC-Driver control signals, S_b, which was applied to the PHM Tx as shown in Fig. 48, the received RF signal at the output of the LNA, which is proportional to V_R at the input of the receiver, and the LPF output, which is proportional to the energy content of the received pulse around f_r, with and without PHM, respectively. It can be seen that the elimination of the suppression pulse in Fig. 52(b) renders the received data completely undetectable at DR = 10.2 Mbps, while Fig. 52(a) clearly shows the effectiveness of the PHM in reducing the ISI. Considering $V_T = V_{dd}$ = 3.3 V and the model shown in Fig. 38, the channel loss in these measurements was $-20\log(V_R/V_T)$ = 40 dB.

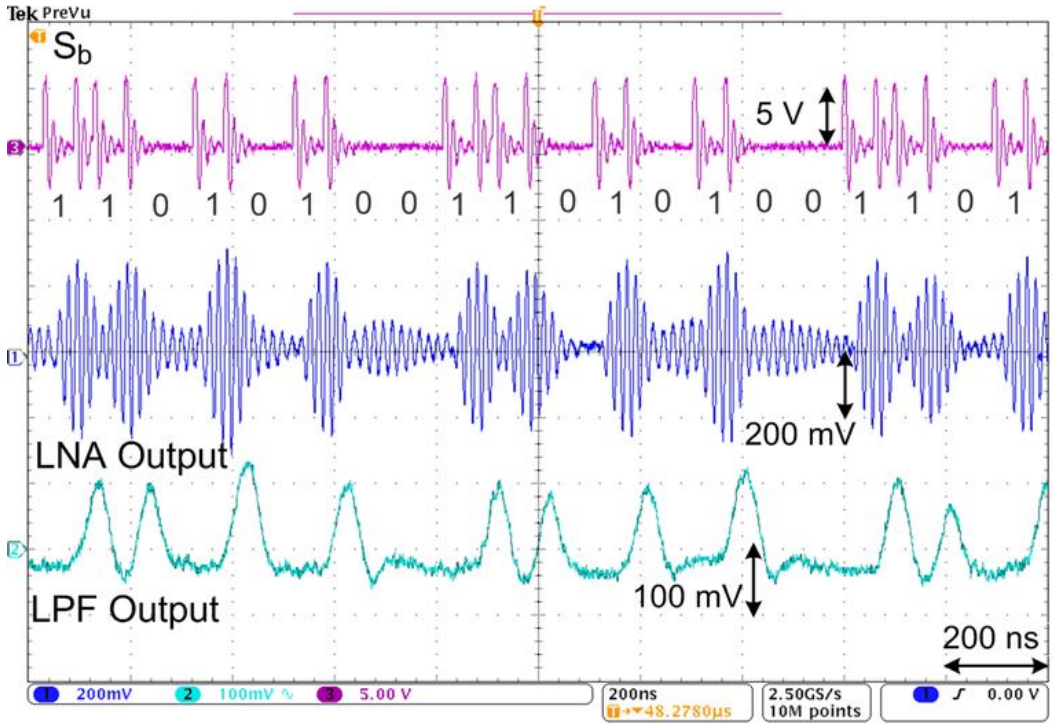

(a)

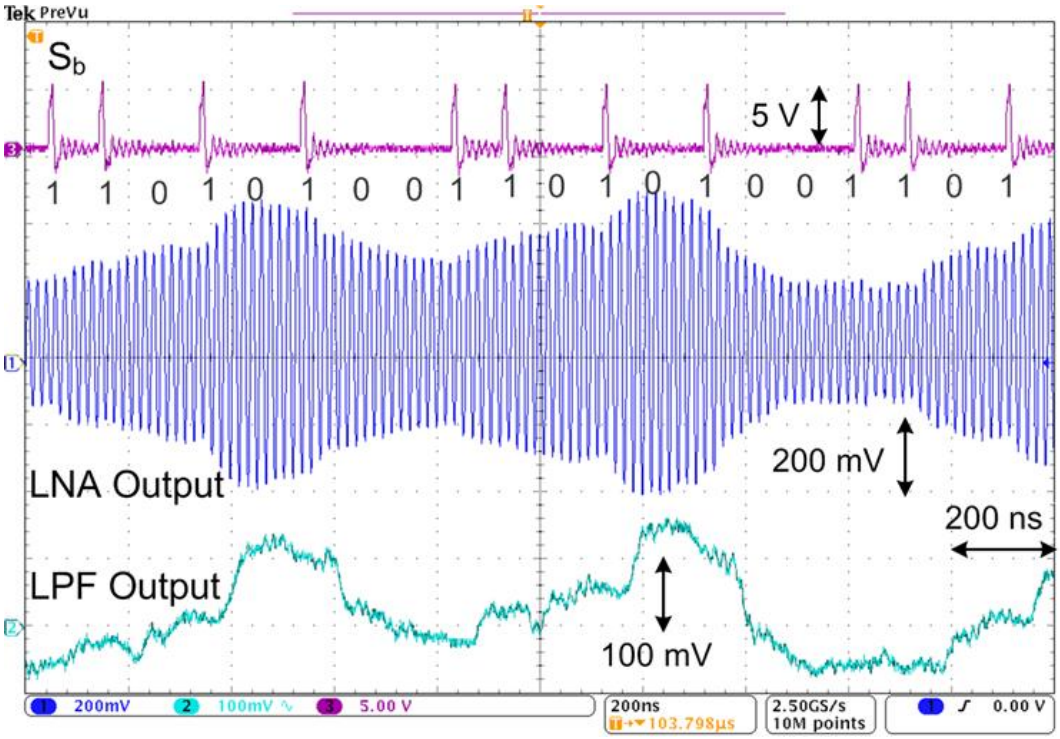

(b)

Fig. 52. Transmitter waveforms at the LC-Driver input and receiver waveforms at the LNA and LPF outputs of the custom designed receiver, (a) with and (b) without PHM, when f_r = 67.5 MHz, *DR* = 10.2 Mbps, N = 3, t_d = 52 ns, P = 1, t_{pw} = 7 ns, and d = 10 mm. Elimination of the suppression pulse in (b) renders the received data completely undetectable as a result of strong ISI.

Fig. 53 shows a snapshot of the key measured waveforms in the PHM transceiver setup of Fig. 51. From top, the transmitted serial data bit stream at *DR* = 10.2 Mbps, S_b of the LC-Driver, receiver VGA output, and recovered serial data bit stream are shown with the Figure-8 coils aligned at *d* = 10 mm. In Fig. 53(b), because of the strong ISI in the absence of the suppression pulse, the receiver has failed to recover the serial data bit stream at this data rate. On the other hand, utilizing the PHM technique in Fig. 53(a) has resulted in correct detection of the serial data bit stream in an otherwise similar condition.

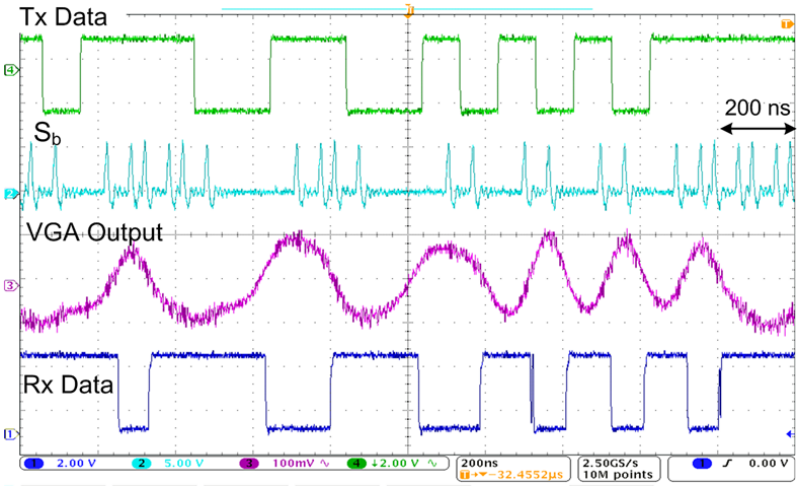

(a)

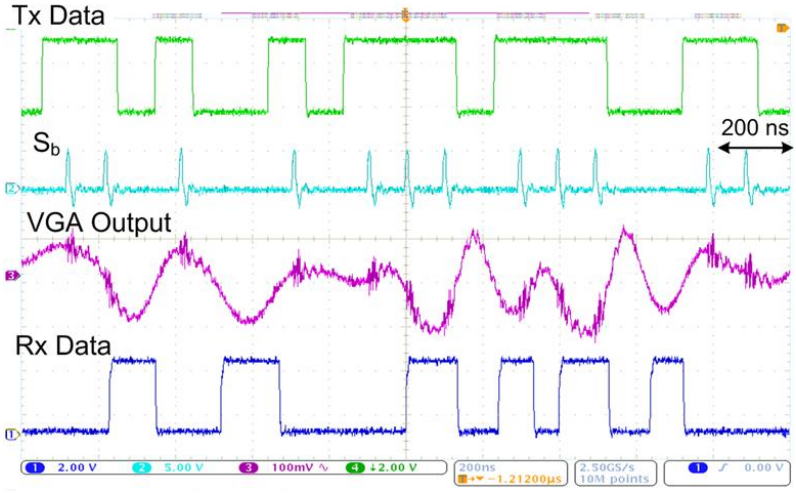

(b)

Fig. 53. PHM transceiver waveforms from top: Transmitted serial data bit stream at 10.2 Mbps, one of the LC-Driver control signals, receiver VGA output, and recovered data bit stream, (a) with and (b) without PHM. It can be seen that while everything between these two measurements are the same, without PHM the Rx Data in (b) is completely erroneous.

To better characterize the performance of the PHM-based transceiver, BER was measured at various data rates, while changing *d* from 5 to 10 mm. The results, shown in Fig. 54, indicate that if the acceptable BER limit is considered 10^{-7}, then the best data rate that can be achieved with the current PHM transceiver at *d* = 10 mm is 10.2 Mbps. The PHM Tx supply voltage, V_{dd}, in this case was at 3.3 V, consuming 3.52 mW, which is the equivalent of 345 pJ/bit. The PHM Rx power consumption in these conditions was 3 mW. Consuming the same amount of power at *d* = 5 mm resulted in *DR* = 10.9 Mbps at BER = 10^{-6}. It should be noted that the receiver bandwidth limitation is the main reason for high BER at 11.4 Mbps and 12 Mbps. The cutoff frequency of the Chebyshev LPF in the Rx should be increased to achieve higher data rates. Also the Signal to Interference decreases as a result of the ISI when the PHM pulses are too close to each other at high data rates, which leads to more BER degradation. Without PHM, on the other hand, the data rate could only reach 1.5 Mbps at *d* = 10 mm with BER = 10^{-5}. Table 5 summarizes the key specifications of the PHM transceiver ASIC.

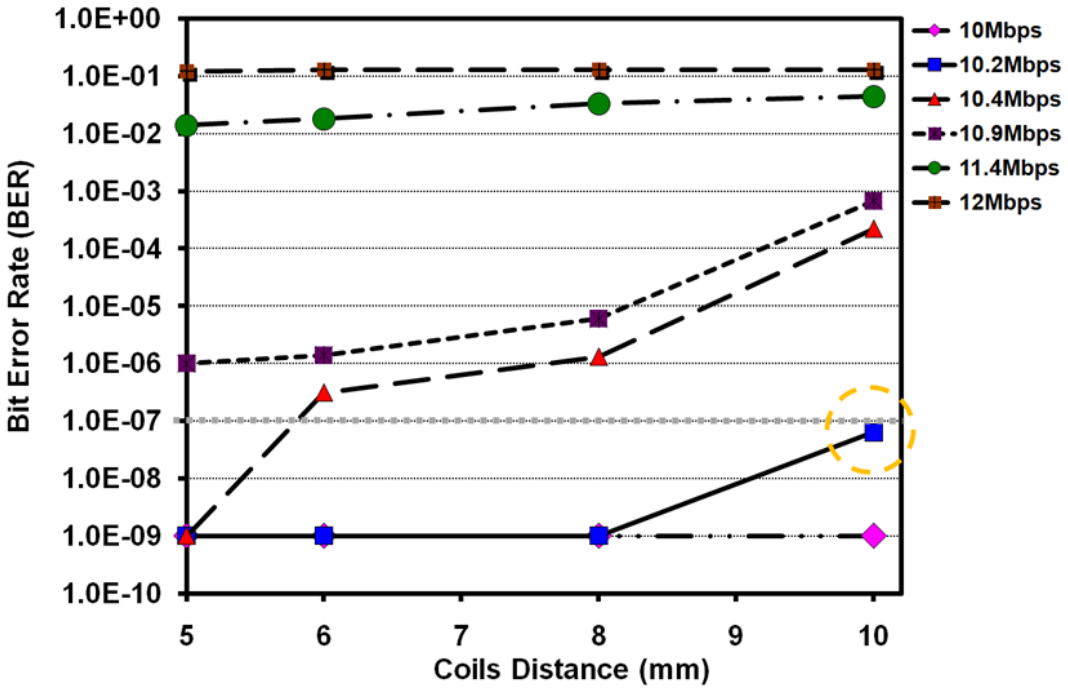

Fig. 54. BER *vs*. coils distance, *d*, at different data rates, when PHM-Tx supply voltage is constant at V_{dd} = 3.3 V.

Table 5
PHM-BASED TRANSCEIVER SPECIFICATIONS

Technology (ON Semiconductor)		0.5-µm 2P3M CMOS
Supply voltage		3.3 V
Data rate, *DR*		10.2 Mbps
Pulse specs: t_d / P / t_{pw}		52 ns / ~1 / ~7 ns
Bit error rate (BER)		6.3×10^{-8}
Nominal coils distance, *d*		10 mm
Power consumption	Tx	345 pJ/bit (3.52 mW)
	Rx	3 mW
Area on chip	Tx	0.1088 mm^2
	Rx	0.5076 mm^2
Die size		1.5 mm × 1.2 mm

Even though the present transceiver has not been optimized for minimum power consumption in this large feature sized and relatively high threshold voltage process, the PHM Tx power was lowered by reducing its V_{dd} from 3.3 V down to 2.4 V, while measuring the BER at d = 10 mm. Fig. 55 depicts the results of this experiment, which demonstrates the strong relationship between BER, Tx power, and Rx sensitivity.

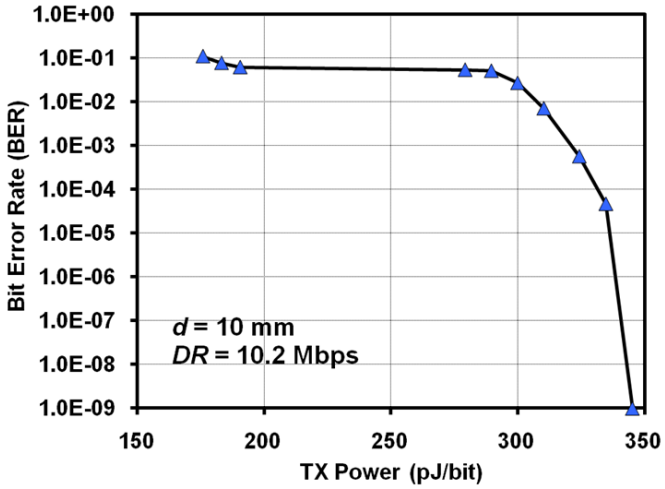

Fig. 55. BER *vs.* transmitter power consumption at d = 10 mm and DR = 10.2 Mbps, when V_{dd} of the PHM-Tx has been reduced from 3.3 V to 2.4 V.

To accurately measure the minimum required energy to transfer high speed data and compare the PHM transceiver performance with other recently published near-field data telemetry links, d was reduced down to ~ 0.1 mm by separating the two coils with a

sheet of paper and lowering V_{dd} down to 1.2 V. Since the FPGA was still operating at 3.3 V, the PHM-Tx control signals in Fig. 38 were also divided down to 1.2 V. Finally, t_{pw} was reduced from 7 ns to ~3 ns using the FPGA gate delays [108]. The average energy consumption in this case was measured by differentially recording the voltage across a resistor in series with the PHM-Tx supply pin, and integrating it over a certain period of time as random data was being transferred across the link at 10.2 Mbps. The results showed that for a BER < 10^{-7} the PHM-Tx power consumption was only 8.85 pJ/bit, which can be further reduced by migrating the PHM transceiver to smaller feature sized processes.

Finally, Table 6 presents a benchmarking of recent inductive data telemetry links. It can be seen that the PHM transceiver can achieve a data rate of 10.2 Mbps with a BER of 6.3×10^{-8} across a 10 mm inductive link, set up between 1 and 2.25 cm^2 Figure-8 coils.

Table 6
BENCHMARKING of INDUCTIVE-DATA-TELEMETRY LINKS

Ref.	***Modulation Scheme***	***Size Tx/Rx (cm)***	***Coils Distance (mm)***	***f_r (MHz)***	***Data Rate (Mbps)***	***Tx Power (pJ/bit)***	***Rx Q at low freq***	***BER***
[80]	pcFSK	2/1.2	5	5/10	2.5	N/A	N/A	10^{-5}
[86]	BPSK	3.5/2.7	15	10	1.12	N/A	N/A	10^{-5}
[87]	BPSK	N/A	10~15	20	2	N/A	N/A	10^{-7}
[88]	QPSK	1.2/1.2	5	13.56	4.16	N/A	65.6^{**}	2×10^{-6}
[94]	LSK	3.5/3.5	20	25	2.8	35.7^{+}	30	10^{-6}
[104]	BPM^{++}	1.5/1.5	0	-	10	2.9	15	N/A
This Work	**PHM**	**1/1.5**	**0.1**	**(67.5)**	**10.2**	**8.85**	**541.9**	**$<10^{-7}$**
This Work	**PHM**	**1/1.5**	**10**	**(67.5)**	**10.2**	**345**	**541.9**	**6.3×10^{-8}**

CONCLUSION AND FUTURE WORK

The work gained new understanding of novel practices in the design of wireless transceivers for low-power advanced applications. A novel design procedure for low-voltage low-power LNAs utilizing weakly saturated SiGe HBTs was introduced while design tradeoffs in designing with weakly saturated SiGe HBTs were identified. This lead to the design and characterization of a 1.0 V, 10-22 GHz, 4 mW LNA utilizing weakly saturated SiGe HBTs for single-chip, low-power, remote sensing applications achieving a 4 mW record lowest power reported wide-band LNA spanning X, K, Ku bands.

Applying the low-power properties of impulse-radio transceivers to low-power space-based/high-altitude remote sensing applications, a CMOS pulse generator and a SiGe HBT Gaussian pulse generator were designed and total ionizing dose effects were investigate leading to a comparative study of the CMOS and HBT Pulse Generators with the SiGe design being the clear front runner. Furthermore circuit-level TID effects were linked to device level effects.

Two compact, low-power, single-ended and differential SiGe W-band LNAs were designed and characterized for phased array radar applications achieving lowest power reported Si-based W-band LNA of 8.8 mW from 2.2 V, and lowest NF reported W-band LNA (Sub-4 dB) leading to a functional 94 GHz transceiver receiver.

Proposed and developed novel modulation technique named Pulse Harmonic Modulation (PHM) for wideband near-field data telemetry in high Q-factor links while developing time-domain theoretical analysis for data telemetry inductive links leading to the design and characterization of a low-power pulse harmonic modulation transceiver achieving a record high data rate of 10.2 Mbps.

Future Work

Significant opportunities exist for future work stemming from this research.

- Design of 1-V Rx front end using weakly saturated devices for a low-power single-chip receiver solution
    - 1-V switch
    - 1-V Mixer

- Investigation of transient radiation effects on pulse generators
    - System-level characterization of transient effects

- Design of upconverted Gaussian pulse generators and conduct radiation study

- Design of self-healing mechanism for CMOS pulse generator through the adaptive adjustment of I_{bias}

- Measurement and characterization of the complete 94 GHz transceiver radar

REFERENCES

[1] F. Inanlou, C. T. Coen, J. D. Cressler, "A 1.0 V, 10-22 GHz, 4 mW LNA utilizing weakly saturated SiGe HBTs for single-chip, low-power, remote sensing," Submitted, *IEEE Microw. Wireless Compon. Lett.*, 2014.

[2] F. Inanlou, E. W. Kenyon, J. D. Cressler, "An investigation of total ionizing dose damage on a pulse generator intended for space-based impulse radio UWB transceivers," *IEEE Trans. Nucl. Sci.*, vol. 60, no. 4, pp. 2605–2610, Aug. 2013.

[3] F. Inanlou, E. W. Kenyon, J. D. Cressler, "An investigation of total ionizing dose damage on a pulse generator intended for space-based impulse radio UWB transceivers," Presented at *IEEE Radiation Effects on Components and Systems*, 2012.

[4] F. Inanlou, N. Lourenco, Z. Fleetwood, I. Song, D. Howard, A. Cardoso, J. D. Cressler, "Impact of total ionizing dose on a 4th generation, 90 nm SiGe HBT gaussian pulse generator technology ," to be presented at *IEEE Nuclear and Space Radiation Effects Conference*, 2014.

[5] F. Inanlou, N. Lourenco, Z. Fleetwood, I. Song, D. Howard, A. Cardoso, J. D. Cressler, "Impact of total ionizing dose on a 4th generation, 90 nm SiGe HBT gaussian pulse generator technology ," in preparation to be submitted to *IEEE Trans. Nucl. Sci.*, 2014.

[6] F. Inanlou, W. Khan, P. Song, S. Zeinolabedinzadeh, R. L. Schmid, T. Chi, A. C. Ulusoy, J. Papapolymerou, H. Wang, J. D. Cressler, "Compact, low-power, single-ended and differential SiGe W-band LNAs with 4.2 dB NF at 94 GHz," to be presented at *IEEE European Microwave Integrated Circuits*, 2014.

[7] F. Inanlou, M. Ghovanloo, "Wideband near-field data transmission using pulse harmonic modulation," *IEEE Trans. Cir. Sys. I*, vol. 58, no. 1, pp. 186-195, Jan. 2011.

[8] F. Inanlou, M. Kiani, M.Ghovanloo, "A novel pulse-based modulation technique for wideband low power communication with neuroprosthetic devices," *IEEE Eng. Med. Biol. Conf.*, pp. 5326-5329, Aug. 2010.

[9] F. Inanlou, M. Kiani, M. Ghovanloo, "A 10.2 Mbps pulse harmonic modulation based transceiver for implantable medical devices," *IEEE J. Solid-State Circuits*, vol. 46, no. 6, pp. 1296-1306, June. 2011.

[10] F. Inanlou, M. Ghovanloo, "Pulse harmonic modulation systems and methods," US Patent Allowed (To be Issued), Filing date: July 2012, Approved: Feb 2014, US Patent Application 13/521,123.

[11] J. K. Erickson, “Living the dream-An overview of the Mars exploration project,” *IEEE Robot. Autom. Mag*., vol. 13, pp. 12-18, June. 2006.

[12] [Online]. Available: http://www.nasa.gov/mission_pages/viking/index.html

[13] R. Cook, “Mars pathfinder missionoperations: Faster, better, cheaper on Mars,” in *Proc. IEEE Aerospace. Conf. 1998*, Mar. 21-28, 1998, vol. 5, pp. 413-420.

[14] W. Kuhn, N. E. Lay, E. Grigorian, D. Nobbe, I. Kuperman, J. Jeon, K. Wong, Y. Tugnawat, and X. He, "A microtransceiver for UHF proximity links including Mars surface-to-orbit applications," *Proc. IEEE*, vol. 95, pp. 2019-2044, Oct. 2007.

[15] A. J. Barbieri, S. Butmann, M. J. Danos, E. Greenberg, P. A. Ilott, G. J. Kazz, J. L. Torgerson, A. Vaisnys, W. R. Adams, C. E. Johnson, M. Dapore, and D. Merz, “Development and flight performance of CCSDS proximity-1 on Odyssey and the Mars exploration rovers,” in *Proc. IEEE Aerospace Conf. 2005*, Mar. 5-12, 2005, pp. 1444-1454.

[16] NASA Goddard Space Flight Center, *National Space Center Data Center Master Catalog*, Greenbelt, MD, 2005. [Online]. Available: http://www.nssdc.gsfc.nasa.gov

[17] NASA-Space Environments and Effects (SEE) Program, *NASA SEE TWG*-Ionosphere and Thermosphere, 2009. Available at http//:see.msfc.nasa.gov/pf/pf .htm.

[18] J.D. Cressler, The Silicon Heterostructure Handbook: Materials, Fabrication, Devices, Circuits, and Applications of SiGe and Si Strained-Layer Epitaxy, CRC Press, 2005.

[19] J.D. Cressler and G. Niu, Silicon-Germanium Heterojunction Bipolar Transistors, Boston: Artech House, 2003.

[20] (2006) DARPA's ISIS project seeks slow, soaring surveillance superiority (updated). [Online]. Available: http://www.defenseindustrydaily.com

[21] D. Ma, F. Dai, R. Jaeger, J. Irwin, “An X- and Ku-band wideband recursive receiver MMIC with gain-reuse,” *IEEE J. Solid-State Circuits*, vol. 46, no.3, pp. 562-571, March 2011.

[22] L. Liang, A. Alt, H. Benedickter, C. R. Bolognesi, ”InP-HEMT X-band low-noise amplifier with ultralow 0.6-mW power consumption," *IEEE Electron Device Lett*., vol. 33, no. 2, pp. 209-211, 2012.

[23] S. Seth, L. Najafizadeh, J. D. Cressler, “On the RF properties of weakly-saturated SiGe HBTs and their potential use in ultralow-voltage circuits,” *IEEE Electron Device Lett.*, vol. 32, no. 1, pp. 3-5, 2011.

[24] C. Andrei, R. Doerner ,O. Bengtsson ,S. A. Chevtchenko ,W. Heinrich and M. Rudolph, "Highly linear X-band GaN-based low-noise amplifier*," Proc. Int. Symp. Signals, Syst., Electron*., pp. 1-4, 2012.

[25] R. J. Doviak, D. S. Zrnić, *Doppler Radar and Weather Observations*. Mineola, NY: Dover Publications, 2006.

[26] H. Chen, Y. Lin, S. Lu, "Analysis and design of a 1.6-28-GHz compact wideband LNA in 90-nm CMOS using a π-Match input network," *IEEE Trans. Microw. Theory Tech.*, vol. 58, no. 8, pp. 2092-2104, Aug 2010.

[27] M. Chen, J. Lin, "A 0.1-20 GHz low-power self-biased resistive feedback LNA in 90 nm digital CMOS," *IEEE Microw. Wireless Compon. Lett*., vol. 19, no. 5, pp. 323-325, May 2009.

[28] M. Okushima, J. Borremans, D. Linten, G. Groeseneken, "A DC-to-22 GHz 8.4mW compact dual-feedback wideband LNA in 90 nm digital CMOS," *IEEE Radio Freq. Integr. Circuits Symp.*, 2009, pp. 295-298.

[29] D. Ma, F. Dai, R. Jaeger, J. Irwin, “An 8 – 18 GHz wideband SiGe BiCMOS low noise amplifier,” *IEEE MTT-S Int. Microw. Symp.*, 2009, pp. 673–676.

[30] FCC Rules and Regulation, MICS Band Plan, pt. 95, 2003.

[31] A. P. chandrakasan, F.S. Lee, D. D. Wentzloff, V. Sze, B. P. Ginsburg, P. P. Mercier, D. C. Daly, and R. Blazquez, “Low-power impulse UWB architectures and circuits,” *Proc. IEEE*, vol. 97, no. 2, pp. 332-352, Feb. 2009.

[32] M. Z. Win and R. A. Scholtz, “Impulse radio: How it works,” *IEEE Commun. Lett.*, vol. 2, no. 2, pp. 36-38, Jan. 1998.

[33] S. Iida, K. Tanaka, H. Suzuki, N. Yoshikawa, N. Shoji, B. Griffiths, D. Mellor, F. Hayden, I. Butler, and J. Chatwin, "a 3.1 to 5 GHz CMOS DSSS UWB transceiver for WPANs," *in IEEE Int. Solid-State Circuits Conf. Dig. Tech. Papers*, Feb. 2005, pp.214-215.

[34] L. Yang and G. B. Giannakis, "Ultra-wideband communication: an idea whose time has come*," IEEE Signal Process. Mag*., pp. 26-54, Nov. 2004.

[35] *IEEE Standard for Information Technology-Telecommunications and Information Exchange Between Systems-Local and Metropolitan Area Networks-Specific Requirement Part 15.4: Wireless Medium Access Control (MAC) and physical Layer (PHY) Specifications for Low-Rate Wireless Personal Area Networks (WPANs),* IEEE std. 802.15.4a-2007, 2007, (*Amendment to IEEE Std. 802.15.4-2006*), pp. 1-203.

[36] A. M. El-Gabaly and C. E. Saavedra, "A quadrature pulse generator for short-range UWB vehicular radar applications using a pulsed oscillator and a variable attenuator," *IEEE Trans. Circuits Syst. I*, vol. 58, no. 10, pp. 2285-2295, Oct. 2011.

[37] S. Lee, C-Y. Kim, S. Hong, "A K-band CMOS UWB radar transmitter with a bi-phase modulation pulsed oscillator," *IEEE Trans. Microw. Theory Tech*., vol. 60, no.4, pp. 1405-1412, May. 2012.

[38] S. Bourdel, Y. Bachelet, J. Gaubert, R. Vaucher, O. Fourquin, N. Dehaese, H. Barthelemy, "A 9-pJ/Pulse 1.42-Vpp OOK CMOS UWB pulse generator for the 3.1–10.6-GHz FCC band", *IEEE Trans. Microw. Theory Tech*., vol. 58, no. 1, pp. 65-73, Jan. 2010.

[39] S. Sim, D.-W. Kim, and S. Hong, "A CMOS UWB Pulse Generator for 6-10 GHz Applications," *IEEE Microwave Wireless Compon. Lett*., vol.19, no.2, pp. 83-85, Feb. 2009.

[40] T. A. Phan, V. Krizhanovskii, and S. G. Lee, "Low-power CMOS energy detection transceiver for UWB impulse radio system,"in *Proc. IEEE costume Integrated Circuits conf. (CICC)*, 2007, pp. 675-678.

[41] J.D. Cressler, M. Hamilton, R. Krithivasan, H. Ainspan, R. Groves, G. Niu, S. Zhan, Z. Jin, C. Marhsall, P.Marshall, H. Kim, R. Reed, M. Palmer, A. Joseph, and D. Harame, "Proton response of SiGe HBT analog and RF circuits and passives," *IEEE Trans. Nucl. Sci.*, vol. 48, pp. 2238-2243, Dec. 2001.

[42] A. Sutton, B. Haugerud, Y. Lu, W.-M.L. Kuo, J.D. Cressler, P. Marshall, R. Reed, J.-S. Rieh, G. Freeman, and D. Ahlgren, "Proton response of 4th-generation 350 GHz UHV/CVD SiGe HBTs," *IEEE Trans. Nucl. Sci.*, vol. 51, pp. 3736-3742, Dec. 2004.

[43] T. Thrivikraman, E. Wilcox, S.D. Phillips, J.D. Cressler, C. Marshall, G. Vizkelethy, P. Dodd, and P. Marshall, "Design of digital circuits using inverse-mode cascode SiGe HBTs for single event upset mitigation," *IEEE Trans. Nucl. Sci.*, vol. 57, pp. 3582-3587, Dec. 2010.

[44] J.D. Cressler, "Silicon-Germanium as an enabling technology for extreme environment electronics," *IEEE Transactions on Device and Materials Reliability*, vol. 10, pp. 437-448, Dec. 2010.

[45] J.D. Cressler, "SiGe HBT technology: A new contender for Si-based RF and microwave circuit applications," *IEEE Trans. Micro. Theory Tech.*, vol. 46, pp. 572-589, May. 1998.

[46] F. Faccio and G. Cervelli, "Radiation-induced edge effects in deep submicron CMOS transistors," *IEEE Trans. Nucl. Sci.*, vol. 52, no. 6, pp. 2413–2420, Dec. 2005.

[47] F.L. Kastensmidt, E.C. Fonseca, R.G. Vaz, O.L. Goncalez, R. Chipana, G. I. Wirth, "TID in flash-based FPGA: Power supply-current rise and logic function mapping effects in propagation-delay degradation," *IEEE Trans. Nucl. Sci*, vol. 58, no.4, pp. 1927-1934, Aug. 2011.

[48] M. Gaillardin, V. Goiffon, S. Girard, M. Martinez, P. Magnan, P. Paillet, "Enhanced radiation-induced narrow channel effects in commercial 0.18μm bulk technology," *IEEE Trans. Nucl. Sci*, vol. 58, no.6, pp. 2807-2815, Dec. 2011.

[49] E. W. Kenyon, N. E. Lourenco, E. X. Zhang, S. Jain, J.D. Cressler, D.M. Fleetwood, R.D. Schrimpf, "Capabilities of a 180 nm SiGe BiCMOS technology platform for focal plane array applications in an unshielded Europa environment" *IEEE Nucl. & Space Rad. Eff. Conf.*, July. 2012.

[50] D. R. Alexandar, "Design issues for radiation tolerant micro circuits for space," *IEEE Nuclear and Space Radiation Effects Conference Short Course*, July. 1996.

[51] N. Nowlin, J. Bailey, R. Tuffler, D. Alexandar, “A total dose hardening- by-design approach for high-speed mixed-signal CMOS integrated circuits,” *Int. J. High Speed Electron. Syst*., 14(2), 367-378, 2004.

[52] J. D. Cressler, *Extreme Environment Electronics*. Boca Raton: CRC Press, 2013.

[53] D.C. Howard, P.K. Saha, S. Shankar, R. Diestelhorst, T. D. England, N.E. Lourenco, E. Kenyon, J.D. Cressler, “ An 8-16 GHz SiGe low noise amplifier with performance tuning capability for mitigation of radiation-induced performance loss,” *IEEE Trans. Nucl. Sci.*, vol. 59, no. 6, pp. 2837-2846, Dec. 2012.

[54] P.K. Saha, D.C. Howard, S. Shankar, R. Diestelhorst, T. England, J.D. Cressler, “A 6-20 GHz adaptive SiGe image reject mixer for a self-healing receiver,” *IEEE J. Solid-State Circuits*, vol. 47, no. 9, pp. 1998-2006, Sep. 2012.

[55] M. Cavallaro, T. Copani, and G. Palmisano, “A gaussian pulse generator for millimeter-wave applications,” *IEEE Trans. Circuits Syst. I*, vol. 57, no. 6, pp. 1212–1220, Jun. 2010.

[56] F. Inanlou, E. W. Kenyon, and J. D. Cressler, “An investigation of total ionizing dose damage on a pulse generator intended for space-based impulse radio UWB transceivers,” *IEEE Trans. Nucl. Sci*., vol. 60, no. 4, pp. 2605–2610, Aug. 2013.

[57] L. Zhou, C.-C. Wang, Z. Chen, and P. Heydari, “A W-band CMOS receiver chipset for millimeter-wave radiometer systems,” *IEEE J. Solid-State Circuits*, vol. 46, no. 2, pp. 378 –391, February 2011.

[58] J. May, R. Alhalabi, and G. Rebeiz, “A 3 G-Bit/s W-band SiGe ASK receiver with a high-efficiency on-chip electromagnetically-coupled antenna,” in *IEEE Radio Frequency Integrated Circuits Symposium*, May 23-25, 2010, Anaheim, CA, pp. 87 –90.

[59] E. Dacquay, A. Tomkins, K. Yau, E. Laskin, P. Chevalier, A. Chantre, B. Sautreuil, and S. Voinigescu, “D-band total power radiometer performance optimization in an SiGe HBT technology,” *IEEE Trans. Microw. Theory Tech.*, vol. 60, no. 3, pp. 813 – 826, March 2012

[60] A. Arbabian, S. Callender, S. Kang, M. Rangwala, A.M. Niknejad, "A 94 GHz mm-wave-to-baseband pulsed-radar transceiver with applications in imaging and gesture recognition," *IEEE J. Solid-State Circuits*, vol.48, no.4, pp.1055,1071, April 2013.

[61] J. Powell, H. Kim, and C. G. Sodini, "SiGe Receiver Front Ends for Millimeter-Wave Passive Imaging," *IEEE Trans. Microwave Theory & Tech.*, vol. 56, no. 11, pp. 2416-2425, November 2008.

[62] R. R. Severino, T. Taris, Y. Deval, D. Belot, and J. B. Begueret, "A SiGe:C BiCMOS LNA for 94 GHz band applications*," in Proc. IEEE BCTM*, Austin, TX, Oct. 4–6, 2010, pp. 188–191.

[63] B. Cetinoneri, Y. Atesal, A. Fung, and G. Rebeiz, "W-band amplifiers with 6-dB noise figure and milliwatt-level 170-200- GHz doublers in 45-nm CMOS," *IEEE Trans. Microw. Theory Tech.*, vol. 60, no. 3, pp. 692 –701, March 2012.

[64] A. Tomkins, P. Garcia, and S. P. Voinigescu, "A Passive W-Band Imaging Receiver in 65-nm Bulk CMOS," *IEEE J. Solid-State Circuits.*, Vol. 45, No. 10, pp. 1981-1991, Oct. 2010.

[65] J. May and G. Rebeiz, "Design and Characterization of W-Band SiGe RFICs for Passive Millimeter-Wave Imaging," *IEEE Trans. Microw Theory Tech*, vol. 58, No. 5, pp. 1420-1430, May 2010.

[66] F. Caster II, L. Gilreath, S. Pan and Z. Wang, F. Capolino, P. Heydari, "A 93-to-113GHz BiCMOS 9-element imaging array receiver utilizing spatial-overlapping pixels with wideband phase and amplitude control," *Proc. IEEE Int. Solid-State Circuits Conf. ISSCC 2013*., pp. 144-145, Feb. 2013.

[67] Y. Yang, S. Cacina, G. M. Rebeiz, "A SiGe BiCMOS W-band LNA with 5.1 dB NF at 90 GHz," *IEEE Compound Semiconductor Integrated Circuit Symposium (CSICS)*, pp.1-4, Oct. 2013.

[68] A.C. Ulusoy, M. Kaynak, V. Valenta, B. Tillack, H. Schumacher, "A 110 GHz LNA with 20dB gain and 4dB noise figure in an 0.13μm SiGe BiCMOS technology," *IEEE MTT-S Int. Microwave Symp.Dig*, pp. 1-3, June 2013.

[69] R.A. Normann, "Technology insight: future neuroprosthetic therapies for disorders of the nervous system," *Nature Clinical Practice*, vol. 3, no. 8, pp. 444-452, Aug. 2007.

[70] N. Lovell, J. Morely, S. Chen, L. Hallum, and G. Suaning, "Biological-machine systems integration: engineering the neural interface," *Proc. of the IEEE*, vol. 98, no. 3, pp. 418-431, Mar. 2010.

[71] J. Fayad, S. Otto, R. Shannon, and D. Brackmann, “Cochlear and brainstem auditory prostheses, neural interface for hearing restoration: cochlear and brain stem implants,” *Proc. of the IEEE*, vol. 96, no. 7, pp. 1085-1095, July. 2008.

[72] B. Thurgood, D. Warren, N. Ledbetter, G. Clark, and R. Harrison, "A wireless integrated circuit for 100-channel charge-balanced neural stimulation," *IEEE Trans. Biomed. Cir. Sys.*, vol. 3, no. 6, pp. 405-414, Dec. 2009.

[73] A. Nurmikko, and *et. al*, “Listening to brain microcircuits for interfacing with external world-progress in wireless implantable microelectronic neuroengineering devices ,” *Proc. of the IEEE*, vol. 98, no. 3, pp. 375-388, Mar. 2010.

[74] S.B. Lee, H.M. Lee, M. Kiani, U.M. Jow, and M. Ghovanloo, “An inductively powered scalable 32-ch wireless neural recording system-on-a-chip with power scheduling for neuroscience applications,” Digest of technical papers *IEEE Intl. Solid State Cir. Conf.*, pp. 120-121, Feb. 2010.

[75] A. Sodagar, G. Perlin, Y. Yao, K. Najafi, K.D. Wise, "An implantable 64-channel wireless microsystem for single-unit neural recording," *IEEE J. Solid-State Circuits*, vol. 44, no. 9, pp. 2591-2604, Sept. 2009.

[76] X. Liu, A. Demosthenous, N. Donaldson, "An integrated implantable stimulator that is fail-safe without off-chip blocking-capacitors," *IEEE Trans. Biomed. Cir. Sys.*, vol. 2, no. 3, pp. 231-244, Sept. 2008.

[77] J. Weiland and M. Humayun, “Visual prosthesis,” *Proc. of the IEEE*, vol.96, no.7, pp.1076-1084, July. 2008.

[78] R.R. Harrison, R. Kier, C. Chestek, V. Gilja, P. Nuyujukian, S. Ryu, B. Greger, F. Solzbacher, and K. Shenoy, "Wireless neural recording with single low-power integrated circuit," *IEEE Trans. Neural Syst. Rehab. Eng.*, vol. 17, no. 4, pp. 322-329, Aug. 2009.

[79] J. C. Lin, “Computer methods for field intensity predictions,” in CRC Handbook of Biological Effects of Electromagnetic Fields, C. Polk and E. Postow, Eds. Boca Raton, FL: CRC, 1986, ch. 2, pp. 273-313.

[80] M. Ghovanloo and K. Najafi, "A wideband frequency-shift keying wireless link for inductively powered biomedical implants," *IEEE Trans. Cir. Sys. I*, vol. 51, no. 12, pp. 2374-2383, Dec. 2004.

[81] FCC Rules and Regulations, MICS Band Plan, Part 95, 2003.

[82] A. Shameli, A. Safarian, A. Rofougaran, M. Rofougaran, J. Castaneda, and F. De Flaviis, "A UHF near-field RFID system with fully integrated transponder," *IEEE Trans. Microwave Theory and Techniques*, vol. 56, no. 5, pp. 1267-1277, May. 2008.

[83] D. Paret, *RFID and Contactless Smart Card Applications.* NJ: Wiley, 2005.

[84] G.J. Suaning and N.H. Lovell, "CMOS neuro-stimulation ASIC with 100 channels, scalable output, and bidirectional radio-freq. telemetry," *IEEE Trans. Biomed. Eng.*, vol. 48, pp. 248–260, Feb. 2001.

[85] M. Ghovanloo and K. Najafi, "A wideband frequency-shift keying wireless link for inductively powered biomedical implants," *IEEE Trans. Cir. Sys. I: Regular Papers,* vol. 51, no. 12, pp. 2374-2383, Dec. 2004.

[86] Y. Hu and M. Sawan, "A fully integrated low-power BPSK demodulator for implantable medical devices," *IEEE Trans. Cir. Sys. I*, vol. 52, no. 12, pp. 2552-2562, Dec. 2005.

[87] M. Zhou, M. Yuce, and W. Liu, "A non-coherent DPSK data receiver with interference cancellation for dual-band transcutaneous telemetries," *IEEE J. Solid-State Circuits*, vol. 43, no. 9, pp. 2003-2012, Sept. 2008.

[88] G. Simard, M. Sawan, D. Massiocotte, "High-speed OQPSK and efficient power transfer through inductive link for biomedical implants," *IEEE Trans. Biomed. Circuits and Sys.*, vol. 4, no. 3, pp. 192-200, Jun. 2010.

[89] Z. Lu and M. Sawan, "An 8 Mbps data rate transmission by inductive link dedicated to implantable devices," *Proc. IEEE Int. Symp. Circuits Syst. (ISCAS'08)*, pp. 3057-3060, May. 2008.

[90] W. Xu, Z. Luo, and S. Sonkusale, "Fully digital BPSK demodulator and multilevel LSK back telemetry for biomedical implant transceivers," *IEEE Trans. Circuits Syst. II*, vol. 56, no. 9, pp. 714-718, Sept. 2009.

[91] M. Ghovanloo and S. Atluri, "A wideband power-efficient inductive wireless link for implantable microelectronic devices using multiple carriers," *IEEE Trans. on Circuits and Systems I*, vol. 54, no. 10, pp. 2211-2221, Oct. 2007.

[92] B. Chi, J. Yao, S. Han, X. Xie, G. Li, and Z. Wang, "Low-power transceiver analog front-end circuits for bidirectional high data rate wireless telemetry in medical endoscopy applications," *IEEE Trans Biomed. Eng.*, vol. 54, no.7, pp.1291-1299, July. 2007.

[93] J. Bohorquez, A. Chandrakasan, and J. Dawson, "A 350 μW CMOS MSK transmitter and 400 μW OOK super-regenerative receiver for medical implant communications," *IEEE J. Solid-State Circuits*, vol. 44, no. 4, pp. 1248-1259, Apr. 2009.

[94] S. Mandal and R. Sarpeshkar, "Power-efficient impedance-modulation wireless data links for biomedical implants," *IEEE Trans. Biomed. Circuits and Sys.*, vol. 2, no. 4, pp. 301-315, Dec. 2008.

[95] A.P. Chandrakasan, F.S. Lee, D.D. Wentzloff, V. Sze, B.P. Ginsburg, P.P. Mercier, D.C. Daly, and R. Blazquez, "Low-power impulse UWB architectures and circuits," *Proc. of the IEEE*, vol. 97, no. 2, pp. 332-352, Feb. 2009.

[96] A.P. Chandrakasan, N. Verma, and D.C. Daly, "Ultralow-power electronics for biomedical applications," *Annu. Rev. Biomed. Eng*., vol. 10, pp. 247–274, 2008.

[97] T. Buchegger, G. Oberger, A. Reisenzahn, E. Hochmair, A. Stelzer, and A. Springer, "Ultra-wideband transceivers for cochlear implants," *EURASIP J. Applied Signal Processing*, vol. 18, pp. 3069–3075, 2005.

[98] M.S. Chae, Z. Yang, M. Yuce, L. Hoang, and W. Liu, "A 128-channel 6 mW wireless neural recording IC with spike feature extraction and UWB transmitter," *IEEE Trans. Neural Sys. and Rehab. Eng.*, vol. 17, no. 4, pp. 312-321, Aug. 2009.

[99] J.C. Lin, A.W. Guy, and C.C. Johnson, "Power deposition in a spherical model of man exposed to 1-20 MHz electromagnetic fields," *IEEE Trans. Microwave Theory and Techniques*, vol. 21, no. 12, pp. 791 – 797, Dec. 1973.

[100] N. Miura, D. Mizoguchi, M. Inoue, T. Sakurai, and T. Kuroda, "A 195-Gb/s 1.2-W inductive inter-chip wireless superconnect with trasnmitter power control scheme for 3-D-stacked system in a package", *IEEE J. Solid-State Cir.*, vol. 41, no. 1, pp. 23-33, Jan. 2006.

[101] H. Ishikuro, N. Miura, and T. Kuroda, “Wideband Inductive-coupling Interface for High-performance Portable System," *IEEE Custom Integrated Circuits Conf. (CICC)*, pp.13-20, 2007.

[102] D. Guermandi, S. Gambini, and J. Rabaey, “A 1 V 250 kpps 90 nm CMOS pulse based transceiver for cm-range wireless communication,” in *Proc. IEEE Eur. Solid-State Circuits Conf.*, pp. 135–138, Sept. 2007.

[103] S. Lee, J. Yoo, and H.J. Yoo, "A 200-Mbps 0.02-nJ/b dual-mode inductive coupling transceiver for cm-range multimedia application," *IEEE Trans. Cir. and Sys. I*, vol. 56, no. 5, pp. 1063-1072, May. 2009.

[104] J. Yoo, S. Lee, and H.J. Yoo, “A 1.12 pJ/b inductive transceiver with a fault tolerant network switch for multi-layer wearable body area network applications,” *IEEE J. Solid-State Cir.*, vol. 44, no. 11, pp. 2999-3010, Nov. 2009.

[105] U. Jow and M. Ghovanloo, "Optimization of data coils in a multiband wireless link for neuroprosthetic implantable devices," *IEEE Trans. Biomed. Circuits Syst.*, vol. 4, no. 5, pp. 301-310, Oct. 2010.

[106] F. Inanlou and M. Ghovanloo, “Wideband near-field data transmission using pulse harmonic modulation,” *IEEE Trans. on Cir. and Sys. I*, vol. 58, no. 1, pp. 186-195, Jan. 2011.

[107] M. Z. Win and R. A. Scholtz, “Impulse radio: How it works,” *IEEE Commun. Lett.*, vol. 2, pp. 10–12, Jan. 1998.

[108] Altera, Cyclone II Field Programmable Gate Array, [Online]. Available http://www.altera.com/products/devices/cyclone2/overview/cy2-overview.html.

[109] Quartus II Web Edition Software, [Online]. Available: http://www.altera.com/products/software/quartus-ii/web-edition/qts-we-index.html.

[110] M. Yin and M. Ghovanloo, “A low-noise receiver for multichannel wireless neural recording,” Proc. *IEEE 30th Eng. in Med. and Biol. Conf.*, pp. 4222-4225, Aug. 2008.

[111] D. Johns and K. Martin, *Analog Integrated circuit Design. New York*, NY: Wiley, 1996.

[112] M. Crepaldi, C. Li, K. Dronson, J. Fernandes, and P. Kinget, "An ultra-low-power interference-robust IR-UWB transceiver chipset using self-synchronizing OOK modulation," *IEEE Int. Solid-State Cir. Conf. Dig. Tech. Papers,* pp. 226-227, Feb. 2007.

[113] R. Dokania, X. Wang, S. Tallur, C. Dorta-Quinones, and A. Apsel, "An ultralow-power dual-band UWB impulse radio," *IEEE Trans. Cir. Sys. II,* vol. PP, pp. 1-5, Jun. 2010.

[114] F. Lee and A. Chandrakasan, "A 2.5 nJ/b 0.65 V 3-to-5 GHz subbanded UWB receiver in 90 nm CMOS," *IEEE Int. Solid-State Cir. Conf. Dig. Tech. Papers,* pp. 116–590, Feb. 2007.

[115] T.-A. Phan, V. Krizhanovskii, and S.-G. Lee, "Low-power CMOS energy detection transceiver for UWB impulse radio system," *Proc. IEEE Custom Integr. Cir. Conf.,* pp. 675-678, Sept. 2007.

[116] Y. Zheng, Y. Tong, J. Yan, Y.-P. Xu, W. G. Yeoh, and F. Lin, "A low power noncoherent CMOS UWB transceiver ICs," *Proc. IEEE Radio Freq. Integr. Cir. Symp.,* pp. 347-350, Jun. 2005.

[117] A. Chandrakasan F.S. Lee, D.D. Wentzloff, V. Sze, B.P. Ginsburg, P.P. Mercier, D.C. Daly, and R. Blazquez, "Low-power impulse UWB architectures and circuits," *Proceeding of IEEE,* vol. 97, pp. 332-352, Feb. 2010.

[118] U. Jow and M. Ghovanloo, "Modeling and optimization of printed spiral coils in air, saline, and muscle tissue environments," *IEEE Trans. on Biomed. Cir. and Sys.,* vol. 3, no. 5, pp. 339-347, Oct. 2009.

VITA

Farzad Michael-David Inanlou was born in Mashhad, Iran in 1984. He received the B.S. degree from Ferdowsi University, Mashhad, Iran, in 2006, and the M.S. degree from Boston University, Boston, MA, in 2008, both in Electrical Engineering. In 2008 Farzad joined the School of Electrical and Computer Engineering's PhD program at Georgia Institute of Technology, Atlanta, GA with a minor in Biomedical Engineering. During summers of 2008, 2010, and 2013 he was with Boston Scientific Neuromodulation, Valencia, CA as an R&D ASIC Design Intern, Korea Institute of Science and Technology, Seoul, South Korea as a National Science Foundation visiting scholar, and Qualcomm, San Diego, CA, as an RFIC Design Intern, respectively.

His PhD research expanded to encompass innovative transceiver design methods in advanced silicon technologies, including SiGe BiCMOS and CMOS processes for RF and millimeter-wave low-power applications. Mr. Inanlou is the recipient of the Georgia Institute of Technology President's Fellowship, and 2010 EAPSI Fellowship from the National Science Foundation.

Following the completion of his PhD he will begin employment as a Research Engineer in RF/Microwave Engineering at NASA's Jet Propulsion Laboratory, Pasadena, CA.